(12)

PENNSTATE

Applied Research Laboratory

Annual Report
1 Feb. 1990 to 31 Jan. 1991

STUDIES OF MHD PROPULSION FOR UNDERWATER VEHICLES AND SEAWATER CONDUCTIVITY ENHANCEMENT

Sponsored By

Department of the Navy
Office of Naval Research
Grant No. N00014-89-J-1693

Prepared By

J. B. Gilbert and T. F. Lin
February 1991

Applied Research Laboratory and
The Nuclear Engineering Department
The Pennsylvania State University
P.O. Box 30
State College, PA 16804

ABSTRACT

This study analyzes the feasibility of MHD propulsion for marine vessels. A theoretical analysis is developed and analytical results are obtained for two vehicle geometries. The first (class 1) is for small vehicles with sizes approximating that of torpedoes, remotely operated vehicles (ROV), and underwater autonomous vehicles (UAV). The second geometry (class 2) corresponds to larger submersibles such as submarines. Vehicle speed, thrust, and efficiency are analyzed as a function of magnetic field strength and channel velocity. Results indicate that thruster performance measures as the square of an increasing magnetic field strength and linearly with increasing conductivity. The analytical results show that the MHD thruster tends to favor larger geometries and channel lengths, such as those applicable to class 2 vehicles.

Based on analytical parametric studies, the MHD thruster propelled large submersible can attain comparable velocities to that of present day submarines (20-42 knots). Additionally the MHD thruster concept offers potentially easier maintenance because of no moving parts and thereby reduced vessel detectibility. Higher speeds then attained by present submersibles may be possible due to reduced hydrodynamic drag.

Since the MHD thruster concept is based on Lorentz force (jxB) acting upon seawater, the ionic conductance characteristics of seawater are of paramount importance. An experimental investigation of ionic conductance of seawater under flowing conditions is conducted. Results are analyzed as both a function of current versus voltage and overvoltage versus current density.

Conductance increased with increasing flow rates. This is attributed to two different causes. First, cases were studied in the order of increasing flow. Due

to Ohmic heating, the temperature of the synthetic seawater increased during the experiment and an increase in temperature corresponds to an increase in conductance. The second cause of increased conductance with increasing flow rate is due to increased "flushing" of the nonconductive gaseous products. Platinum-plated copper, Hastelloy-C, graphite and dimensionally stable anode (DSA) were evaluated as electrode materials. Of these, graphite and DSA were the best performers with no noticeable corrosion/errosion. However, it is worth noting that graphite is brittle.

Conductivity enhancement of seawater by the seeding of acids and bases, under beaker tests, steady states, and dynamic pulsed injections, were conducted. The results were not only positive, but also consistent with theoretical prediction.

Based on this theoretical and experimental investigation, MHD thruster propulsion for marine vehicle applications is very promising. However, construction of a prototype MHD thruster is needed to benchmark the theoretical studies. Further research in electrode metallurgy and hydrogen/oxygen/chlorine gas evolution also needs to be conducted to solve potential problems in MHD thruster design.

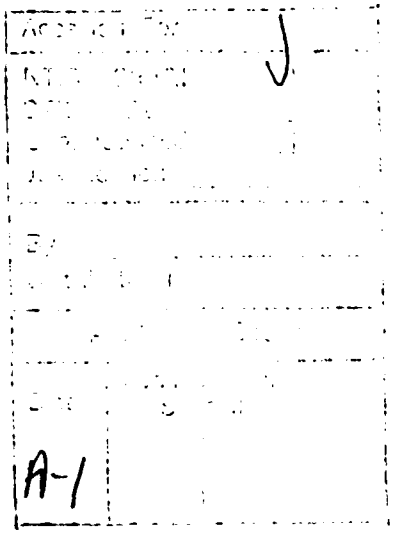

TABLE OF CONTENTS

TABLE OF CONTENTS (Continued)

TABLE OF CONTENTS (Continued)

LIST OF TABLES

LIST OF FIGURES

LIST OF FIGURES (Continued)

LIST OF FIGURES (Continued)

NOMENCLATURE

A_{ex}	exit area of the MHD channel (m^2).
A_{in}	entrance area of the MHD channel (m^2).
A_{surf}	surface area of the vehicle.
B	magnetic field strength (T).
C	nozzle discharge coefficient.
C_D	drag coefficient of vehicle surface.
D	electrode gap distance (m).
D_H	hydraulic diameter (m).
D_e	equivalent hydraulic diameter (m).
E	flow-induced counter electric field (volt/m).
E_a	potential of Anode (volt).
E_c	potential of Cathode (volt).
F	velocity-of-approach factor of a nozzle.
F_{em}	Lorentz force (N).
f	Darcy-Weisbach friction factor for pipe flows.
I	current across the electrodes (A).
i	current density ($A \cdot m^{-2}$).
L	active length of the MHD channel (m).
$\dot{m}$	mass flowrate in a MHD channel (kg/s).
N_{ch}	number of MHD channels.
P_e	electrical power required by the MHD channel (watts).
P_w	mechanical power imparted to the sea water in the MHD channel (watts).
p_{amb}	ambient pressure of the vehicle (Pa).
p_{in}	entrance pressure of an MHD channel (Pa).
p_{ex}	exit pressure of an MHD channel (Pa).

R	resistance of sea water in the MHD channel (Ohms).
R_e	Reynold's number.
s	area ratio between the nozzle exit and the channel entrance (A_{ex}/A_{in}).
T	thrust of an MHD channel (N).
U_{ex}	velocity of the sea water exiting from the nozzle (m/s).
U_{in}	velocity of the sea water in the channel (m/s).
V	voltage across the electrodes (volts).
V_s	velocity of the vehicle (m/s or knots).
V_{ch}	active volume of sea water in the MHD channel (m^3).
W	width of the electrode (m).
Y	nozzle expansion coefficient.
Δp_{ch}	pressure rise or drop across the entire MHD channel (Pa).
Δp_N	pressure drop across nozzle (Pa).
ΔV	Voltage drop across two oppositely charged electrode plates separated electrolyte.
η	total overvoltage ($volts$).
η_A	activation overvoltage ($volts$).
η_D	diffusion overvoltage ($volts$).
η_e	electric efficiency.
η_{ind}	field induction efficiency.
η_t	total efficiency.
σ	electric conductivity of sea water ($1/(\Omega \cdot m)$).
ρ	sea water density (kg/m^3).
ν	kinematic viscosity (m^2/s).

ACKNOWLEDGEMENTS

This work was supported mainly by the Office of Naval Research Grant No: N00014-89-J-1693 with Dr. Gabriel D. Roy as Scientific Officer and Dr. Richard Miller as program manager of code 1132P, and in part by the Applied Research Laboratory of The Pennsylvania State University (Project No: 1832).

To Tom Imblum, Joe Naggar, Michael Bausch, and Sean Marks, we extend our sincere appreciation for their help in construction and operation of the experimental test sections and compilation of the data attained. Their devotion to the project has been reflected in its outstanding success.

In addition, we thank the following individuals and firms for their services: Kumiko Higman for translating reference 39; James C. Mankin for proof reading the electrochemistry section in Chapter 4; Tony Sacco of Eltech Research Corporation for providing free samples of the dimensionally stable electrode; Mike Ammerman of Engelhard Corporation for providing free platinum plating; Ken Mann of TRA-CON Incorporated for supplying free samples of silver epoxy; Bea Hampton of International Polychemical Service Corporation for providing free samples of WELD-ON 40 Acrylic Cement; Chem Serve Corporation for providing free samples of Aracid Rubine Dye; and Mike Coslo, Randy Riesterer, and Tracy Hanselman of Applied Research Laboratory Photography Staff for their assistance in photographing the experimental apparatus for synthetic seawater electrolysis.

Chapter 1

INTRODUCTION

1.1 Objective

The purpose of this study is to analyze the feasibility of the magnetohydrodynamic (MHD) thruster as a propulsion mechanism for next generation marine vehicles. A physical dimensional model is developed to address overall performance of a vessel using the MHD thruster based on conservation of mass, momentum and energy. Experiments using synthetic sea-water are conducted to determine conductivity and pressure drop dependence with reference to voltage and flow rates. Performance of platinum plated copper, carbon and Hastelloy-C as materials for cathode and anode is examined. Finally, conductivity enhancement using H_2SO_4, HCl and $NaOH$ is evaluated.

1.2 Development of the MHD Concept

Seawater conducts electricity on a modest scale by electrolytic ion exchange. While its conductivity is several orders of magnitude lower than metals, it is significantly higher than fresh water. By taking advantage of seawater's modest electric characteristics, the electromagnetic propulsion of marine vehicles has been a subject of technical speculation and study for some years [1-6]. The concept did not appear to hold much promise until the advent of the superconducting magnet. With such a magnet, the power requirement for excitation is virtually absent, and the weight penalty of the magnet is drastically reduced. Also, much stronger magnetic field than those previously attainable can be realized. Nevertheless, the reinforcing structures to ensure the integrity of the multitesla magnets are still needed.

To date, four basic forms of MHD propulsion have been studied. These are internal flow direct current (d.c.), internal flow induction, external flow d.c., and external flow induction. All four methods apply Lorentz (**j** x **B**) force to provide kinetic energy to the fluid medium being acted upon. In the induction methods, a magnetic field is varied along the length of the vessel with intensity proportional to a sine function. These fluctuations induce a circling electric current in the seawater perpendicular to the axis of the vessel. Via Lorentz forces, the seawater is thrusted to the rear of the vehicle. The internal d.c. duct system imparts kinetic energy to the channel fluid by passing an electric field through the fluid perpendicular to the magnetic field. The fluid is thrusted in the direction normal to the (**j** x **B**) plane.

The concept of the MHD thruster as a marine vehicle power supply was first evaluated in 1962 by O. M. Phillips. His analysis addressed d.c. free field and duct propulsion systems. In his study, the duct system obtained the best results. His analysis was based upon a 600 ft submarine utilizing a 6000 Gauss (.6 T) field and setting conductivity of seawater to 4 ($\Omega^{-1}m^{-1}$). The vehicle achieved a theoretical speed of 10 knots but with an efficiency of $\eta_t = .08$. According to Phillips' calculations, to obtain a 30% efficient system at 30 knots, a 20,000 gauss (2 T) magnetic field would be required [3]. However, Phillips did not account for scaling of the MHD thruster; an increase in channel volume results in a corresponding increase in efficiency.

1.3 The Prototypes

In 1966, the EMS-1, a 10 ft long 900 lb external field model, was developed and constructed at the University of California in Santa Barbara. Having an active length of 1 m and radius of .225 m with a .015 T electromagnet and a 30 volt

internal power supply, this model sustained a velocity of approximately 1 ft/s (.4 m/s) for 20 minutes. In these experiments, gas evolution at the electrodes was found not to be a serious problem [6].

Recent advances in cryogenics have made the superconducting magnet feasible for MHD propulsion. As early as 1979, A. Iwata, and Y. Saji constructed the ST-500; a 3.6 m long wooden model which was propelled by a 2.0 T (maximum) external field thruster. This vessel obtained a velocity of .6 m/s through a maximum thrust of 20 N [7]. A problem with this design was that it greatly accelerated the fluid next to the ship's body, thereby increasing the drag exerted against propulsion. This is a major flaw in any external field application.

In January 1984, E. Tada et al. designed an icebreaker to utilize d.c. external field MHD thrusters. This vessel was conceptualized as having 12 thrusters mounted at the bottom of the hull. Characteristic features of the ship were length of 80 m, active propulsion length of 10 m, with a magnetic field of 2.7 T. The η_t for this system was less than or equal to .1. Problems with this system were excessive weight, insufficient magnetic field, and hydrogen and chlorine gas formation at the electrodes. Liquid helium was also used in this design to maintain superconductive temperature at -269° C. Complexities in cryostat design to maintain liquid helium at this temperature were also a problem [8].

Because of drawbacks inherent to external magnetic field thrusters, the Japanese Foundation for Shipbuilding Advancement is now evaluating the d.c. internal duct design, and constructed in 1987 a model ship using this technology [9]. Construction of a full scale ship is scheduled to be completed in the year 1990. The experimental ship will have a displacement of 150 tons, 4 T field in duct channel, and propulsive thrust of 8000 N attaining a design velocity of 8 knots. The thrust

efficiency is expected to be very high [10]. In addition to the Japanese research, Argonne National Laboratory is constructing a test loop which will utilize a 6 T magnet to drive a MHD thruster. Again the emphasis is on internal duct d.c. system. This magnet is a 21 by 13 foot dipole , but has a disadvantage in that it was designed for fusion research applications and has a weight of 172 tons [11]. Of even more interest, intelligence experts in the United States and Britain believe that a pod mounted on top of the vehicle rudder in *VictorIII*, *Sierra* and *Akula* class Soviet nuclear attack submarines contains a MHD drive utilizing internal duct d.c. current configuration. The dimensions of the pod are 29.5 feet long, 8.2 feet outer diameter and 2.5 feet inner diameter at the inlet. One analyst estimated that this device could provide enough thrust for a vehicle speed of 7 knots [12].

It appears that the MHD propulsion mechanism is today a reality. Whether this propulsion method will be economically attractive or not is a question that must await further investigation. However, it is fair to predict that in certain naval applications such as submarines where the importance of acoustic signature outweighs other considerations, the MHD technology which offers superior quietness because of reduced mechanical moving parts will prevail.

1.4 Military Applications

A primary application for the MHD thruster is in submarine propulsion. Submarines comprise a major portion of world power navies and have played a key role in naval warfare since World War I. Unlike any other vessel, they are capable of operating undetected in the world seaways. In spite of improved anti-submarine warfare (ASW) technology, this is still true. The submarine's stealth is what makes

it a viable and effective weapon and the MHD thruster should improve this characteristic.

At present, there are three principle methods used in submarine detection. Two of the techniques take advantage of water's excellent ability to conduct sound waves. The first method is active acoustical detection (active sonar) where sound waves are emitted by user, attenuated by the target's surface, and reflected back. Active sonar is well proven and effective but gives away the user's position thereby making him vulnerable to retaliatory measures. The second method is passive sonar which uses hydrophones to listen for an acoustical signature being emitted by the submarine. While this method does not give away the position of the user, it requires that the vessel be emitting enough noise to be detected and it does not have as effective a range as active sonar. Finally, magnetic anomaly detectors are used to detect disturbances in the earth's magnetic field due to large metallic objects such as submarines. These detective devices, while also being passive, have a limited range of only a few thousand feet [13]. A fourth method, detection via thermal signature given off by submarine's thermal discharge, is a very promising new technique but will not be discussed in this analysis.

The key to the submarine's effectiveness is, again, its ability to avoid detection. Therefore developments in submarine technology have been primarily concerned with reducing the vessels signature in the presence of ASW devices. For any proposed propulsion system, this is of paramount importance. The three primary sources of noise—propeller, hull and machinery [14]—have been reduced to a great extent. However due to the nature of moving parts, complete silencing of present drive systems is not expected. These systems include diesel-electric and nuclear powered propellers. The former utilizes bat'ery and/or generator power to drive

the propeller(s) and other shipboard systems. The diesel-electric system has a characteristically short cruising range of approximately 10,000 miles. However, when on battery power, this drive system is virtually acoustically silent [14] but is restricted to low speeds (10-20 knots) [15]. The diesel-electric submarine carries a much lower price tag than its nuclear counterpart. Thus the diesel-electric propelled submarine is an optimal system for coastal defense, especially for countries with small military budgets.

However, nuclear powered submarines are the predominant choice for larger navies. To demonstrate this point, as of 1980 over 115 of the United States' submarines were nuclear powered [16] while the Soviet arsenal was approximately 190 [14]. The contributing factor is virtually indefinite cruising range and sustained high vehicle speeds provided by the nuclear power plant. Although noisy at high power levels, the typical pressurized water reactor (PWR) can operate quietly at low power by utilizing natural circulation techniques. Unfortunately, the noise generated by turbine gear reduction is still present. A turbine-electric drive submarine, the *Tullibee*, was laid down in 1958 with intentions of alleviating this problem. This noise reducing design was successful, but the vessel could only attain a velocity of 15 knots [16].

For comparison, the typical *Los Angeles* class submarine with S6G Westinghouse power plant can produce approximately 35,000 *shp* (26.1 MW) while the *Ohio* class using a S8G Westinghouse power plant generates a reported 60,000 *shp* (42.3 MW). These vehicles have speeds of 30+ and 20+ knots, respectively [17]; the *Ohio* class has a lower speed because it is a much larger submarine. The Soviet *Alfa* class submarine attains a very respectable 42 knots with 24,000 *shp* [15]. Because of its extremely small size, this submarine is believed to use a liquid metal fast breeder

reactor as well as automated control systems [18]. Obviously the *Tullibee*'s 15 knots is not adequate so the turbine gear-reduction noise problem remains. However, the magnetohydrodynamic thruster is a very attractive solution to this impasse.

The following chapter discusses in detail the theoretical background of this type of MHD pump jet propulsion. The vehicle's speed, efficiency and thrust performances as determined analytically are covered in chapter 3. The basic properties and recent scientific studies of seawater electrolysis are presented in chapter 4. Chapter 5 describes the design and operating procedures of a test loop constructed to evaluate the electrolytic behavior of synthetic seawater. The results of seawater electrolysis experiments are presented in chapter 6. The concept of conductivity enhancement of seawater as well as experimental results using sulfuric acid are presented in chapter 7. Chapter 8 discusses new technology which may contribute to the feasibility of the MHD propulsion device. And chapter 8 concludes with the potential future applications and areas needing further study for the MHD thruster based on this study.

Chapter 2

THEORETICAL ANALYSIS

2.1 Introduction

Two slightly different conceptualizations of the MHD thruster are presented in Figures 2.1 and 2.2. Figure 2.1 represents a submersible propelled by an annular thruster whereas Fig. 2.2 depicts a vehicle utilizing an array of rectangular duct thrusters. Both designs function on the basis of the same principles with the only significant difference being the channel geometry.

In both cases, seawater is sucked into the inlet of the thruster. The d.c. electric current is supplied through the electrodes to the seawater traveling in the channel. A magnetic field oriented perpendicular to the electric field is passed through the fluid in the duct. The resulting Lorentz force pumps the fluid through the exit nozzle. In the absence of a constricting nozzle, the fluid would be ejected with greater pressure than ambient. The difference in pressure and momentum between inlet and exit of the MHD motor provides thrust which will propel the vehicle.

In general, the annular thruster offers a higher thrust efficiency by minimizing frictional surface area per unit volume of fluid in the channel. However, a design incorporating a series of thrusters distributed symmetrically around the vehicle offers navigational control by varying the thrust in respective channels. This could eliminate the need for drag inducing appendages such as rudders.

2.2 Analysis of the MHD Pump

A schematic of the duct-type MHD thruster is illustrated in Figure 2.3. Seawater entering the thruster becomes the medium for an electric current produced

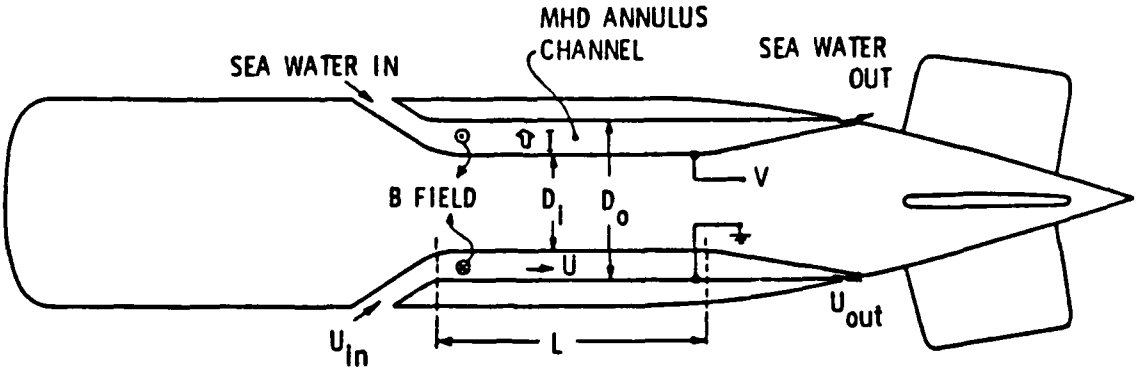

Figure 2.1 Submersible with an Annular MHD Channel.

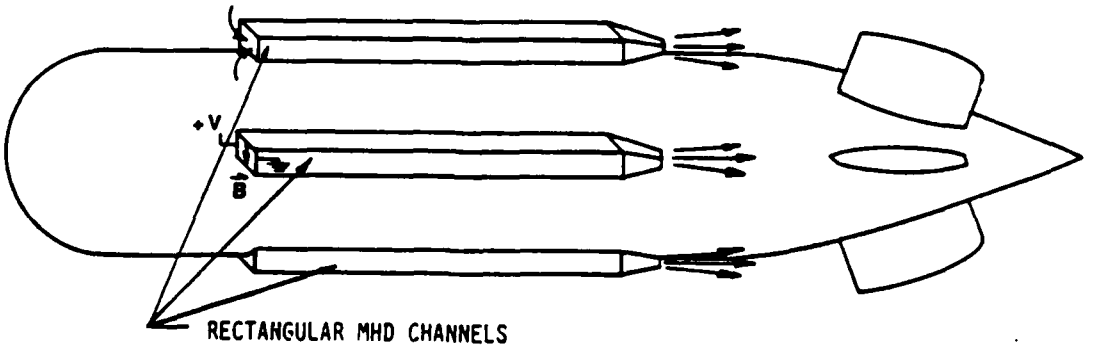

Figure 2.2 Submersible with Rectangular MHD Channels.

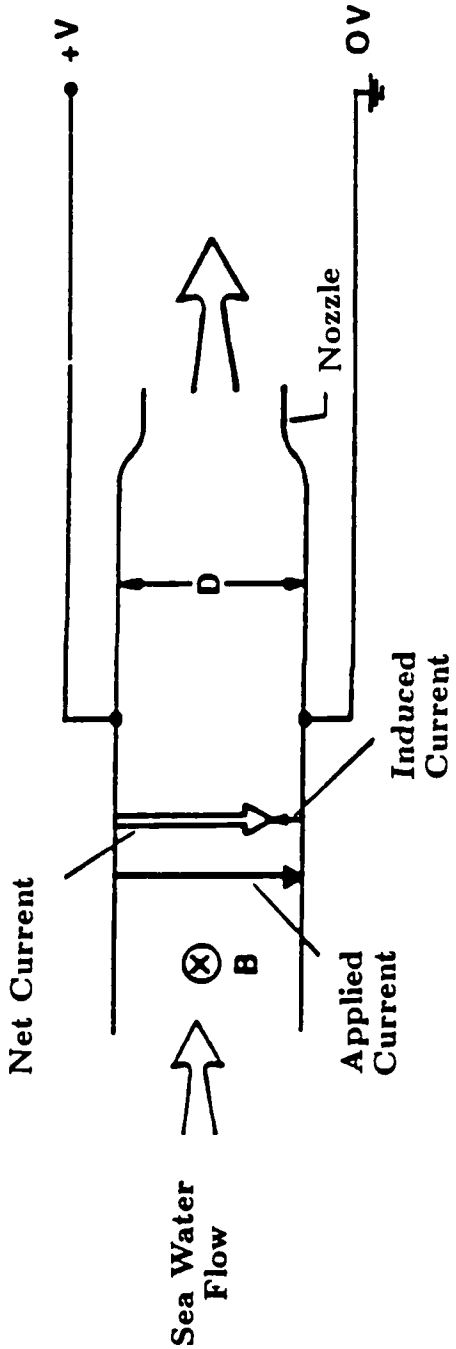

Figure 2.3 Schematic of a Duct-Type MHD Channel.

through two oppositely charged electrode plates (current travels from the top to the bottom in Figure 2.3). Simultaneously, the seawater is exposed to an intense magnetic field perpendicular to the electric field (directed into the paper in Fig. 2.3). The Lorentz force propels the fluid through the exit nozzle. The net current, I, flowing across the MHD channel between the electrodes is,

$$I = \frac{V - ED}{R}, \tag{2.1}$$

where V is the voltage drop across the electrode, E is the flow-induced electric field that opposes the current and R is the resistance incurred through the electrolyte. When using a rectangular duct geometry,

$$R = \frac{D}{\sigma W L}, \tag{2.2}$$

where D is the gap distance between electrode plates, σ is conductivity of the electrolyte, and W and L are width and length of the electrode plate. Using the MHD approximation, the induced electric field can be written as [19],

$$E = BU_{in}, \tag{2.3}$$

where B is the magnetic field as seen by the channel fluid, and U_{in} is the mean velocity in the duct. Defining the field induction efficiency to be,

$$\eta_{ind} = \frac{ED}{V} = \frac{BU_{in}D}{V}, \tag{2.4}$$

the net current becomes [combining Eq. (2.1) and (2.4)],

$$I = \frac{1 - \eta_{ind}}{\eta_{ind}} \sigma B U_{in} W L. \tag{2.5}$$

The total Lorentz force applied to the seawater in the duct is:

$$F_{em} = IDB = \frac{1 - \eta_{ind}}{\eta_{ind}} \sigma B^2 U_{in} D W L$$

$$= \frac{1 - \eta_{ind}}{\eta_{ind}} \sigma B^2 U_{in} V_{ch}, \tag{2.6}$$

where V_{ch} is the volume of fluid between electrode plates. The mechanical power, P_w, imparted on the seawater in the duct is,

$$P_w = F_{em} U_{in} = \frac{1 - \eta_{ind}}{\eta_{ind}} \sigma B^2 U_{in}^2 V_{ch}. \tag{2.7}$$

The electrical power, P_e, supplied to the thruster is,

$$P_e = VI = \frac{1 - \eta_{ind}}{\eta_{ind}} \sigma B V U_{in} W L. \tag{2.8}$$

The efficiency, η_e, in converting electrical power (P_e) to mechanical power (P_w) can now be defined as,

$$\eta_e = \frac{P_w}{P_e} = \frac{B U_{in} D}{V}, \tag{2.9}$$

which is the same as the field induction efficiency $\eta_e = \eta_{ind}$. From Eq. (2.8) it is evident that a large value of η_{ind} is undesirable because it implies minimal electrical power. However, common sense dictates that the value for electrical efficiency must be as large as possible.

The optimal value of η_e (η_{ind}) can be shown by the following approach. Reducing Eq. (2.7) by using the definition of electrical efficiency (Eq. (2.8)) and equating electrical and mechanical efficiency, one obtains,

$$P_w = (1 - \eta_e)\eta_e \sigma V^2 \frac{V_{ch}}{D^2}. \tag{2.10}$$

Assuming a channel with fixed geometry and electrical potential, the mechanical power may be optimized by taking the derivative of Eq. (2.10) with respect to η_e and setting it equal to zero. This, as expected, yields an optimal η_e equal to .5. Thus the MHD thruster will always incur at least a 50% loss in energy during conversion from electrical to mechanical power. This loss will be in Ohmic heating of the electrolyte and must be taken into account in any MHD thruster analysis or design.

2.3 Dual-Control-Volume Analysis

Previous MHD thruster analyses have utilized the Bernoulli's equation to model momentum exchanges [20,21]. These studies did not take into account viscous losses within the thruster channel and they assumed ambient pressure at the inlet (p_{in}) and outlet (p_{ex}) of the thruster. Such assumptions are not justified. To address the performance of the thruster while accounting for these effects, two separate control volumes were modeled. The first models the internal parameters of the thruster and includes various losses therein (see Figure 2.4). The second control volume relates the thrust provided to the parameters of the vehicle (see Figure 2.5). Since the two control volumes are coupled by inlet and exit areas, inlet and exit pressures, vehicle velocity and mass flow rate, these parameters must be solved simultaneously and cannot be assumed.

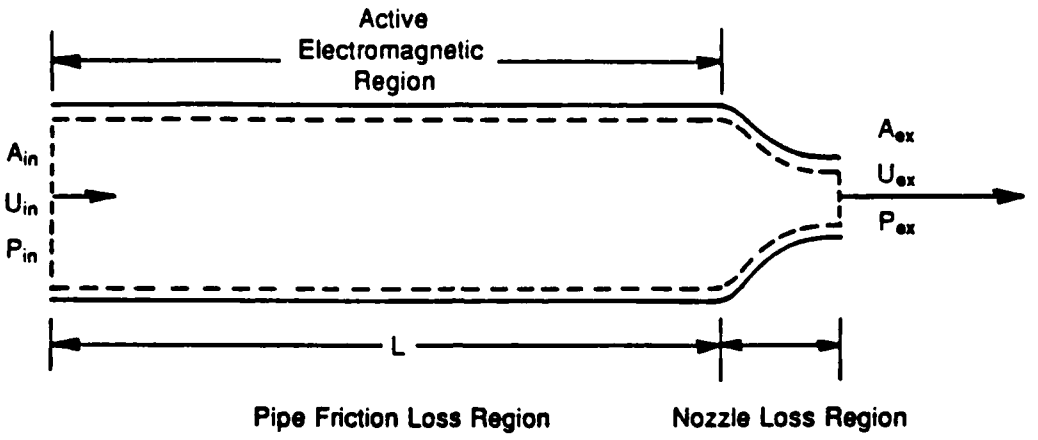

Figure 2.4 Control Volume #1.

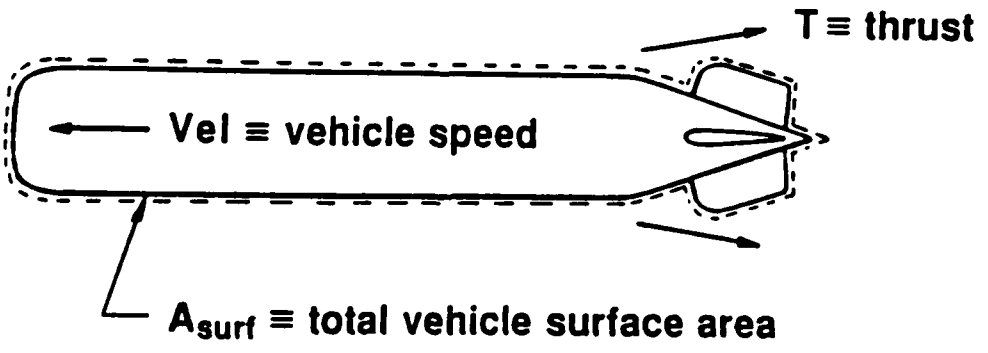

Figure 2.5 Control Volume #2.

The area enclosed by a dashed line in Fig. 2.4 is control volume 1. The conservation of mass and momentum for this control volume will now be address. Defining the ratio between exit area and channel area as s, the conservation of mass can be written as follows:

$$U_{ex} = \frac{U_{in}}{s}. \tag{2.11}$$

Here U_{ex} is the velocity of fluid being expelled by the thruster. Expansion of seawater due to ohmic heating is assumed negligible. Therefore the density is constant.

The conservation of momentum can be written as,

$$\rho U_{in} A_{in}(U_{ex} - U_{in}) = IBD - (f\frac{L}{D_H}\frac{\rho U_{in}^2}{2})A_{in}$$

$$-\Delta p_N A_{in} + (p_{in}A_{in} - p_{ex}A_{ex}). \tag{2.12}$$

The first term on the right-hand side (RHS) of Eq. (2.12) is the Lorentz force acting on the seawater. The second term on the RHS accounts for viscous dissipation in the straight channel. Here f is the Darcy-Weisbach friction factor and is explicitly approximated by the relation [22],

$$f = [1.14 - 2log_{10}(\frac{\epsilon}{D_H} + \frac{21.25}{R_e^{.9}})]^{-2}. \tag{2.13}$$

ϵ is the equivalent surface roughness. A comparison of this relation with the Moody plot for various Reynold's numbers R_e is given in Table 2.1. D_H is the hydraulic diameter of the channel. For noncircular ducts, f yields a friction factor within 10% of experimental data. However, an equivalent diameter has been developed to better approximate turbulent flows [22].

$$D_e = \frac{64}{k}D_H. \tag{2.14}$$

TABLE 2.1 Evaluation of f as a Function of Equation (2.13) Versus Moody Chart

R_e	f (Moody Chart)	f (Equation (2.13))
4,000	.040	.040500812
5,000	.037	.037800248
10,000	.0309	.030938265
15,000	.0276	.027756989
50,000	.0208	.020742071
100,000	.0179	.017847757
500,000	.0132	.013080866
1,000,000	.0117	.011598713

The laminar flow friction coefficient k is determined by [22],

$$k = fR_e = \frac{64}{\frac{2}{3} + \frac{11D}{24W}(2 - \frac{D}{W})}. \tag{2.15}$$

The third term on the RHS of Eq. (2.12) accounts for losses incurred by a constricting nozzle. Nozzle loss is developed from the Bernoulli's equation and can be expressed as [23],

$$\Delta p_N = \frac{1}{2\rho} \frac{\dot{m}^2}{(YFCA_{ex})^2}. \tag{2.16}$$

Here $\dot{m}$ is the mass flow rate. Y is the expansion factor (unity for liquids). F, velocity-of-approach factor, is defined as $F = 1/\sqrt{1 - s^2}$. C is the nozzle discharge coefficient and is approximately .98 for smooth transition nozzles at high Reynold's numbers [24]. The last term on the RHS of Eq. (2.12) is the pressure difference between inlet and exit of channel in control volume 1.

The thrust produced by the MHD channel can be written using momentum principles [25] as,

$$T = \dot{m}(U_{ex} - U_{in}) + (p_{ex}A_{ex} - p_{in}A_{in})$$

$$+p_{amb}(A_{in} - A_{ex}). \tag{2.17}$$

The first term in the RHS of Eq. (17) is the momentum thrust. The second and third terms comprise the pressure thrust. p_{amb} is the ambient pressure at vehicle operation depth. Combining Eq. (2.12) and (2.17), the thrust can be written as,

$$T = \Delta p_{ch}A_{in} + p_{amb}(A_{in} - A_{ex}). \tag{2.18}$$

Δp_{ch} is the pressure difference between inlet and exit of the MHD channels and is defined as,

$$\Delta p_{ch} A_{in} = (p_{ex} - p_{in}) A_{in}$$

$$= IBD - (f \frac{L}{D_H} \frac{\rho U_{in}^2}{2}) A_{in} - \Delta p_N A_{in}. \tag{2.19}$$

The relationship between thrust provided by one MHD channel and vehicle velocity is obtained by a force balance on the second control volume enclosed by dotted lines in Fig. 2.5.

$$C_D A_{surf} (\frac{1}{2} \rho V_s^2) = N_{ch} T, \tag{2.20}$$

The left hand side (LHS) of this equation represents the friction drag of the vessel as a function of wetted surface area external to the vehicle, A_{surf}. N_{ch} is the total number of MHD channels and C_D is the coefficient of drag. The empirical formula for C_D approved by the International Towing Tank Conference of 1957 [26-28] and used in this study is,

$$C_D = \frac{.075}{(log_{10} R_e - 2)^2}. \tag{2.21}$$

Here R_e is the Reynold's number defined as,

$$R_e = \frac{V_s L}{\nu}, \tag{2.22}$$

Where L is the length of the vehicle and ν is the kinematic viscosity of the fluid. By a manipulation of variables, the thrust in Eq. (2.17) can be expressed as,

$$T = \dot{m}(U_{ex} - U_{in}) - (p_{in} - p_{amb})(A_{in} - A_{ex})$$

$$+\Delta p_{ch} A_{ex}, \tag{2.23}$$

where $(p_{in} - p_{amb})$ can be approximated using Bernoulli's equation,

$$p_{in} - p_{amb} = \frac{1}{2}\rho(V_s^2 - U_{in}^2). \tag{2.24}$$

Rewriting the thrust term in Eq. (2.20) in terms of Eq. (2.23) and (2.24), the following relation is obtained:

$$C_D A_{surf}(\frac{1}{2}\rho V_s^2) = N_{ch}(\dot{m}(U_{ex} - U_{in})$$

$$-\frac{1}{2}\rho(V_s^2 - U_{in}^2)(A_{in} - A_{ex}) + \Delta p_{ch} A_{ex}). \tag{2.25}$$

For further discussion, we will identify the three terms on the right-hand side of Eq. (2.25) as momentum thrust, pressure thrust 1 and pressure thrust 2. By inspection, the momentum thrust will only exist in the presence of an exit nozzle and will always contribute to propulsion of the vehicle. This thrust is a linear function which will increase proportional to constriction of the nozzle. The pressure thrust 1 term is also only present in the existence of a constricting nozzle. Since with a constricting nozzle A_{in} is always greater than A_{ex}, this thrust component can only assist the propulsion of the vehicle when the channel velocity is greater than the vehicle velocity. By contrast, the pressure thrust 2 term will always be present (except for special cases which will be discussed later). If the net change in pressure of the channel is positive, this component will assist propulsion of the vehicle; otherwise it will impede propulsion. From Eq. (2.16), it becomes apparent that the only time Δp_{ch} will be negative is when the drag component of the pressure

drop incurred across the thruster is greater than the pressure induced due to Lorentz forces.

2.4 Solution Procedures

The pressure at the entrance and exit of the MHD thruster are treated as unknowns but are coupled through Eq. (2.24). By predetermining vehicle and MHD channel dimensions, an optimal voltage for a given B and U_{in} is determined; voltage is calculated using Eq. (2.4) with η_{ind} set to .5. Δp_{th} is then calculated by Eq. (2.19) using an assumed value of s. By simple manipulation of the quadratic, Eq. (2.25) is in turn solved for V_s. However, for a given channel velocity, only two unique solutions exist for s which satisfy Eq. (2.18). One corresponds to unity and the other corresponds to a value less than unity. An iterative procedure is utilized to solve for the respective s. Once the solution has been obtained, the total thrust efficiency is determined by comparing thrust obtained versus electric power supplied.

$$\eta_t = \frac{N_{ch} T V_s}{P_e}. \tag{2.26}$$

Vehicle velocity and thruster efficiency versus channel velocity are used to evaluate the MHD thruster performance.

Chapter 3

ANALYTICAL RESULTS

3.1 Introduction

Performance calculations were based on two classes of underwater vehicles. The first class (class 1) is vehicles with dimensions similar to MK48 torpedoes. The common diameter and length were chosen to be 0.533 m and 6.1 m, respectively. The second class (class 2) is large submersibles such as submarines, with vessel diameter and length being 9.8 m and 83 m, respectively. Four rectangular MHD channels were attached symmetrically about the axis of each vehicle and the channel lengths were chosen to be two-thirds of the vehicle length. For first class vehicles, the electrode width and gap distance were 0.3 m and 0.1 m. For second class vehicles, the electrode width and gap distance were 3 m and 1 m, respectively.

Figure 3.1 shows the dependence of class 1 vehicle velocity on the magnetic field strength and the seawater conductivity. It indicates that the vehicle velocity increases proportionally with σB^2. The solid line represents the velocity performance at realistic seawater conditions. To achieve the torpedo speed of 50 - 70 knots, the magnetic field needs to be in the range of 15 to 20 T. Nevertheless, it points to the possibility of low speed applications in remotely operated vehicles (ROV) or underwater autonomous vehicles (UAV) with more realistic magnetic fields. By increasing the conductivity of seawater in the active volume of the MHD channels (shown as dashed line in Figure 3.1), the velocity can be increased linearly. Similar curves can be generated for class 2 vehicles.

For both class 1 and class 2 vehicles a detailed evaluation of the behavior of the MHD channel was conducted in the presence of 5, 7.5, 10, 12.5, 15, 17.5, and

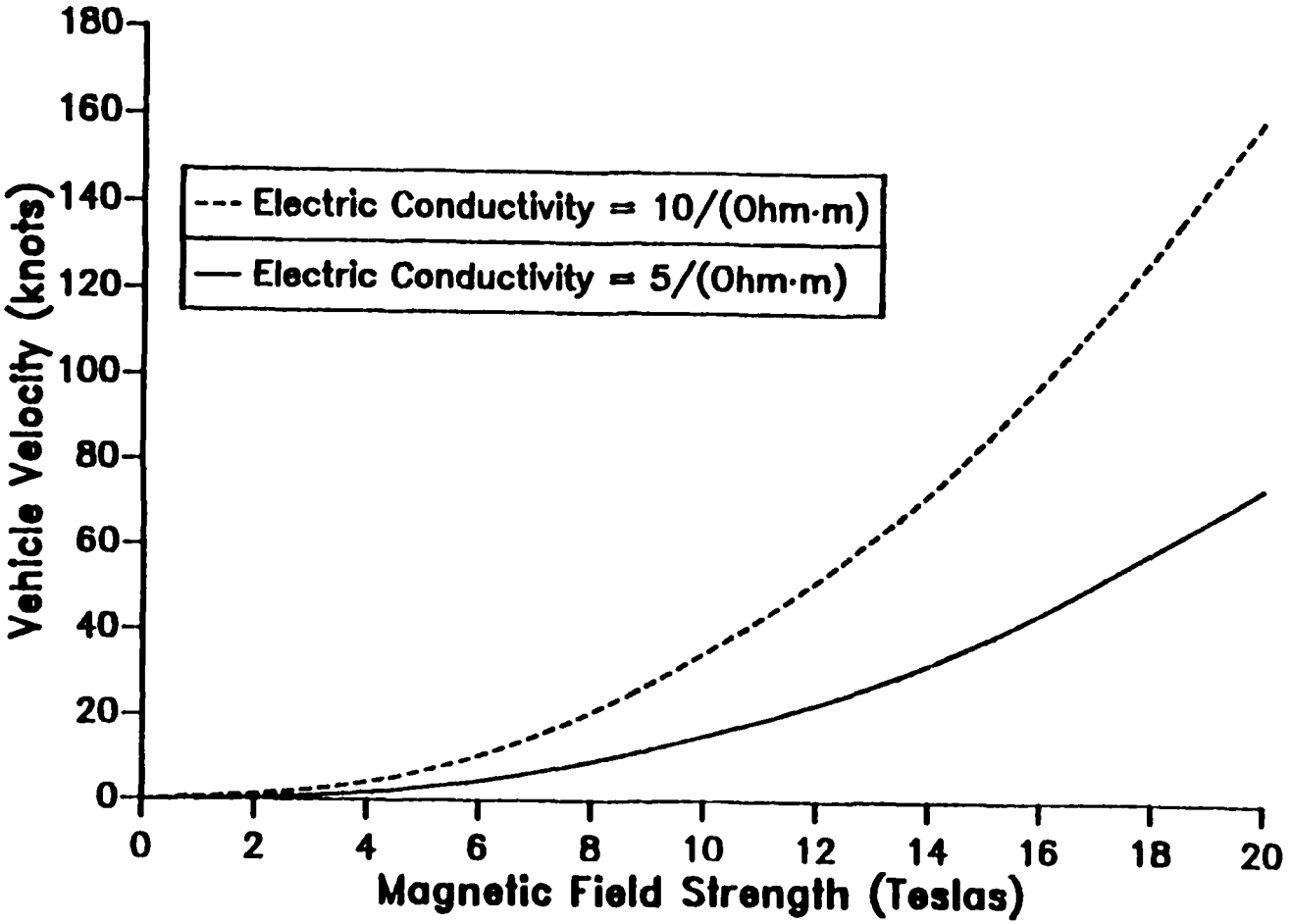

Figure 3.1 Velocity versus Magnetic Field for Class 1 Vehicles.

20 T magnetic fields. The performance of the system was found to be very similar and a detailed discussion of the results follows.

3.2 Class 1 Vehicle Performance

Figures 3.2 and 3.3 show the velocity and efficiency performances of class 1 vehicles versus the fluid velocity in the MHD channel at $B = 20\ T$. As discussed in section 2.3, there exist two distinct valid solutions for V_s at low U_{in} due to the quadratic nature of Eq. (2.24). One solution corresponds to the case of $s = 1$, where the MHD channel is straight and without any nozzle. The other solution corresponds to a s value less than 1. As shown in Fig. 3.3, both solutions often have invalid regions because η_t becomes larger than 0.5. This contradicts the imposed electric efficiency as discussed in section 2.1. At $B = 20\ T$, the solution without nozzle out-performs the solution with nozzle. Although the results do not show a valid solution without exit nozzle below $U_{in} = 23\ m/s$, a valid solution is expected if the η_t condition is relaxed by decreasing electrical efficiency (which corresponds to more Ohmic heating). The mechanical efficiency will also decrease (see Eq.(2.10)) and the thruster will perform at lower total efficiency (< 0.5). It is uncertain whether this configuration will out-perform the smooth nozzle solution.

Figure 3.4 shows the behavior of the thrust components in Eq. (24) versus channel velocity for class 1 vehicle with 20 T B field. To the RHS of the plot where s is equal to 1, the total thrust is simply equal to the pressure thrust 2 since the momentum thrust and pressure thrust 1 are both zero. It is noted that the momentum thrust is always greater than or equal to zero; pressure thrust 1 is always less than or equal to zero; and pressure thrust 2 can be greater or less than zero. The total thrust increases with increasing channel flow as physically expected.

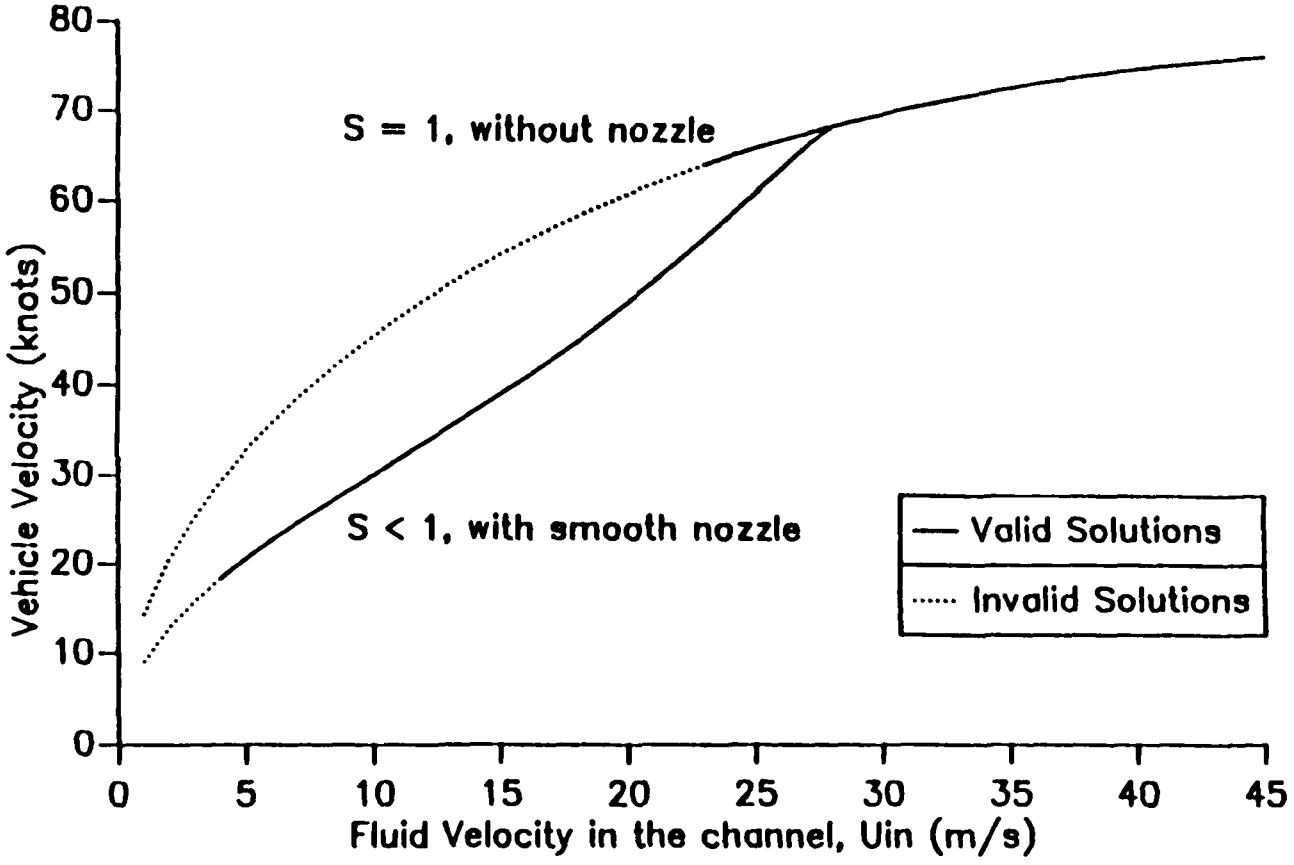

Figure 3.2 Velocity of Class 1 Vehicles at B = 20 T.

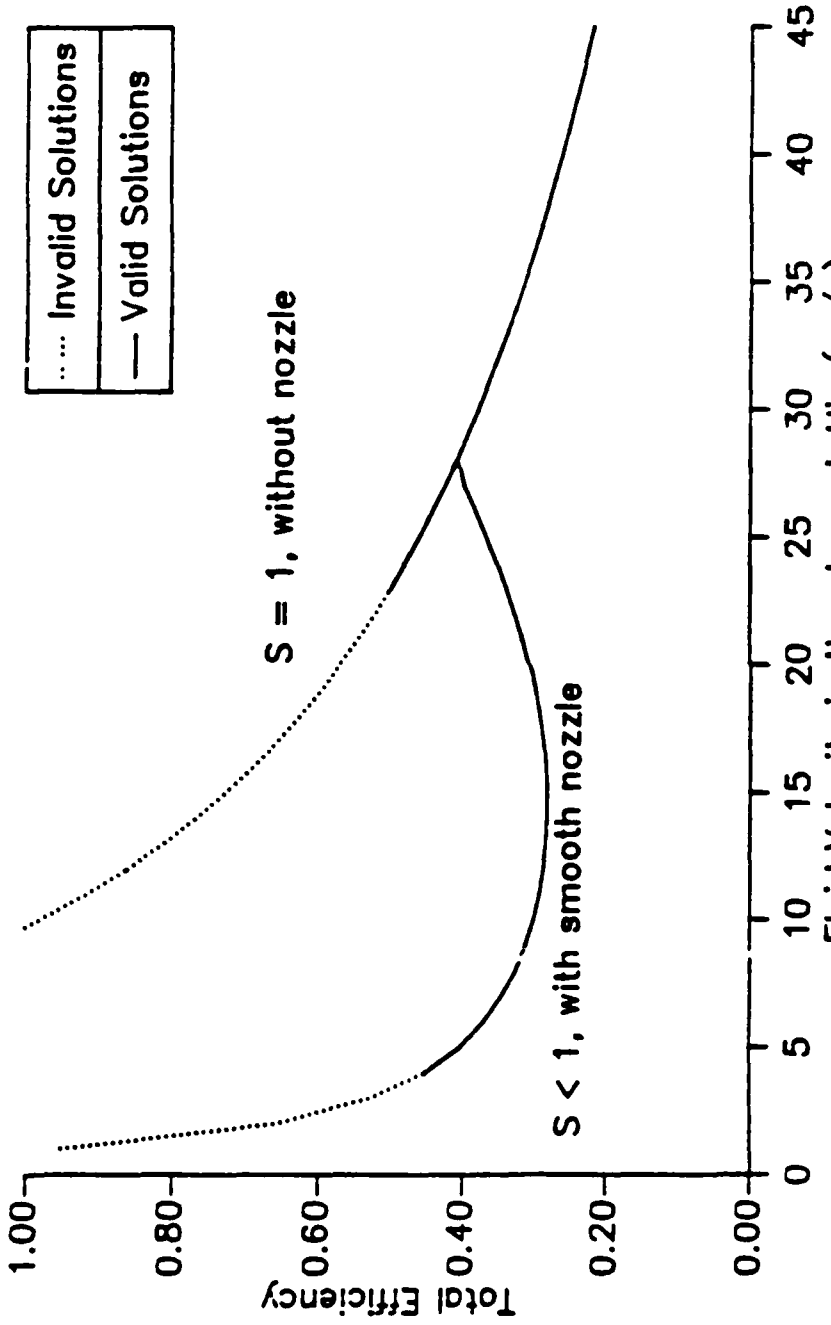

Figure 3.3 Total Efficiency of Class 1 Vehicles at $B = 20\ T$.

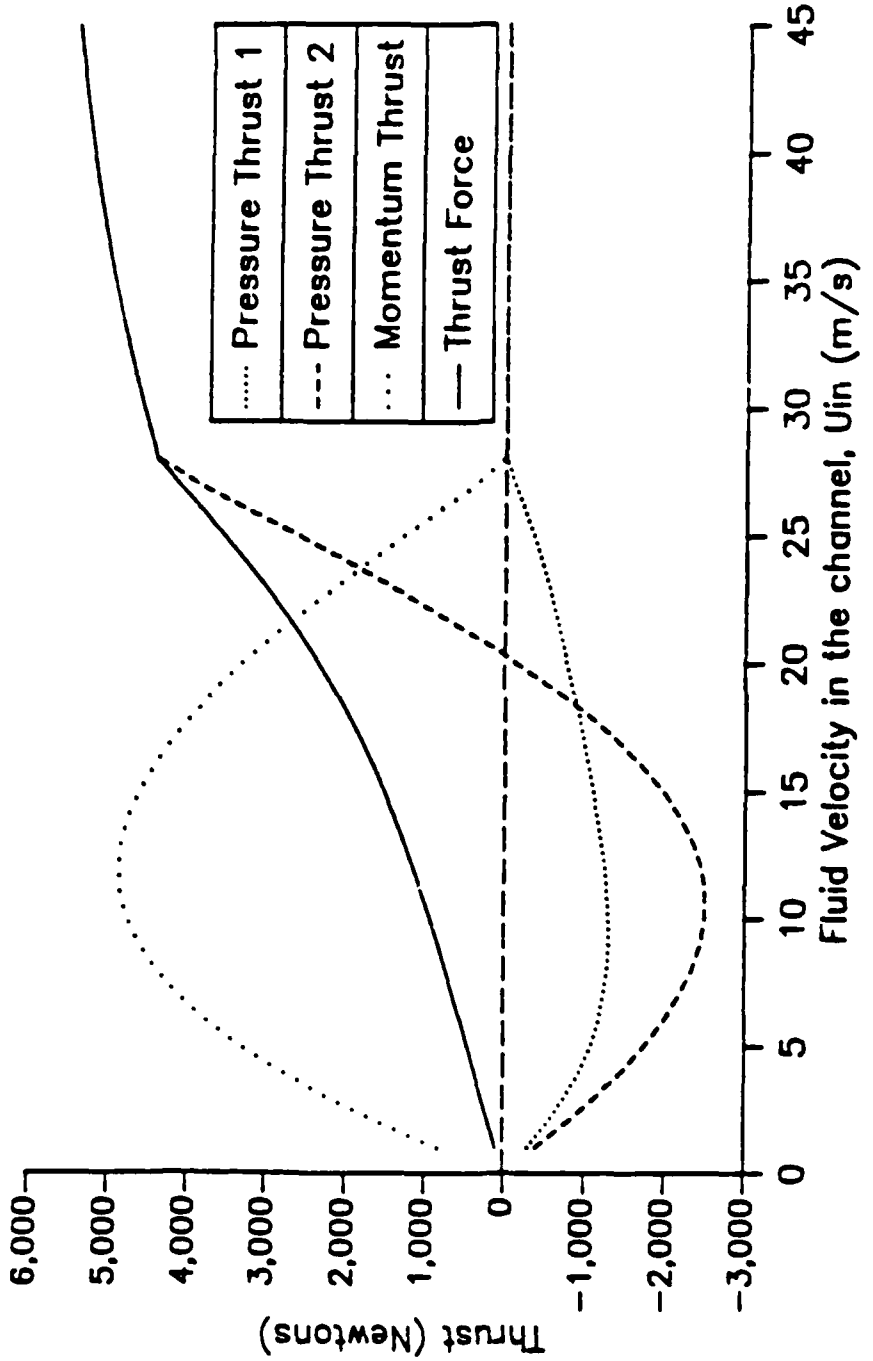

Figure 3.4 Thrust of Class 1 Vehicles at B = 20 T.

However, its increase is more rapid at low channel flow which corresponds to high momentum thrust at low nozzle area ratio. The behavior of these thrust components in relation to increasing channel velocity is the same for both classes of vehicles in the presence of the magnetic fields studied.

At $s = 1$, the only thrust applied to the system is due to increasing channel pressure via Lorentz force. From Eq. (2.9) it is evident that in the presence of a large magnetic field, a low voltage is a very effective configuration for propulsion; a vessel with thrusters operating at $U_{in} = 45\ m/s$ (which corresponds to $V = 180$ volts) attains a V_s of 76.7 knots with an efficiency of 0.218. As seen by Fig. 3.2 and 3.3 if a lower vehicle velocity is permissible and thereby a lower voltage, a much higher efficiency can be obtained. At $U_{in} = 30\ m/s$ (which corresponds to V = 120 volts), vehicle speed is 70.1 knots and efficiency is 0.38. This behavior is apparent in all thruster configurations.

Utilizing a smooth nozzle, the vehicle velocity will always remain below the corresponding velocity attained by thruster without nozzle (Fig. 3.2). This is due to the fact that the momentum thrust gained by a constricting exit nozzle is less than the drag forces exerted against the nozzle [Eq. (24)]. A fairly linear relation is observed between increasing channel velocity and increasing vehicle velocity. It should be noted that in this case s is also increasing linearly until the design without nozzle is reached ($U_{in} = 28\ m/s$).

As the magnetic field is decreased, the performance of the thruster is reduced as a function of σB^2. The 17.5 T and 15 T class 1 vehicle configurations mirror the results of 20 T case except that the gap between performance of thruster with or without nozzle has also decreased proportional to decreasing magnetic field. The solution without exit nozzle displays an optimum vehicle velocity/efficiency design

corresponding to an exit pressure closest to ambient. For $B = 17.5\ T$, optimum performance is at $U_{in} = 24m/s$, $\eta_t = 0.330$ and the corresponding vehicle velocity is 52.2 knots. For $B = 15\ T$, the optimum configuration is at $U_{in} = 13\ m/s$, $\eta_{total} = 0.331$, and the corresponding velocity is 30.6 knots.

As the magnetic field is decreased to 12.5 T, this trend continues until the solution with nozzle out-performs the solution without nozzle. The smooth nozzle thruster enables higher vehicle velocities while operating at approximately the same efficiency as the thruster without nozzle. In addition, optimal design criteria for the smooth exit nozzle are apparent. An optimum geometry exists when $U_{in} = 15$ m/s and the smooth nozzle is constricted such that the exit pressure is closest to ambient. This behavior is somewhat expected because the optimum nozzle design for a rocket exhaust nozzle (which functions under virtually the same principles) is at exhaust pressure equal or slightly greater than ambient pressure [25]. Also, $U_{in} = 32$ m/s is the configuration with the largest negative exit pressure and smallest vehicle velocity and thruster efficiency. Therefore exit pressures much smaller than ambient are normally undesirable.

In the case of $B = 10\ T$, the general behavior of the two solutions is the same as in the former case. However, the superior performance offered by the smooth nozzle increases significantly. A vessel velocity of 25 knots is attainable at 0.42 efficiency. In perspective, the thruster without exit nozzle obtains a maximum vehicle velocity of only 13 knots at 0.18 efficiency. In effect, the increase in thrust created by the momentum thrust term due to the smooth nozzle is substantially overcoming the negative pressure caused by the nozzle drag.

These trends continue below $B = 10\ T$, however the velocities attainable while maximizing efficiency drop significantly. For the case of 7.5 Teslas, vehicle velocities

and efficiencies obtainable are 6.7 and 19.9 knots with efficiencies of 0.179 and 0.33 for the thruster without and with smooth nozzle, respectively. For the case of $B = 5$ T, the thruster without exit nozzle attains a vehicle velocity of only 2 knots. By contrast utilizing a smooth nozzle ($s = .80$), a vehicle velocity of 13.7 knots can be reached at 0.26 efficiency.

3.3 Class 2 Vehicle Performance

Figures 3.5 and 3.6 show the velocity and efficiency performances of class 2 vehicles, i.e. submarines, in the presence of 5 T field. The general behavior of MHD thrusters for class 2 vehicles is the same as that observed in class 1 vehicles utilizing large B fields (>12.5 T). The smooth nozzle configuration attains vehicle velocities which increase linearly corresponding to increasing channel velocity. However, most of the solutions for B fields larger than 5 T and systems without nozzle contradict the imposed condition of optimal electric efficiency. Never the less for reasonable submarine propulsion applications, 5 T B field is sufficient. It is noted that reasonable submarine velocities can be achieved with a magnetic field of about 5 T. For a submarine having a 35 knots velocity, the total efficiency is about 0.355. This is due primarily to the large size of the MHD channels. For class 2 vehicles, even larger MHD channels than the ones currently under consideration are possible. That would result in further increases in vehicle velocities and total efficiency.

3.4 Small Vehicle Applications

The purpose of this study is to assess the feasibility of seawater MHD propulsion for underwater vehicles. It is commonly acknowledged that magnetic fields

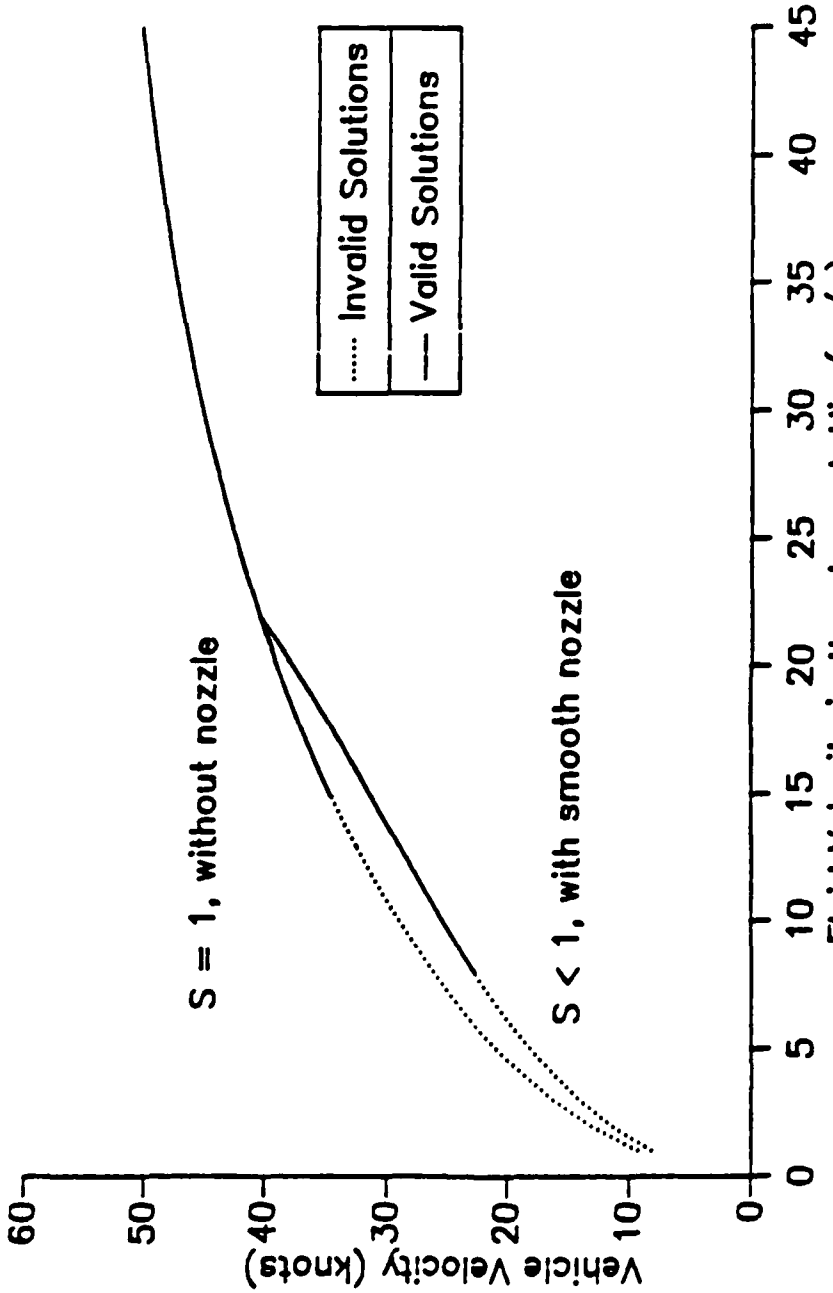

Figure 3.5 Velocity of Class 2 Vehicles at B = 5 T.

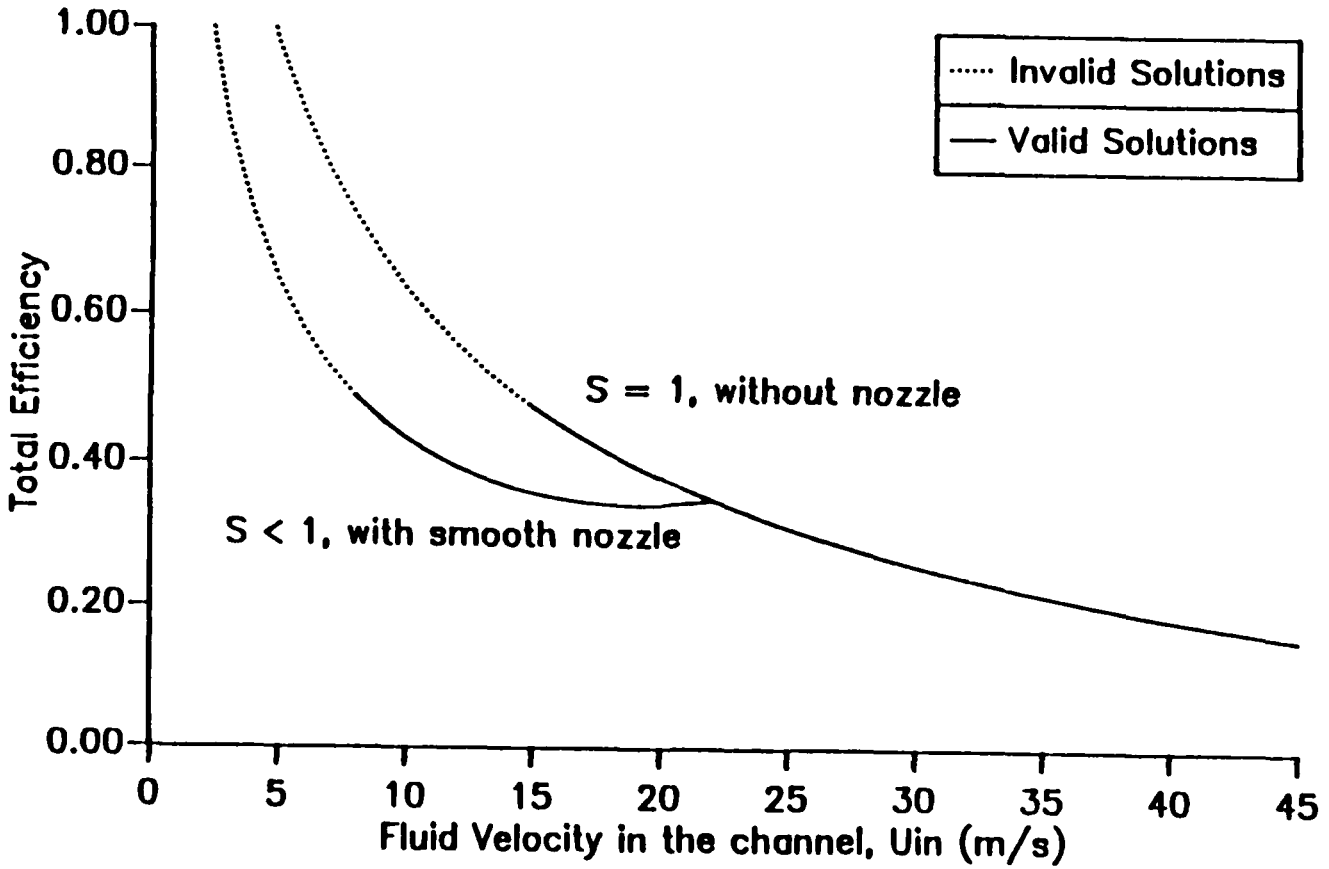

Figure 3.6 Total Efficiency of Class 2 Vehicles at B = 5 *T*.

higher than 10 T are, although achievable, not practical in large scale engineering applications. Therefore, for smaller vehicles, the possible applications of seawater MHD propulsion are in low speed ROV's and UAV's, with lower magnetic fields. The electric sources can be from batteries, fuel cells, or generators driven by the long endurance version of the stored chemical energy propulsion system (SCEPS) concept. The high magnetic fields required by the torpedo applications seem to be still somewhat out of the reach of current technologies.

3.5 Large Vehicle Applications

On the more encouraging side, a 5 T magnetic field appears to be adequately suited for propelling a class 2 submarine with reasonable speed, efficiency, and thrust as shown in Figures 3.5, 3.6, and 3.7. The electric power will most likely be nuclear driven. A class 2 submarine traveling at a speed of 36 knots would need 66 MW of electric power for its MHD channels. Assuming the Rankine cycle efficiency of the nuclear propulsion plant is 33%, the required reactor thermal power would be at least 200 MW. This, of course, does not include any other service power needed for the vehicle. Nevertheless as will be seen in the following discussion, it is compatible in power capacity to the current nuclear submarine technologies.

For this study, power available to the MHD thruster electric field is set at the shaft power provided by the existing power plants. Justification is as follows: Auxiliary systems in a typical submarine require approximately 4 $MW(e)$. This additional power should not be significantly effected by installation of a MHD thruster. Electrical losses in line resistances, electric generator inefficiencies, and magnet's cryogenic requirements should be approximately the same as mechanical losses such as gear reduction in present systems [29]. It should be noted that the 83 m length

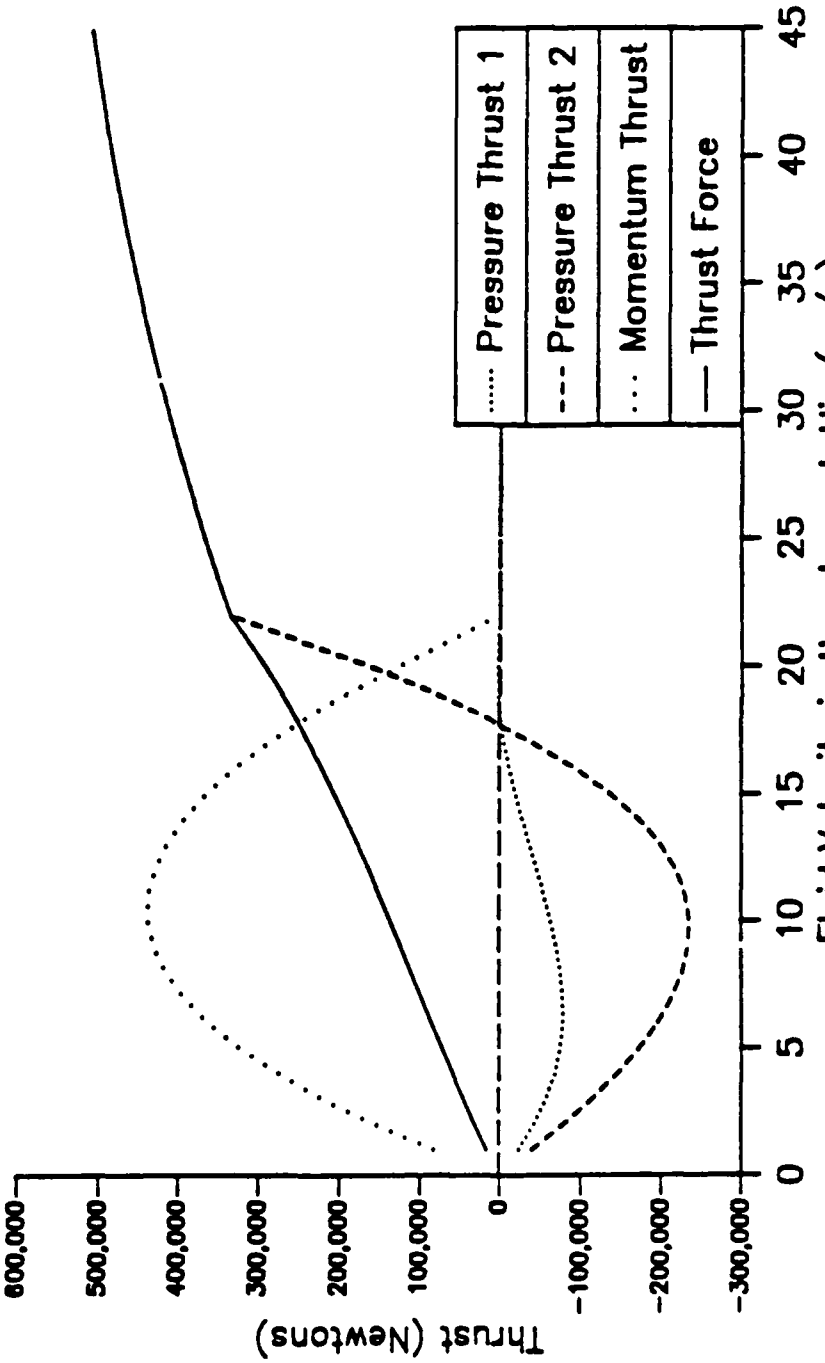

Figure 3.7 Thrust of Class 2 Vehicles at B = 5 T.

of the simulation model was chosen based on reduction of submarine proportions due to maximum incorporation of automated systems in conjunction with the MHD thruster. A good example is reduction in Soviet attack submarine size by 30.2% in the automated *Alfa* class [18]. The vessel would probably incur a further size reduction just by the removal of the mechanical drive.

Present Westinghouse nuclear plants, the SG6 and SG8, generate approximately 26.1 MW(shaft) and 42.3 MW(shaft), respectively. The two reactor system in the Soviet Typhoon class submarine has a shaft power of 120,000 *shp* (89.5 MW) [15]. Advanced reactor systems, such as Liquid Metal Fast Breeder Reactors (LMFBR) and High Temperature Gas Reactors (HTGR), are probably the most promising systems offering high power density and a reduction in reactor size. A lead-bismuth reactor is believed to be the powerplant of the *Alfa* class soviet submarine [18].

Typical ranges for diesel-electric power are on the range of 4,000 to 12,000 *shp* [3.0 to 8.9 $MW(e)$] [15]. Two new power systems, the Sterling engine and the fuel cell, are being developed by consortiums of Swedish and West German companies, respectively. The Sterling engine is piston gas driven device whose energy is obtained from an external heat source. This generator is rated at 100 KW and is presently being fielded in the Swedish Naecken class submarine. The fuel cell is based upon a chemical reaction between hydrogen stored in the cell and liquid oxygen but has not been fully developed [18].

Table 3.1 provides a comparison of anticipated MHD thruster performance versus that of screw type propulsion system for two submarine classes. For this study, the geometry of the MHD thrusters were maximized based upon 5 T magnetic field strength. Vessel thrust power was assumed to be proportional to electric

TABLE 3.1 Comparison of Velocities Obtainable by Propellors versus MHD Thrusters for *Los Angeles* and *Ohio* Class Submarines
Operating Depth = 30 m
B = 5 T, $\sigma = 5\ \Omega^{-1}m^{-1}$, $\rho = 1025\ kg \cdot m^{-3}$, $\eta_e = .5$

Vehicle Class	Vehicle Length (meters)	Vehicle Diameter (meters)	Nuclear Power Plant (shp)	Vehicle Speed w/ screws (knots)	Vehicle Speed w/ 4 MHD thrusters (knots)
*Los Angeles**	109.73	10.06	35,000 (26.1 MW)	30+	28.4†
*Ohio**	170.69	12.80	60,000 (42.3 MW)	20+	27.0‡

* Vessel Parameters are from reference 17.

† Thruster Geometry: D = 1.0 m, W = 2.40 m, and L = 73.15 m.

‡ Thruster Geometry: D = 1.0 m, W = 2.75 m, and L = 113.79 m.

power available to the thruster. As is apparent from Table 3.1, the MHD thruster can propel large submersibles with velocities comparable to screw type propulsion systems using existing nuclear powerplants.

To obtain respectable vehicle velocities with a 5 T B field, a power supply of at least 20 MW is required. The only present power supplies generating this much continuous electrical energy are nuclear. Lower power levels will not attain vehicle speeds comparable to modern vessels. Nuclear power also offers the potential of natural circulation at low load levels. Since this configuration would have no moving parts, the submarine would be virtually silent. Also, vessel speeds above 42 knots are feasible if MHD thruster, advanced reactor system, and automated control are incorporated together. The reduction in size can also help the submarine avoid acoustical and magnetic field anomaly detectors. In addition, a hybrid submarine having both the propeller screws and MHD channels may offer some strategic merits in underwater warfare.

Chapter 4

ELECTROLYSIS OF SEAWATER

4.1 Introduction

Seawater passes electric current through ionic conductance. When used as a medium for d.c. current, seawater incurs several processes which may adversely affect its performance as a conductor. These include production of microbubbles at electrode surface, overvoltage, and electrode corrosion. In conductivity measurements of electrolytic solutions, these problems are overcome by utilizing an alternating current (a.c.) bridge operating at frequencies of 1000 to 4000 hertz [30] and agitating the solution with a stirring device. Unfortunately the the d.c. thruster design inherently cannot use alternating current. Therefore to analyze the MHD d.c. thruster concept, these effects must be explored.

The objective of this chapter is to provide the reader with enough information regarding the ionic conductance process in order to gain a fundamental understanding. Results from recent research in areas applicable to seawater MHD propulsion are then presented in order to better understand the design of and results obtained from the experimental apparatus described in chapters 5 and 6.

4.2 Microbubble Effects

Due to the nature of ionic conductance, negatively and positively charged ions will migrate to the anode and cathode, respectively. With a seawater solution, these ions will be in the form of hydrogen, oxygen, and chlorine: hydrogen gas will evolve at the cathode while chlorine and/or oxygen will evolve at the anode. Figure 4.1 illustrates the electrolysis of seawater.

SEA-WATER ELECTROLYSIS IN A FLOWING CONDITION

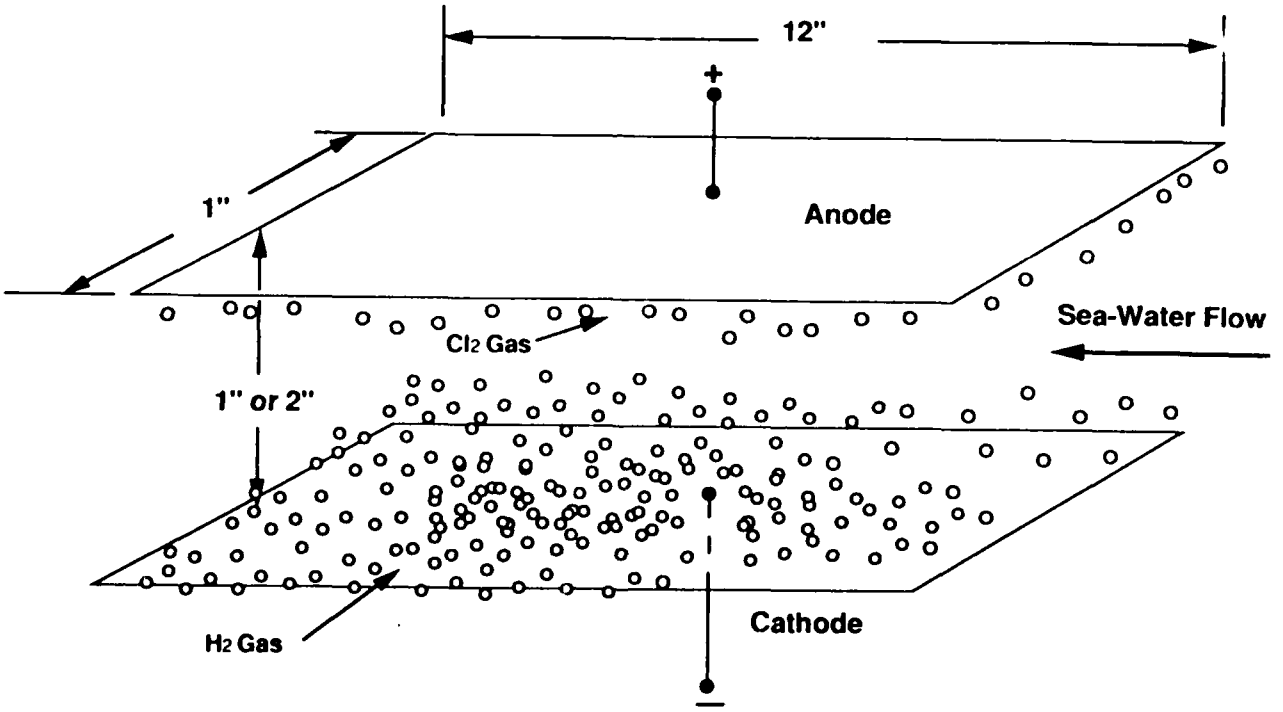

Figure 4.1 Seawater Electrolysis in a Flowing Condition.

If the channel geometry of the MHD thruster is fixed, then the generation of microbubbles will result in a displacement of conducting medium and replacement with nonconductive gaseous products (such as H_2, O_2 and Cl_2). The resulting decrease in the volume of conducting medium will result in an increase in global resistance. This effect can be inferred from Eq. (2.2). As will be discussed in section 4.6, the generation of microbubbles may also hinder conductance by increasing diffusion overvoltage.

Since the microbubble generation is directly proportional to current, its effects on conductance should be reduced if the velocity of the electrolyte traveling between the two electrode plates is increased. This would be contributed to faster removal rate of the microbubbles. Therefore in the presence of a potential difference between electrodes, the electric current conducted by the seawater in a MHD duct should increase with increasing flow rates.

4.3 Mechanism of Electrode - Electrolyte Interaction

The voltage drop in a MHD channel is due to two primary effects. The first is incurred due to the Ohmic losses in the solution and are fairly well understood. The second, overvoltages, is caused by the electrode-electrolyte interface. These effects, as will be seen, are functions of both electrode and electrolyte composition. If the potential at the cathode is represented by E_c and the potential of the anode is E_a, then the voltage drop, ΔV, is described by,

$$\Delta V = E_a - E_c = IR + \eta, \tag{4.1}$$

The Ohmic loss, IR, is energy transformed to heat in the electrolytic solution and

can be evaluated using Eqs. (2.1) and (2.2). η represents the losses due to overpotential (overvoltage).

Before the forms of overpotential can be addressed, the mechanism of electrode-electrolyte interaction must be understood. As presented by W. Moore [30], an electrode reaction proceeds as follows:

1. diffusion of reactants to electrode;
2. reaction in the layer of solution adjacent to electrode;
3. absorption of reactants on electrode surface;
4. transfer of electrons to or from absorbed reactant species;
5. desorption of products from electrode;
6. reaction in layer of solution adjacent to electrode;
7. diffusion of products away from electrode. (page 553)

It should be noted that steps 2 and 6 do not always occur during electrode processes. In d.c. thruster applications, the current traveling through the seawater is provided by an external source. Therefore, both cathodic and anodic reactions will occur. Each independently following the above mentioned steps.

4.4 The Cathode Reactions

The cathode mechanism can follow two courses. First method as presented by Koryta and Dvořák [31] begins with ionization of a water molecule.

$$H_2O \rightleftharpoons OH^- + H^+. \tag{4.2}$$

The H^+ ion is then attracted to the cathode where it is absorbed on the surface (H_{abs}).

$$H^+ + e^- \rightleftharpoons H_{abs}. \tag{4.3}$$

Following with a chemical reaction,

$$2H_{abs} \rightleftharpoons H_2 \uparrow, \tag{4.4}$$

or an electrode reaction,

$$H_{abs} + H_3O^+ + e^- \rightleftharpoons H_2 \uparrow + H_2O, \tag{4.5}$$

the hydrogen is desorbed and the H_2 microbubble is created. The preference for reaction given by Eq. (4.4) or that of (4.5) based on various electrode materials is provided by Koryta and Dvořák [31].

The second method for H_2 production, as outlined by Bennett [32], is by the migration of Na^+ ions to the cathode. The Na^+ then gains a electron,

$$Na^+ + e^- \rightleftharpoons Na_{abs}, \tag{4.6}$$

and combines with a water molecule to generate hydrogen,

$$2Na_{abs} + 2H_2O \rightleftharpoons 2NaOH + H_2 \uparrow . \tag{4.7}$$

4.5 The Anode Reactions

At the anode, both chlorine and oxygen evolution are possible. Of the negatively charged ions with most typical electrode materials, chlorine is preferred. Two major factors contribute to this. First, evolution of oxygen or chlorine at the anode causes the solution at the electrolyte-electrode boundary to become highly acidic (on the order of pH 1-2). This causes an increase in thermodynamic voltage for oxygen whereas chlorine evolution is unaffected. The second factor favoring chlorine production is its lower overpotential at typical current densities [32].

For oxygen generation, the reaction can proceed through various sequences. The first step is migration of water molecules to the anode surface where they are absorbed. The reactions then progress as follows:

$$H_2O_{abs} \rightleftharpoons OH_{abs} + H^+ + e^-. \tag{4.8}$$

The reaction proceeds as,

$$OH_{abs} \rightleftharpoons O_{abs} + H^+ + e^-. \tag{4.9}$$

Finally,

$$2O_{abs} \rightleftharpoons O_2 \uparrow . \tag{4.10}$$

For chlorine production, the chlorine ions diffuse to the cathode, where they are absorbed.

$$Cl^- \rightleftharpoons Cl_{abs} + e^-, \tag{4.11}$$

$$Cl_{abs} \rightleftharpoons Cl_2 \uparrow . \tag{4.12}$$

The chlorine gas than immediately reacts with water.

$$Cl_2 + H_2O \rightleftharpoons HClO + Cl^- + H^+, \tag{4.13}$$

$$HClO \rightleftharpoons ClO^- + H^+. \tag{4.14}$$

4.6 Overpotential

The overpotential incurred during a change in current carrying medium such as electron conductor (metal) to ion conductor (electrolyte) or vice versa can be in several different forms. Of these, activation (η_A) and diffusion (η_D) overpotentials are usually most significant.

$$\eta = \eta_A + \eta_D + ... \tag{4.15}$$

The behaviors of the different forms of overpotentials are of a fairly complex nature and numerous theories have been developed to better understand and predict them. The purpose of this work is to gain enough insight into overpotential in order to understand its impact on the experimental results obtained in chapter 6 and therefore its influence on feasibility of the MHD thruster. The interested reader desiring a more detailed discussion of overpotential is recommended to the treatise presented in references 30, 31 and 33.

Activation overpotential (also known as transfer overpotential) is caused by a slow electron transfer from metal to electrolyte or vice versa due to a high activation energy required for the transfer. A significant increase of the electrode potential above the equilibrium value is required to decrease the activation energy thereby increasing the rate of electron transport [31]. This behavior is known to follow the Tafel equation [30,31,33-35],

$$\eta_A = a + bLog(i), \tag{4.16}$$

where a is a constant corresponding to the chemical activation energy of the electrode-electrolyte reaction and reactant concentrations. b is a parameter with linear dependence on temperature, and i is current density.

The Tafel equation illustrates an exponential growth of current with linearly increasing potential difference: one would expect a decrease in the significance of activation overvoltage with increasing current densities. Therefore the influence of activation overpotential in MHD thruster performance is expected to be minimal due to the relatively high electric current densities in the MHD channel and the good electrolytic properties of the predominantly $NaCl$ solute in seawater.

Diffusion overvoltage occurs when the slow diffusion of reactants to the vicinity of electrode plates limits the electrochemical reaction rate. This also corresponds to an increase in reaction products at electrodes due to slow mass transfer by diffusion [36]. Diffusion overvoltage is normally minimized by extreme agitation of the electrolytic fluid to increase mass transfer. Since the seawater in a MHD duct is highly turbulent under operating conditions, its overpotential is not expected to be very large and should decrease with increasing channel velocities.

It should be noted that due to diffusion limitation of reactants there exists a limiting current which cannot be exceeded by increasing voltage (unless another substance in the electrolyte can be ionized and thereby carrying more current). The current density in the thruster channel is not expected to be even close to this limiting parameter.

4.7 Studies of Seawater Electrode Performance

A second area of primary interest for feasibility of MHD thruster applications is determination of the best material for the electrodes. The electrodes need to resist

the corrosive effects of seawater. Also, deposits will accumulate on the anodes and cathodes due to electrolytic processes. A possible cleaning technique is to simply reverse the polarity of the electrodes. If this is done in conjunction with magnetic field reversal, the direction and magnitude of thrust supplied by the MHD propulsion mechanism will not be affected. Thus, the optimal material to be used in electrode plate design is one that functions well as both cathode and anode. This may also be necessary because electric field reversal is potentially the easiest method to provide thrust reversal which will probably be required to facilitate vehicle maneuvers.

In torpedo applications, the MHD thruster only needs to function once and for a relatively short time duration. Therefore "sacrificial electrodes" can be used. These are electrodes which erode while the electrolysis is taking place. The erosion process enhances conductivity thereby improving thruster performance.

Previous experiments have shown that certain metals do not function well as electrodes for seawater. During separate experiments conducted by L. Whitehead et al. and D. R. Wilson in the mid to late 1960s, the highly corrosive effects of seawater electrolysis were observed. Specifically, stainless steel electrodes were found to be completely corroded within only one minute of operation in the presence of an electric field of 3 $KV \cdot m^{-1}$ and electric current density of 20,000 $A \cdot m^{-2}$ to 80,000 $A \cdot m^{-2}$ [37]. Aluminum was evaluated in by S. Way and C. Devlin and also found to be adversely affected as a cathode by appearance of chloride deposits [6]. According to A. Iwata and Y. Saji [9], two by-products which degrade electrode performance are sodium hypochlorite ($NaOCl$) and magnesium hydroxide ($Mg(OH)_2$). These are produced by the following electrochemical reactions:

$$2Cl^- \rightleftharpoons Cl_2 + 2e^-, \tag{4.17}$$

$$Cl_2 + 2NaOH \rightleftharpoons 2NaOCl + H_2 \uparrow, \tag{4.18}$$

$$Mg^{2+} + 2NaOH \rightleftharpoons 2Na^{+} + Mg(OH)_2, \tag{4.19}$$

In 1980, an oxygen selective anode was found which will evolve oxygen with a reported 99+% efficiency. This electrode uses a manganese-dioxide coating on a metal substrate [32]. The coating appears to act as a diffusion barrier to chloride ions but does not affect oxygen. More recent research by S. Motoo and N. Furuya has lead to the development of a gas diffusion electrode for cathode applications. Their electrode allowed the super-saturated hydrogen formed on the electrolyte side of the cathode to diffuse through the electrode and be accumulated in a collection chamber. This process suppresses hydrogen gas evolution on the cathode-electrolyte boundary in the presence of up to 2 $A \cdot cm^{-2}$. At a current density of 8 $A \cdot cm^{-2}$ and up to 1 $ml \cdot s^{-1}cm^{-2}$ of the gas dissusion rate was able to be accumulated in the collection chamber [38].

In April 1989, M. Hiroi et al. conducted a systematic evaluation of performances of various anodes for seawater MHD applications. The anodes they evaluated were DSE(Ti/RuO_2), DSE(Ti/IrO_2), Pt plate, Ti/Pt (sputtering), glassy carbon, and three versions of DSE/MnO_2 (manufactured using Bennett method, thermal decomposition, and $MnSO_4 - H_2SO_4$ bath). Based on their experiments, the most promising electrode was a DSE coated with MnO_2 which achieved approximately a 74%-91% oxygen evolution efficiency in the presence of a current density of 100-500 $mA \cdot cm^{-2}$. The oxygen evolution efficiency is attributed primarily to the presence of a higher chlorine overpotential [39].

Chapter 5

TEST LOOP APPARATUS

5.1 Test Facility Description

In construction of the test facility a number of factors were considered. The system needed to attain flow rates of 100 gallons per minute and withstand the corrosive attacks of sea salt as well as a 5% seeding of sulfuric acid. The circulation system's primary components consist of a reservoir tank, primary test line, and a filtration bypass line. Polyvinyl Chloride (PVC) class 12454-B piping was used to construct the system. A fiber-glass centrifugal pump facilitates the solution flow in the lines (see Figure 5.1).

The reservoir, constructed from fiberglass, is designed to hold 150 gallons. An active ventilation system at the top of the reservoir tank removes any potentially hazardous gases that may be emitted during testing. A mixing motor mounted on top of the reservoir (beside the ventilation system) serves to ensure uniform mixing of the sea salt solution. At the bottom of the tank, a 3" diameter PVC piping exits towards the centrifugal pump.

The pump used to propel the salt solution within the system is a 10 horsepower, 3,500 *rpm* Sethco fiberglass centrifugal pump model CVR $1\frac{1}{2}\times3\times6$. The centrifugal pump is regulated by a Parametrics Parajust motor controller model G-04-200-A00. A 150 psi gauge located at the discharge line of the pump monitors the head at the pump. The solution upon being propelled by the pump may either enter the bypass line or the primary test line.

The bypass line, made of PVC, enables fine filtration of the solution when needed. The filter used is a Shelco Filter model 5FOS-80, composed of five phenolic

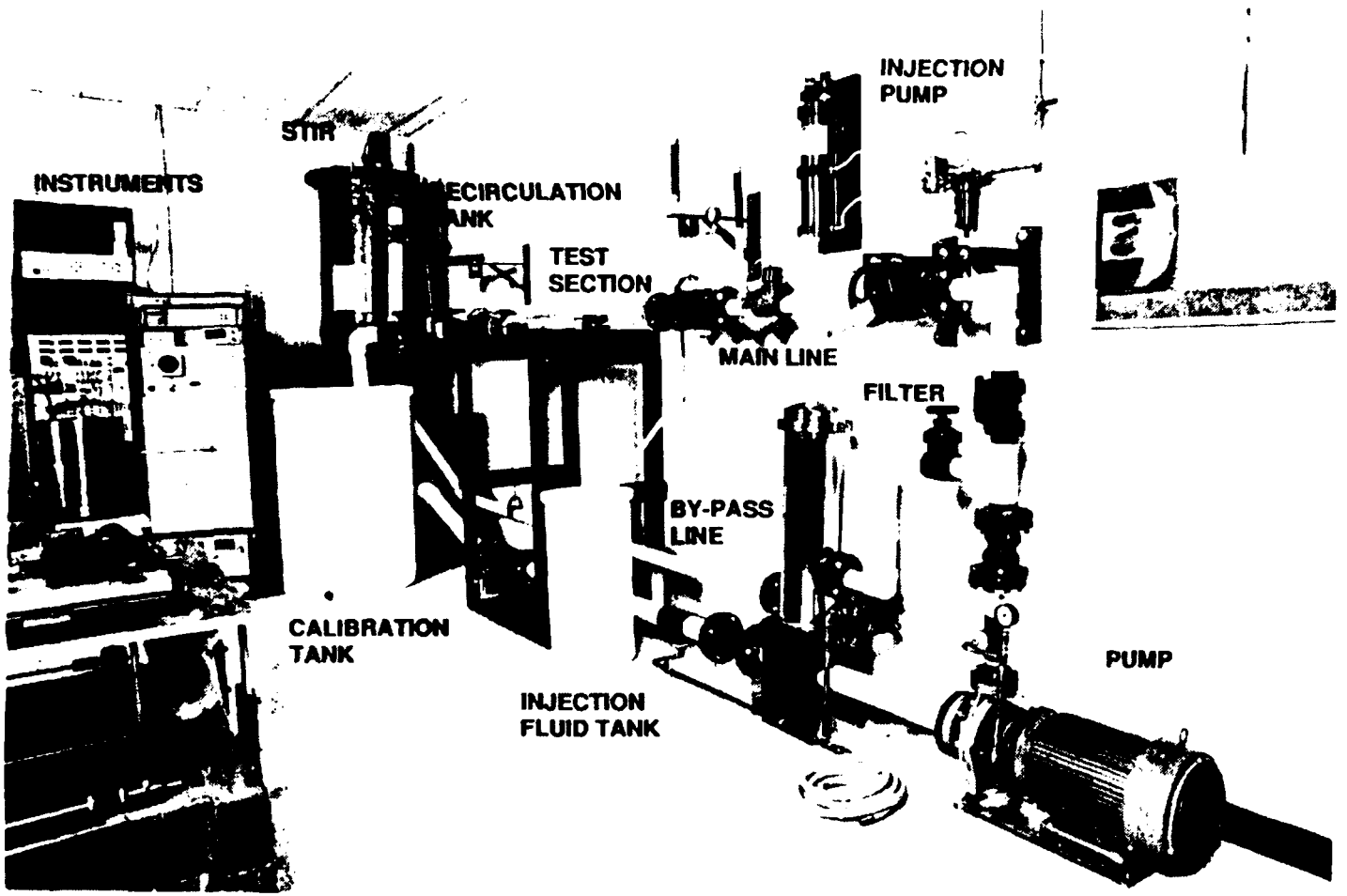

Figure 5.1 Synthetic Seawater Electrolysis Test Facility.

resin binder cartridges housed in a 306 stainless steel casing. A gate valve controls flow through the bypass line. During experimental runs this valve may be closed to allow the solution to flow through the primary test line only.

The primary line contains the test section, and flow meter. The flow meter, located upstream of the test section, is a Data Industrial model 220PD-2 sensor coupled with a model 1000 Digital Flow monitor. The metering system has a flow range of 0 to 200 *gpm*. Flow rate through the primary line is controlled in two ways. The first is simply by the parajust controller which regulates the speed of centrifugal pump previously mentioned. The second method of flow rate control is by the Saunders diaphram high flow valve model 5922-11-KW located upstream of both the flow meter and test section. Downstream from the test section, the flow runs back into the reservoir tank or may be diverted into a 100 gallon Neoprene tank for calibrating purposes.

In order to damp out vibration in the circuit, vibration isolation devices were placed directly upstream and downstream of the test section as well as upstream and downstream of the centrifugal pump. In addition, vibration isolation devices are used to isolate the entire system from its surroundings.

5.2 Test Section Description

Design criteria for the test section was to provide a mechanism for passing electrical current through seawater with a current density on the order of .4 $A \cdot cm^2$. The section needed to allow for visual observation of the electrolysis and for pressure observation across the electrode length. Figure 5.2 shows 2"$\times$1" rectangular duct test section at the electrodes.

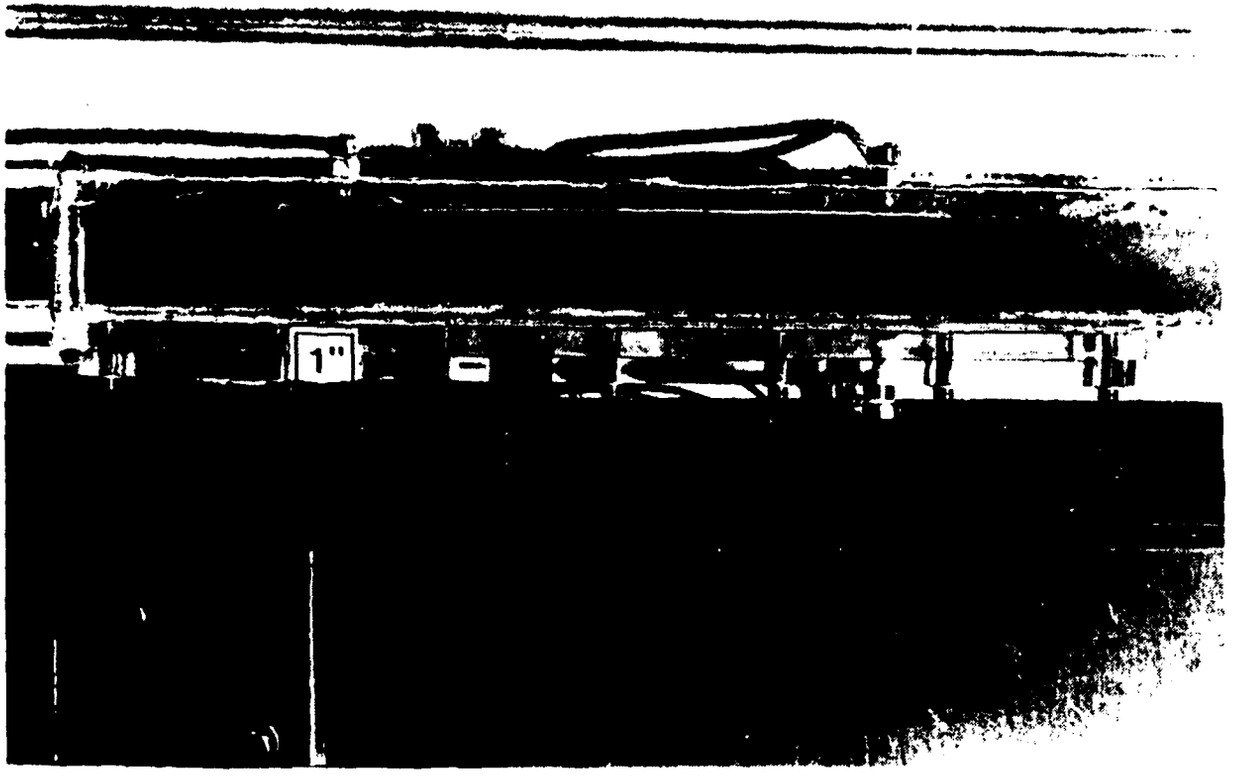

Figure 5.2 View of 2"×1" Test Section at the Electrodes.

Three different test sections were constucted. They were built from transparent acrylic using a rectangular duct configuration. Two of the sections utilize a two inch electrode gap while the other has a one inch electrode gap. A one inch distance is allowed between insolating walls. The electrode surfaces are one inch by twelve inches with pressure ports placed one inch upstream and downstream of the electrode's leading and trailing edges. A Validyne model DP15 pressure transducer with a 1.25 psi diaphram is used to observe pressure differential across the electrodes. The accuracy of this device is $\pm$ .25% of full scale.

To reduce head loss and prevent cavitation, a smoothly constricting nozzle is placed upstream of the test section to facilitate transition of the flow from 2" diameter pipe to the rectangular duct before reaching the electrodes. The flow is then allowed a distance of approximately 20 times the duct equivalent diameter to become fully developed. A smoothly expanding diffuser is placed downstream of the electrodes to allow smooth transition from the rectangular duct to 3" diameter pipe.

To provide the required current to the electrodes, an Electronic Measurements model TCR 30 SCR-regulated d.c. power supply is used. The power supply is capable of providing a maximum of 125 A at 40 volts. Two panel meters are built into the unit to monitor voltage and current at the load. At low currents and voltages (below 5 A and 5 volts, respectively) the TCR 30 panel meters were found to be inaccurate. To alleviate the voltage inaccuracy, a Hewlett Packard model 3456A digital voltometer was placed in parallel with the electrode plates to measure potential difference. This unit had an accuracy of $\pm$ 1 micro-volt. However, experimental fluctuations limited the accuracy to $\pm$ 100 micro volt. In later experiments, the accuracy of current measurement at low Amperage improved

by adding two 10 A ammeters in series with the positive terminals. This allows accurate readings down to .01 milli-amps.

5.3 Electrode Plate Design

Dimensions of the electrode surface and gap distance were based on achieving a current density of 0.4 $A \cdot cm^{-2}$ with a maximum potential difference of 40 volts. Seawater specific conductivity, σ, was conservatively estimated at 5 $\Omega^{-1} \cdot m^{-1}$. Using Ohm's law ($V = IR$) where resistance R is determined by,

$$R = \frac{\rho l}{A}. \tag{5.1}$$

ρ is the specific resistance, l is the distance between electrodes and A is the surface area of an electrode. It should be noted that the inverse of ρ is specific conductance. The electrode gap was calculated to be 2". To minimize current supply requirements and simplify test section construction, the electrode surface area was set to twelve inches in length by 1" width.

Each electrode type required a different mechanism for mounting of electrode leads. For the platinum plated copper, two holes were drilled through the 1"×12" copper plate and silver-soldered to the plate. The entire structure was then electro-plated with platinum (approximately 50 μ inch thick for 1"×1" test section electrodes and 75 μ inches thick for the two inch by one inch test section electrodes).

The electrode leads were connected to the 1"×12"×$\frac{1}{4}$" carbon plate by gluing a copper structure described above to the back side of the carbon surface. To accomplish this, the carbon and copper surfaces were first thoroughly cleaned and then joined using a TRA-DUCT 2902 conductive silver paste epoxy adhesive. The

assembly was baked at over $110°C$ for one hour to improve adhesive performance ($R \approx 8 \times 10^{-5}\Omega \cdot cm$). The primary ingredient of the adhesive is silver. It should be noted that copper was not exposed to the ·ynthetic seawater.

Finally, electrical connections for the Hastelloy-C electrode plate were formed by welding two Hastelloy-C bolts to the back of the plate. Some scoring due to the welding process was noticeable on the electrode surface.

5.4 "Sea-Salt" Solution Description

An aqueous solution of "Sea-Salt" manufactured by Lake Products Company was used as the electrolyte. This mixture was chosen because it meets American Standard for Testing Materials Standard D-1141-52-Formula A, Table 1, Section 4 for duplication of ocean water (an ingredient listing is given in Table 5.1). Table 5.2 gives a comparison by percent solid weight between "Sea-Salt" mix and real seawater. As can be seen, the "Sea-Salt" mix consistency is in good agreement with actual seawater.

5.5 System Calibration

The total system and reservoir capacities were calibrated twice upon completion of the loop construction. This was accomplished by utilizing a weight scale, 100 gallon neoprene tank, and positive displacement pump. With loop entirely dry, the neoprene tank was placed on weight scale and filled with water. Water was then supplied to the reservoir in one gallon increments by weight utilizing a positive displacement pump. A strip running vertically on the outside of tank was calibrated accordingly up to 145 gallons. After completion of reservoir calibration, the entire

TABLE 5.1 Composition of "Sea-Salt" Mix

Composition	Percent by Weight (%)	Density (grams/litre)
$NaCl$	58.490	24.530
$MgCl_2 \cdot 6H_2O$	26.460	5.200
Na_2SO_4	9.750	4.090
$CaCl_2$	2.765	1.160
KCl	1.645	.695
$NaHCO_3$	.477	.201
KBr	.238	.101
H_3BO_3	.071	.027
$SrCl_2 \cdot 6H_2O$	.695	.025
NaF	.007	.003

TABLE 5.2 Comparison of "Sea-Salt" Versus Real Seawater

Element	"Sea-Salt" % Total Weight	Seawater Parts per Million†	Seawater % Solids	"Sea-Salt" % Solids
Na	26.305	10,561	.324066	.324125
Cl	47.273	18,980	.582405	.582488
Mg	3.160	1,272	.039032	.038940
S	2.200	884	.027126	.027108
Ca	0.999	400	.012274	.012309
K	0.941	380	.011660	.011595
Br	0.160	65	.001995	.001971
B	0.012	4.6	.000141	.000148
Sr	0.036	13	.000399	.000444
F	0.003	1.4	.000043	.000037
C	0.068	~28	.000859	.000838

† The partial listing of the composition of seawater is from reference 40.

system was flooded and all air in plumbing evacuated. A second scale on the reservoir was then marked with the level of 145 gallons corresponding to electrolyte capacity of total system. Using the same procedure as outlined above, the entire system capacity was calibrated up to its 166 gallon maximum.

The flow meter was calibrated in a similar fashion as the tank. The 100 gallon neoprene tank was placed on the weight scale and positioned so that the calibration line downstream of the test section exhausted into it. Then the circulation system was filled to capacity and the circulation pump set to desired operating speed. At this point the ball valve downstream of the test section on the tank return line would be closed. Simultaneously, the calibration line ball valve would be opened directing all flow into the 100 gallon neoprene tank. After 15 seconds for high flow rates and 30 seconds for low flow rates, flow would be redirected back to the recirculation tank. Typically this process was repeated six times for each flow rate evaluated. Flow rate range was 10 *gpm* to 140+ *gpm* and calibration was done in 10 *gpm* increments. To prevent damage to the test section during pressure surge (which occurred during the valve switching procedure), a 2" PVC circular section was installed in place of the test section.

The pressure transducer is calibrated from 0 to 1.25 psi using an open water manometer. The conductivity meter, an Omega CDCN-36 or a CDPM-70, was benchmarked against KCl solutions of known conductivity. Due to temperature changes of the "Sea-salt" solution and meter inconsistencies, this was required before and after each trial. A strip chart recorder was used to record voltage, current, and change in pressure. The sensitivity settings on the chart recorder were set to appropriate levels. The pH meter, a Digisense model no 5994, was calibrated using buffer solutions of 4.1 and 10.04.

5.6 "Sea-Salt" Solution Preparation Procedure

Before mixing the electrolyte, all necessary calibration must be completed and the entire system must be thoroughly cleaned. This is accomplished by partially filling the reservoir with tap water and using the centrifugal pump to flush both test section and filtration lines. After the system is completely drained, the following steps are taken to prepare the synthetic seawater:

1. Tap water (140 gallons) is added to the reservoir. Using a 5 micron filter in line with the plumbing, water is pre-filtered before entering the tank. This preliminary filtration step was found necessary to remove large sediments found in tap water. Tap water was found to suffice since its conductivity was measured to be approximately 3 orders of magnetude less than the "Sea-Salt" solution—and therefore negligable.

2. "Sea-Salt" mix at a ratio of 41.953 grams per litre is added to make a 140 gallon mix. Then water is added to the tank to bring electrolyte solution to 140 gallons.

3. Using mixing motor, solution is stirred until all particles are dissolved.

4. Test line and bypass line are flooded. All air pockets are removed from system by operating circulation pump at low speed. Trapped air is removed from pressure gauge and bleeder valves.

5. Amount of seawater required to fill system to 166 gallon capacity is determined. Then proportional amounts of salt and water are added to reach this level. Care is taken to ensure that salt is totally dissolved using the mixing motor.

6. The pH of the electrolyte is adjusted to 8.20 by using $NaOH$ in tablet form.

7. A sample (500 ml) of the electrolyte is taken from the tank for future reference. Also conductivity of electrolyte is benchmarked against a 32.44 grams per litre KCl solution which possesses a conductivity approximating seawater [41,42]. Before each series of experiments, the conductivity meter reading is calibrated against known solutions of KCl at 1, 3, 3.5, 7, 11 and 16 percent by weight [40].

8. After an experiment is completed, a second 500 ml sample of solution is taken to determine any changes in electrolyte consistency.

5.7 Experimental Procedure for Flowing Condition

After electrolyte mixing is accomplished, current-voltage behavior is examined at two different conditions—flowing and stagnant. For all experiments, the power supply is set up for voltage dependence: power supply will provide current necessary to attain the voltage set by user. The pH and temperature probes are placed in the fluid at top of recirculation tank. The conductivity probe is located approximately 20 inches upstream of the test section. The ventilation system is activated for entire experiment. Because stagnant case was found to degrade electrodes faster than flowing condition, the later is first examined. The procedure for flowing condition is as follows:

1. Parajust motor controller is activated. After 30 second ramp time, the centrifugal pump is at operating speed. Flow rate is then adjusted to .5 m/s (1 m/s for the 1"$\times$1" test section) using motor controller in conjunction with diaphragm valve. At least 10 psi head at pump discharge must be obtained to ensure proper lubrication of the impeller housing bearing.

2. Once desired flow rate is reached, chart recorder is activated at rate of 25 mm/min and zero and span are set on all recorder pins. The chart recorder is

used to generate a written history of each experiment. Initial readings of voltage (voltmeter from Hewlett Packard) and current (from ammeter) are recorded directly on chart paper in respective columns. Initial values of temperature, pH, voltage, conductivity, current, pump head, pressure upstream of test section and pressure drop across electrodes are then recorded.

3. Potential across electrodes is then incremented to desired level. Voltage increments of .1 volt are used from 0 to 2.0 volts potential difference. The increment is increased gradually as the potential difference increases from 2 to 5 volts. Above 5 volts potential difference, an increment of 5 volts is used.

4. After any change in potential difference, the power supply is given time to reach steady state. For low voltage runs, this delay time is approximately 20 minutes. For higher voltage runs, the current and voltage stabilized almost instantaneously.

5. Once power stability is attained, voltage, current, conductivity, pressure difference across electrodes, pH and temperature measurements are recorded. Readings for voltage and current are placed directly on chart recorder. Recorder speed is than increased to 1 mm/sec for approximately 15 seconds. This enables clearer recording of pressure variance across electrodes.

6. Steps 3 through 5 are then repeated until entire range of voltage variations for the specific flow rate are complete. Once series is completed, power supply is turned off.

7. Steps 1 through 6 are repeated for flow rates of 2.5 m/s and 5 m/s (5 m/s and 10 m/s for the 1"$\times$1" test section).

5.8 Experimental Procedure for Stagnant Condition

1. Following same procedure as in step 1 of flowing case, flow rate is adjusted to .5 m/s and all initial readings are recorded.

2. Power supply is turned on and set to desired voltage. Power supply is then turned off.

3. Centrifugal pump is shut off. Isolation ball valves located upstream and downstream of test section are closed.

4. Chart recorder is turned on and set to 25 mm/s. An event marking device is used to record all pertinent time dependent readings such as initial current, maximum current and periodic decaying current levels as displayed by the Ammeter. The values of current and voltage corresponding to the event are marked directly on the chart recorder paper.

5. The power supply is turned on and operated until current reading has decayed asymptotically to a stable value. The stable value is usually approached within 10 seconds. However under conditions of extreme gas formation (potential difference greater than 20 volts) a stable value will still be approached, but may not be reached due to movement of microscopic hydrogen bubbles on and off of the electrode surface. The power supply is then deactivated upon realization of the oscillations.

Once the experiment is finished, the synthetic seawater is drained form the system. System is then flushed with tap water and allowed to air dry. All filters are rinsed clean or replaced. Any deposits are removed from strainer. Test section is disassembled and inner surfaces are cleaned.

Chapter 6

EXPERIMENTS OF SEAWATER ELECTROLYSIS

6.1 Introduction

The purpose of this experimental investigation is to determine the effects on ionic conductance of seawater with respect to varying flow rates and electrode materials. Since the production of microbubbles increases the resistance of the seawater by decreasing the volume of electrolyte available to transport electric current, a primary goal of this work is to determine whether the current across the electrodes increases with increasing flow rates. This corresponds to flushing the microbubbles off the electrode surfaces. Flow rates examined were .5, 2.5 and 5 m/s for 1"$\times$2" duct and 1, 5 and 10 m/s for 1"$\times$1" rectangular duct. The importance of activation and diffusion overpotentials at MHD operating currents was examined. Simultaneous evaluation of the performance of different types of electrodes was conducted. Electrolysis was performed using platinum-plated copper, graphite, and Hastelloy-C electrodes. The dimensionally stable anode (DSA), dimensionally stable electrode (DSE) and gas diffusion electrodes were not evaluated due to complexities involved in the test section and electrode design (this will be a subject of future work).

6.2 Conductivity as a Performance Measurement

Since conductivity of seawater is both a function of temperature and salinity, results of the experiments had to be compared against a theoretical conductivity of seawater at said temperature. Because the salinity of synthetic seawater was set at 35%, the fourth degree polynomial developed by Dauphinee and Klein [43,44] could be used for this purpose:

$$R_D = \frac{\sigma_{t,35}}{\sigma_{15,35}} = 0.6765836 + 2.005294 \times 10^{-2} t$$
$$+1.110990 \times 10^{-4} t^2$$
$$-7.26684 \times 10^{-7} t^3$$
$$+1.3587 \times 10^{-9} t^4. \quad (6.1)$$

Here R_D is the ratio of the conductivity of seawater at temperature t and 35% salinity ($\sigma_{t,35}$) to the conductivity of standard seawater at $15°C$ and 35% salinity ($\sigma_{15,35}$). To obtain the conductivity of seawater at 35% and temperature t, Eq. (6.1) must first be used to determine R_D. The conductivity can then be determined by,

$$\sigma_{t,35} = R_D \sigma_{15,35}, \quad (6.2)$$

As can be seen by Table 6.1, this equation predicts the behavior of seawater at 34.325% salinity to within 2% in the range of $0°C$ to $29°C$.

6.3 Stagnant Condition Results with Platinum-Plated Electrodes

Figures 6.1 and 6.2 show current versus time for stagnant case of a 2"×1" test section and 1"×1" test sections, respectively. In all cases the general behavior is identical. Following creation of potential different between electrode plates, the current increases rapidly from zero to its maximum value in under one second. The hydrogen is continuously generated in direct proportion to current density as discussed in section 4.4. Therefore the longer the electrolytic process is sustained, the larger the buildup of hydrogen. The increasing quantities of hydrogen gas displaces the

TABLE 6.1 Comparison of Equation (6.1) Estimations of Conductivity at 34.325 % Salinity with Seawater Conductivity at 34.325 % Salinity

Temperature Degrees Celsius	Thomas et al. [44,45] $\Omega^{-1}cm^{-1}$	Reeburgh [44,46] $\Omega^{-1}cm^{-1}$	Polynomial† $\Omega^{-1}cm^{-1}$
0.0	28.542	28.530	28.542
5.0	32.917	32.870	32.885
10.0	37.432	-	37.440
15.0	42.176	42.162	42.185
20.0	47.077	-	47.099
25.0	52.148	52.138	52.163
29.0	-	56.283	56.308

† where $\sigma_{15°C,34.325\%} \approx 42.185\Omega^{-1}cm^{-1}$ [44]

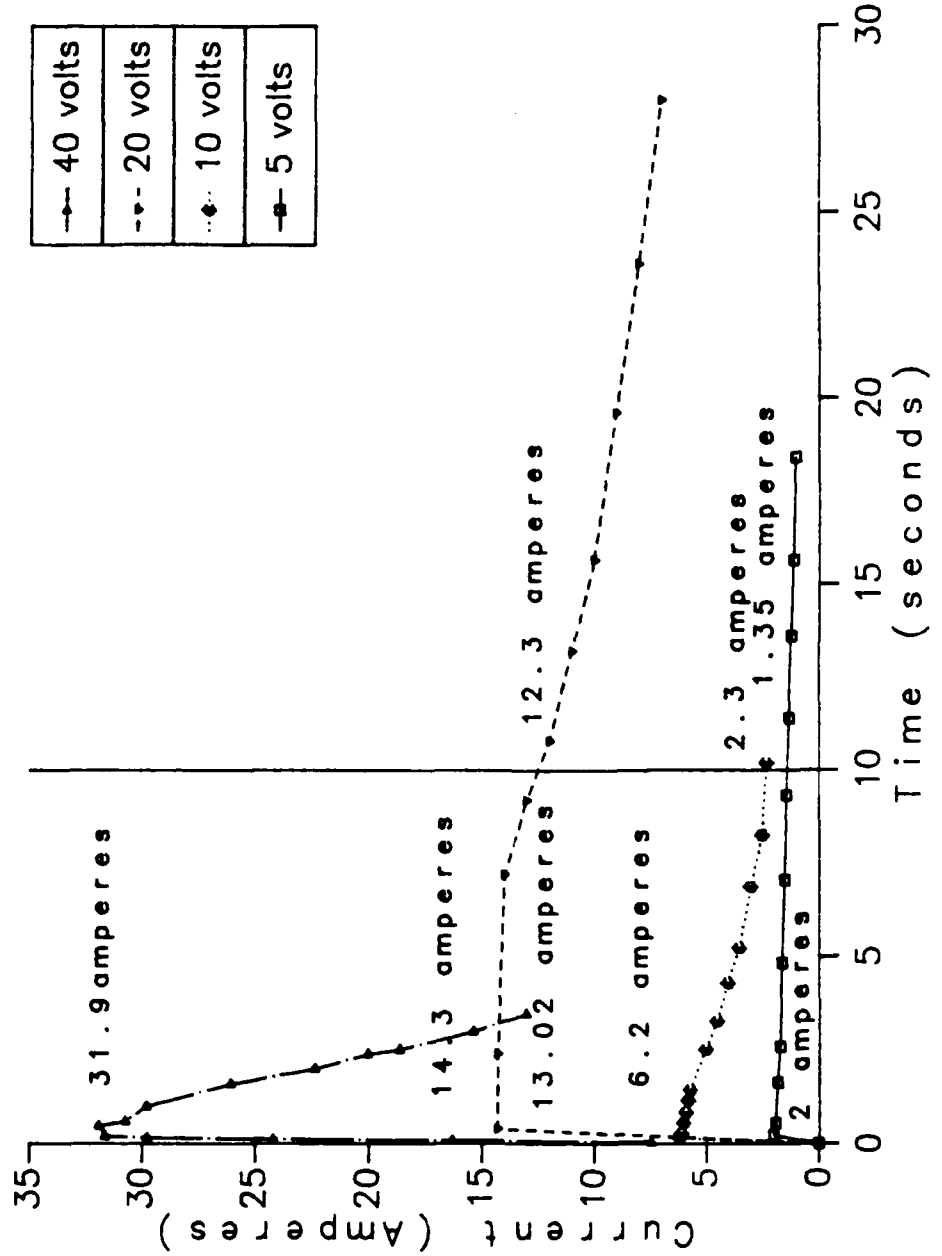

Figure 6.1 Current versus Time for 2"×1" Duct Stagnant Case with Platinum-Plated-Copper Electrodes.
Temperature = 25.3-26.8 °*C*. pH = 8.25-8.27.

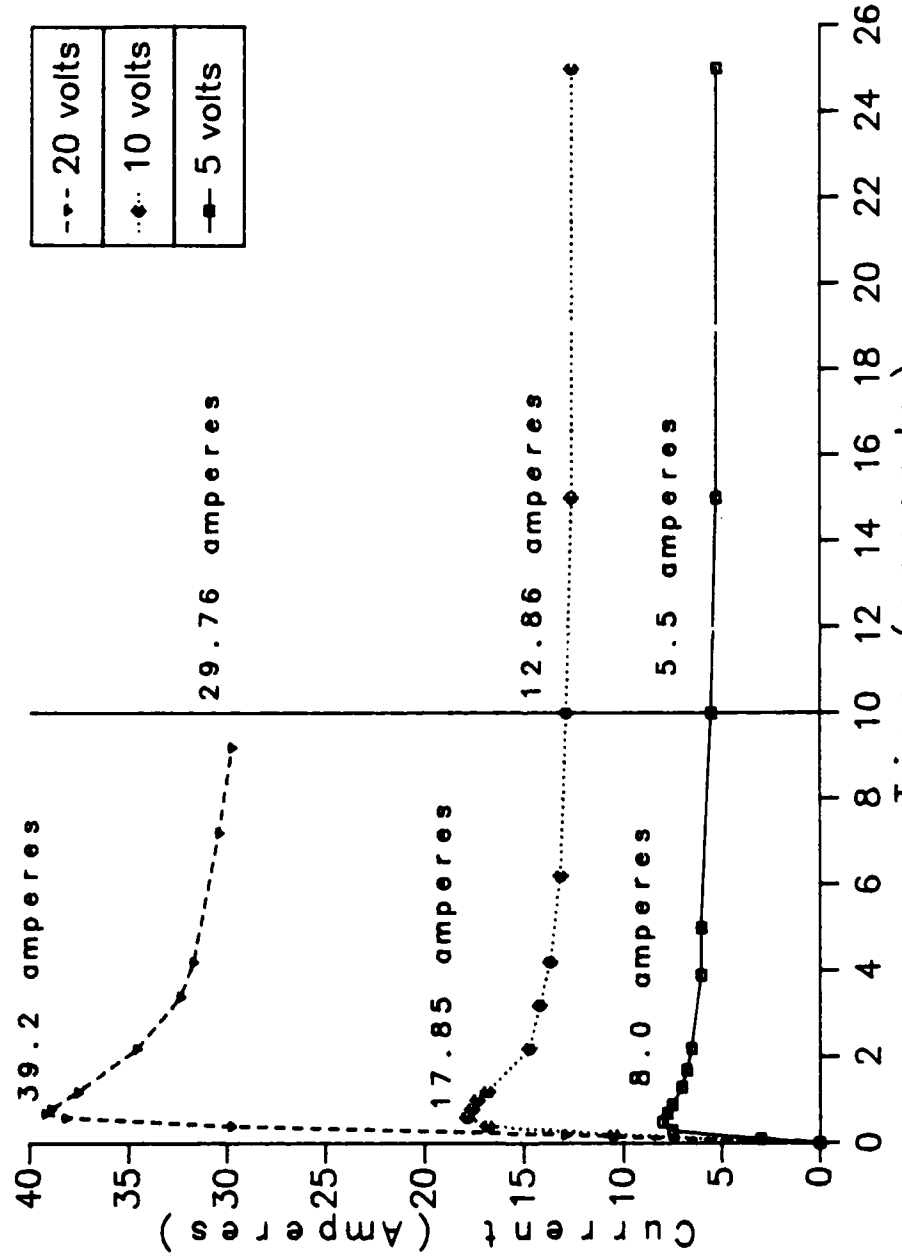

Figure 6.2 Current versus Time for 1"×1" Duct Stagnant Case with Platinum-Plated-Copper Electrodes.
Temperature = 29.3-30.3 °*C*. pH = 8.33-8.34.

electrolyte thereby decreasing the volume of electrolyte available for current transport. This initially results in a drastic decay in current from its maximum value. As time progresses, a steady-state develops between hydrogen production and hydrogen removal by diffusion upstream or downstream of the conducting region. As this occurs, the current between the electrode plates asymptotically approaches an equilibrium value.

Figure 6.3 shows production of hydrogen gas with initial flow of electricity. Here the electrodes have just been energized with a 5 volt potential difference. As expected, the "Alka-seltzer" style hydrogen gas evolution at the cathode occurs instantaneously with flow of electric current.

Figure 6.4 illustrates the migration of hydrogen gas away the from conducting region under equilibrium condition. Here the current has been flowing between the electrode plates for approximately one minute. Some of the H_2 bubbles accumulated at the top of the channel have diffused out of the conducting region. Diffused H_2 gas is that at the far right and left of Fig. 6.4.

As can be seen in Fig. 6.2, the 1"×1" test section under stagnant conditions exhibits the same behavior as the 2"×1" duct. The only significant difference is the current was higher in this test section due to the decrease in gap distance (39.2 A at 20 Volts versus 14.3 A for the 2"×1" test section). The stagnant cases simply illustrate the very significant impact of hydrogen-bubble formation on conductance of the solution.

6.4 2"×1" Duct Flowing Condition Results with Platinum-Plated Electrodes

Figures 6.5 and 6.6 present the results of current versus voltage for the 2"×1" test section with platinum-plated copper electrodes. After overcoming an initial

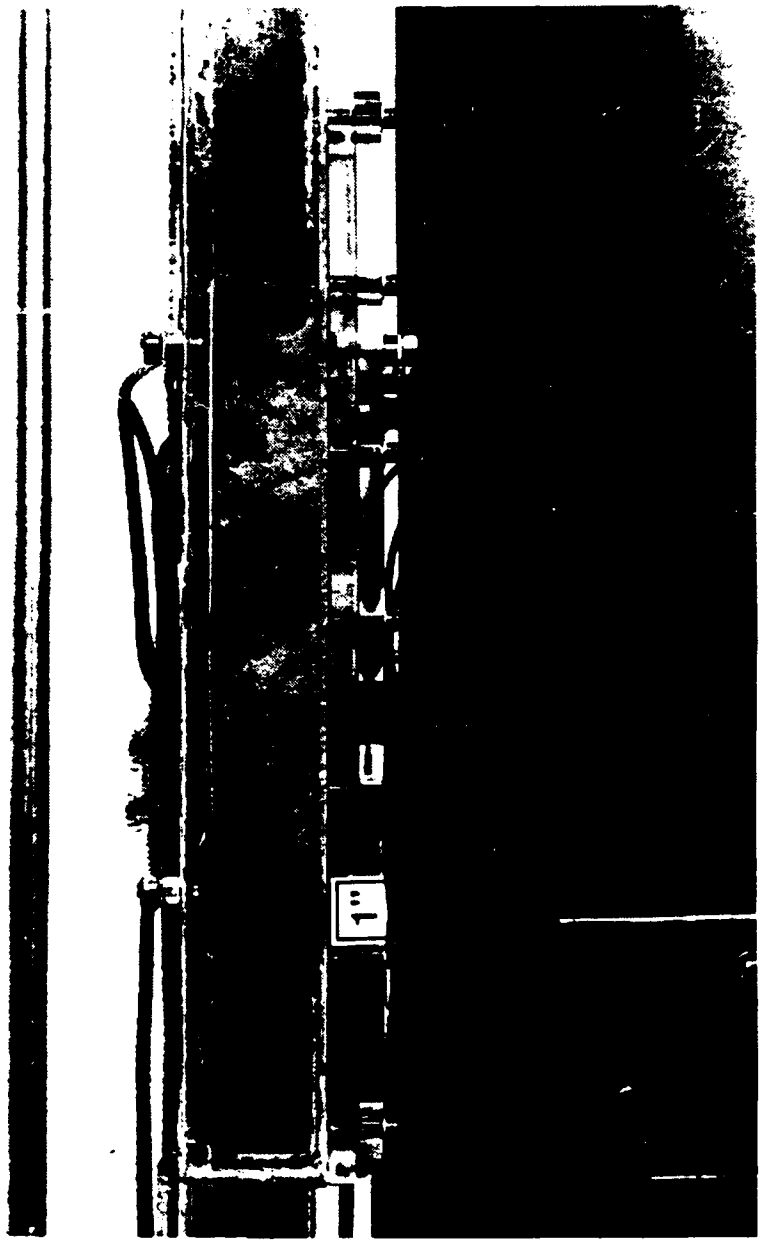

Figure 6.3 Initial Production of Hydrogen Gas.

Figure 6.4 Production of Hydrogen Gas at Equalibrium.

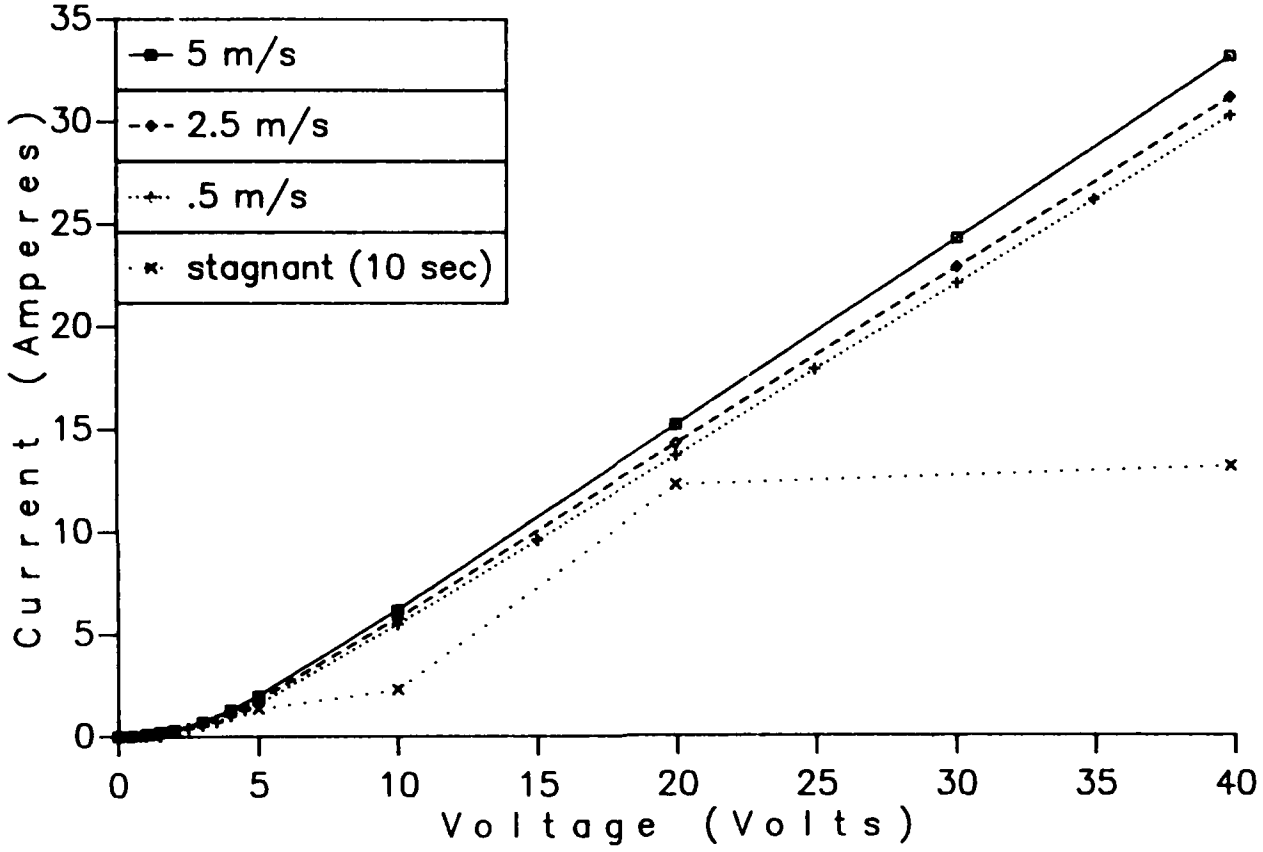

Figure 6.5 Current versus Voltage for 2"×1" Duct with Platinum-Plated-Copper Electrodes: Cathode on Top.
Temperature = 20.8-26.9 °C. pH = 8.21-8.26.

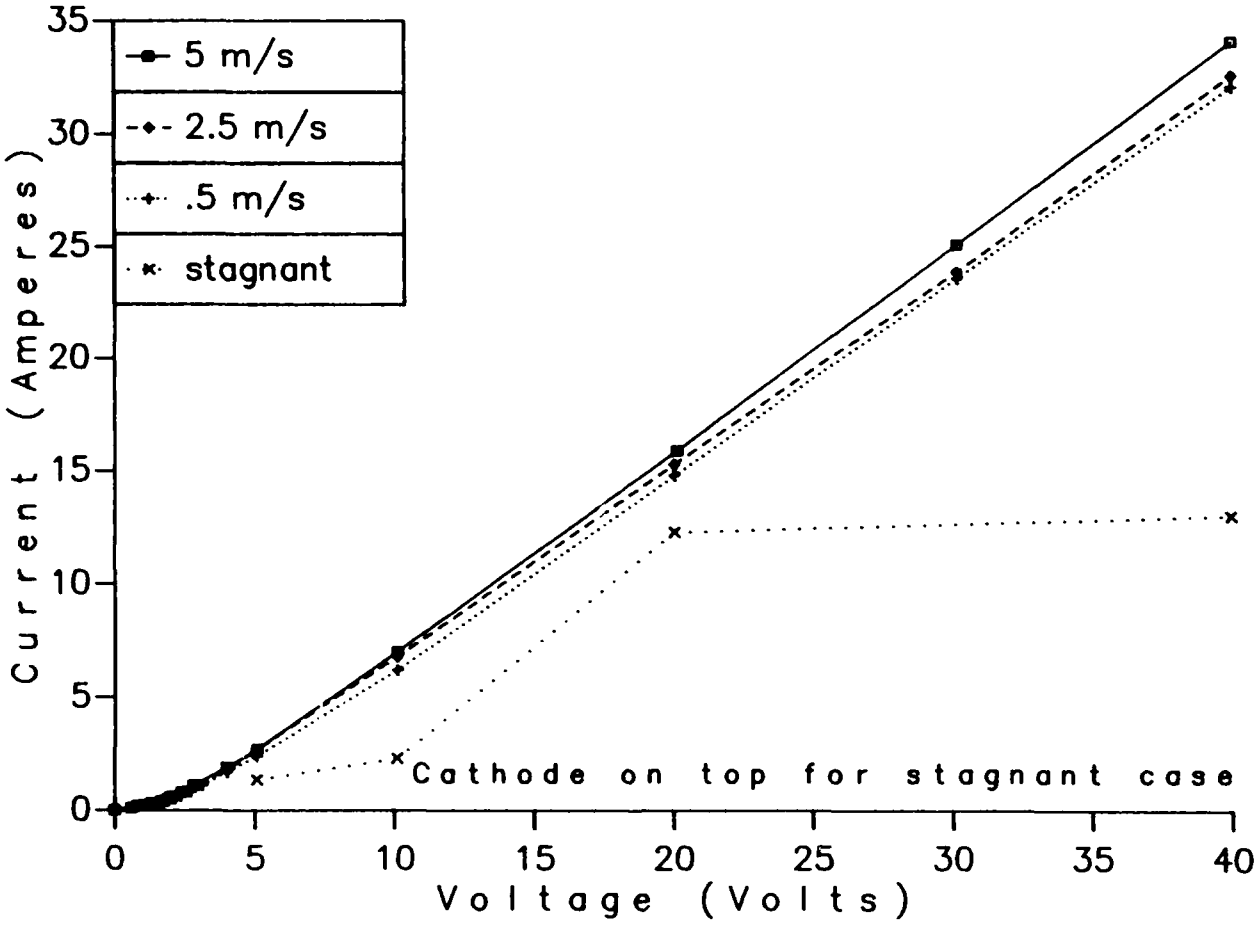

Figure 6.6 Current versus Voltage for 2"×1" Duct with Platinum-Plated-Copper Electrodes: Anode on Top.
Temperature = 25.5-29.1 °C. pH = 8.27-8.30.

activation overpotential, current increases linearly with increasing potential difference between electrodes. This behavior was apparent in all electrode configurations studied. Ohmic losses are primarily a linear function whereas typically dominating overpotentials (such as activation and diffusion) behave logarithmically. This tends to suggest that the most significant cause of potential difference in the presence of current densities above .03 $A \cdot cm^{-2}$ is Ohmic loss.

At any set potential difference, the current was found to increase with an increase in flow rate. The two parameters contributing to this effect are temperature increases and changes in H_2 gas bubble removal rates. During all experiments, the cases were studied by first completing .5, then 2.5 and finally 5 m/s scenarios (1, 5 and 10 m/s, respectively, for 1"×1" duct). Thus the solution temperature increased due to Ohmic heating with each flow rate evaluated. Since the conductivity of a solution increases with increasing temperature, this attributed significantly to the increase in current with increasing flow rate observed at a constant voltage.

The second factor that would contribute to the improved conductance is the flushing of the gaseous products downstream of the test section as discussed in section 4.3. This parameter should become more significant at higher current densities since gas production is in direct proportion to current densities.

Fig. 6.5 presents the current versus voltage results of the 2"×1" test section with the cathode located above the anode. In this orientation, the hydrogen is produced at the top of the duct. Since hydrogen is considerably less dense than seawater, it remains near the cathode surface until being "flushed" downstream. The flow rate in the test section is fully developed. Therefore it is hyperbolic in shape with maximum channel velocity in the center of the duct and zero velocity at the duct walls due to viscous effects (assuming "no slip" conditions). The end

result is that the hydrogen is carried downstream by fluid traveling at a much lower velocity than the mean.

Fig. 6.6 presents current versus voltage results when cathode and anode are reversed. By locating the cathode at the bottom of the channel, the hydrogen rises into the mainstream of the fluid, and is thereby "flushed" much faster. Figure 6.7 illustrates "flushing" of the bubbles in the MHD channel. At 40 volts in the presents of 5 m/s flow rate, a current of 34 A was obtained (compared to 33 A with the cathode on top). Thus the rise in conductance based on electrode orientation is significant.

Figures 6.8 and 6.9 show the overvoltage as a function of current density for the 2"$\times$1" test section with platinum-plated copper electrodes. It should be pointed out that the overvoltage is determined by $V - IR$, where IR is Ohmic loss. To determine an empirical relation for R, the chemical consistencies of the solution were assumed not to significantly change during the experiment. Also, the empirical expression for conductivity was assumed to accurately represent the behavior of the solution. Validity of these assumptions was obtained by benchmarking the conductivity of the synthetic seawater solution with the conductivity of standard seawater before and after the experiment. However, using Eq. (2.2) for determining R does not take into account current that will travel in electric fringing fields at edges of the two electrode plates; therefore the value for R empirically determined will overestimate the actual value. The effect of the fringing fields was found to be more noticeable with increasing current density (above .03 $A \cdot cm^2$).

Fig. 6.8 shows results for 2"$\times$1" rectangular duct with the anode located below the cathode. In this configuration, the overpotential required to pass current was on the order of 2.6 volts at .0225 A and flow rates of 2.5 m/s and 5 m/s. The

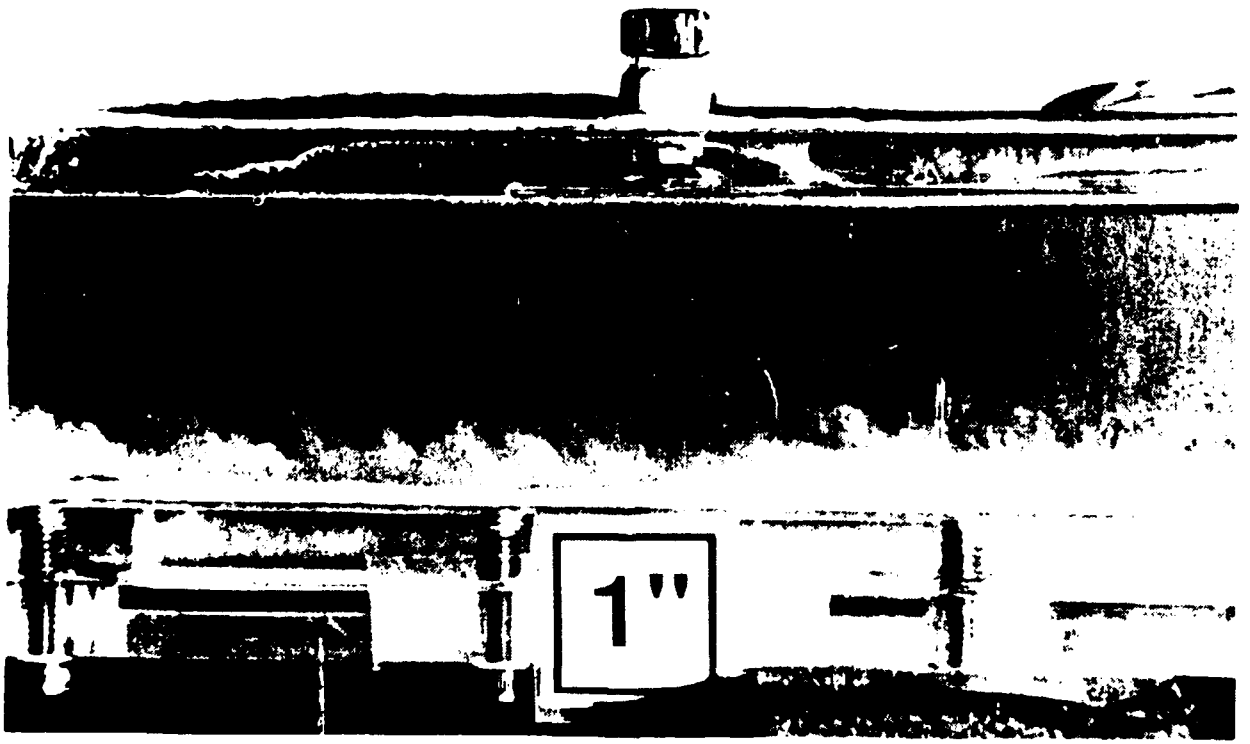

Figure 6.7 "Flushing" of Hydrogen Bubbles under Flowing Conditions.

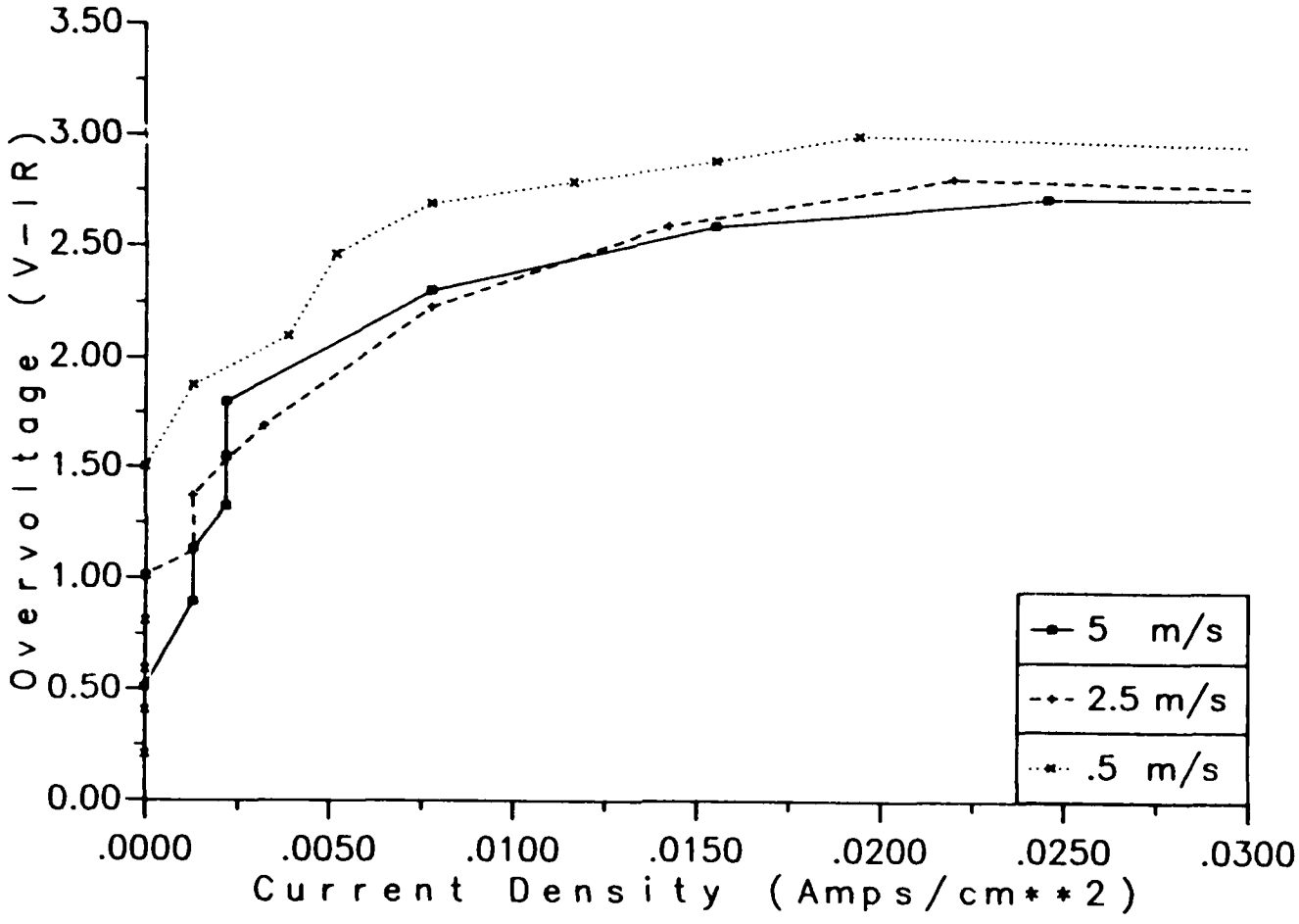

Figure 6.8 Overvoltage versus Current Density for 2"×1" Duct with Platinum-Plated-Copper Electrodes: Cathode on Top.
Temperature = 20.8-26.9 °*C*. pH = 8.21-8.26.

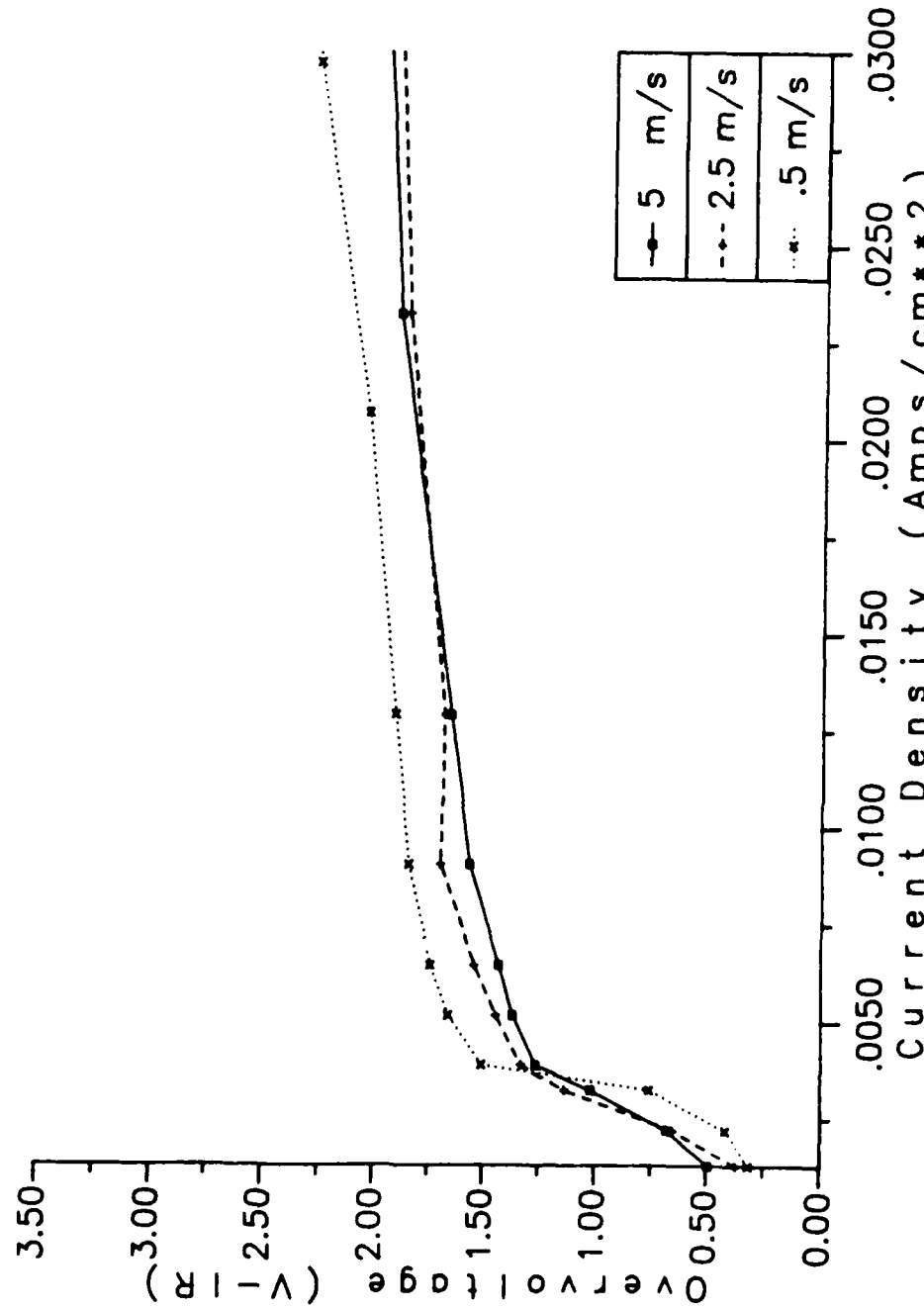

Figure 6.9 Overvoltage versus Current Density for 2" ×1" Duct with Platinum-Plated-Copper Electrodes: Anode on top.

Temperature = 25.5-29.1 °C. pH = 8.27-8.31.

overvoltage for the .5 m/s case was significantly higher (approximately 2.9 volts). The variance between the .5 m/s scenario overvoltage and the lower overvoltage in the higher flow rate scenarios clearly establishes dependence of overvoltage on flow rate.

The diffusion overvoltage is probably the parameter being affected. This overvoltage is the result of decreasing reactant concentrations near the electrode surface while increasing product concentrations due to limiting mass transfer by diffusion. The region of decreased reactant concentration is known as the double layer [33]. Operation at higher flow rates decreased the voltage drop significantly by decreasing the the thickness of the double layer and thereby increasing the diffusion rate near the electrode surface.

Fig. 6.9 illustrates similar results for the platinum-plated copper with anode and cathode reversed. By comparing Fig. 6.8 and 6.9 another interesting behavior is noted. The orientation with the cathode at the bottom attains a consistantly lower overpotential at low current densities (2.0-2.7 volts versus 2.7-3.0 volts for opposite orientation). This improvement is probably due to lower diffusion overpotential due to better diffusion of reactants to electrode surface. With cathode on top, the diffusion process is hindered by increased difficulty in removal of hydrogen gas produced at the electrode surface.

6.5 1"×1" Duct Flowing Condition Results with Platinum-Plated Electrodes

Figure 6.10 presents current versus voltage results for the 1"×1" rectangular duct. As with the larger test section, an increase in flow rate resulted in an increase in current. Of interest in these cases is the increased magnitude in current as compared with the 2"×1" rectangular duct. Since the electrode gap distance l

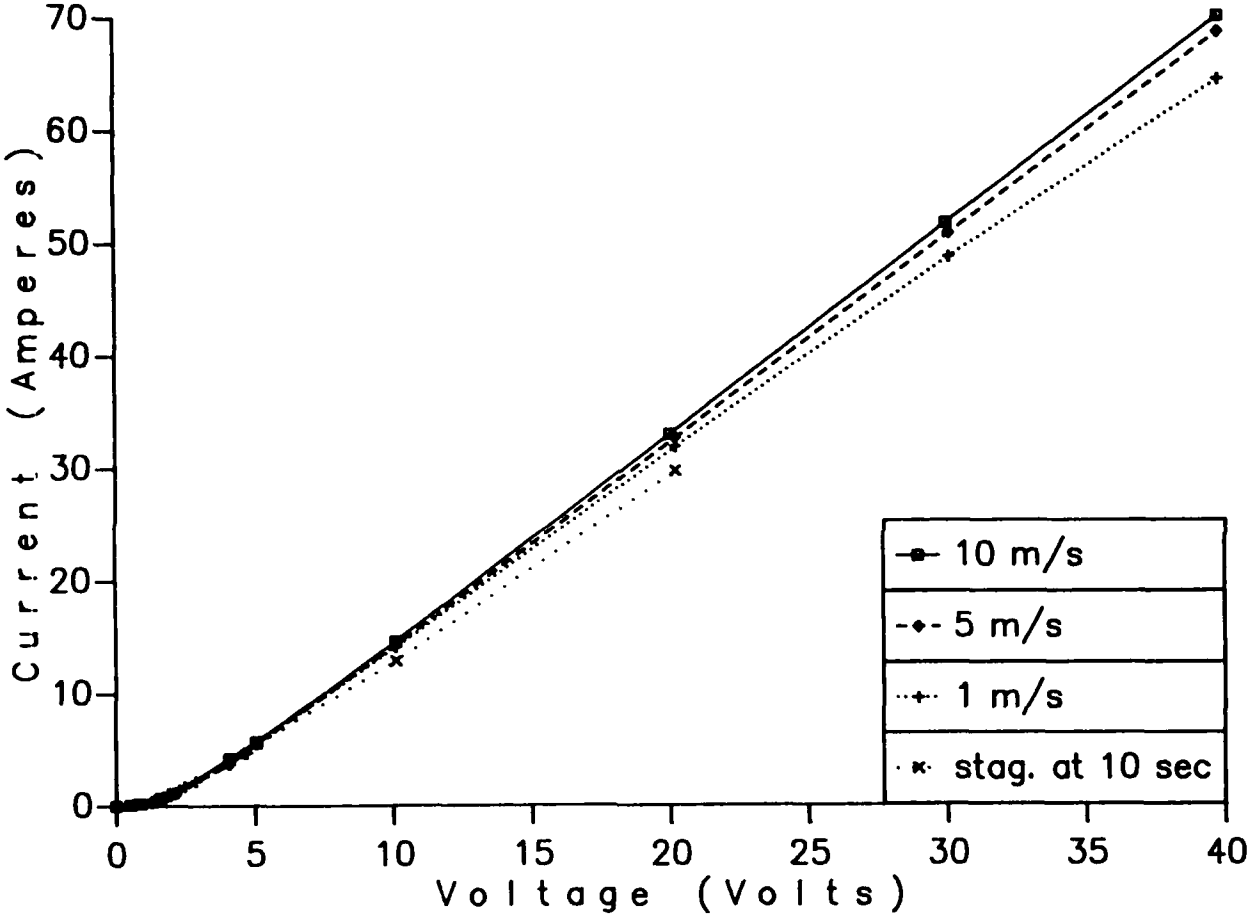

Figure 6.10 Current versus Voltage for 1"×1" Duct with Platinum-Plated-Copper Electrodes: Anode on Top.
Temperature = 27.9-30.9 °*C*. pH = 8.29-8.34.

has been decreased by a factor of two, the effective resistance should also decrease proportionally. This is evident in the much higher current (70 A at 40 volts versus about 34 A at 40 volts for the 2"×1" test section).

Since the volume of the electrolyte is much less as compared to the larger test section, the 1"×1" test section is more adversely effected by gas bubble displacement of conducting electrolyte. This is illustrated by the larger increase in current densities with increasing flow rates. At 1 m/s and 40 volts potential difference, 64.4 A were conducted; at 5 m/s, 68.4 A were passed; and at 10 m/s, 70 A were passed. This is compared against the 2"×1" test section with cathode on bottom. The current generated was 32.1 A, 32.6 A and 34.0 A at .5, 2.5 and 5 m/s, respectively.

Figure 6.11 shows the overvoltage as a function of current density for the 1"×1" test section using platinum-plated-copper electrodes. The same trend of decreasing overvoltage with increasing flow rates was observed. However, the overvoltage for this scenario was much lower than that of the 2"×1" test section cases, (1.75 volts at .06 A). The decrease in overvoltage is probably due to a decrease in the double layer thickness near the electrode surface. This decrease is caused by the much higher channel velocities present in the 2"×1" duct when operating at the same volumetric flow rates as the 2"×1" duct.

6.6 2"×1" Flowing Condition Results with Graphite and Hastelloy-C Electrodes

As illustrated by Figures 6.12 (anode on top) and 6.13 (cathode on top) the current versus voltage behavior of the 2"×1" test section with Hastelloy-C as cathode and graphite as anode is very similar to that observed with the platinum-plated copper. Above .03 $A \cdot cm^2$, current increases linearly with voltage. Increase in flow rate resulted in increase in conductance. It should be noted that the discontinuity

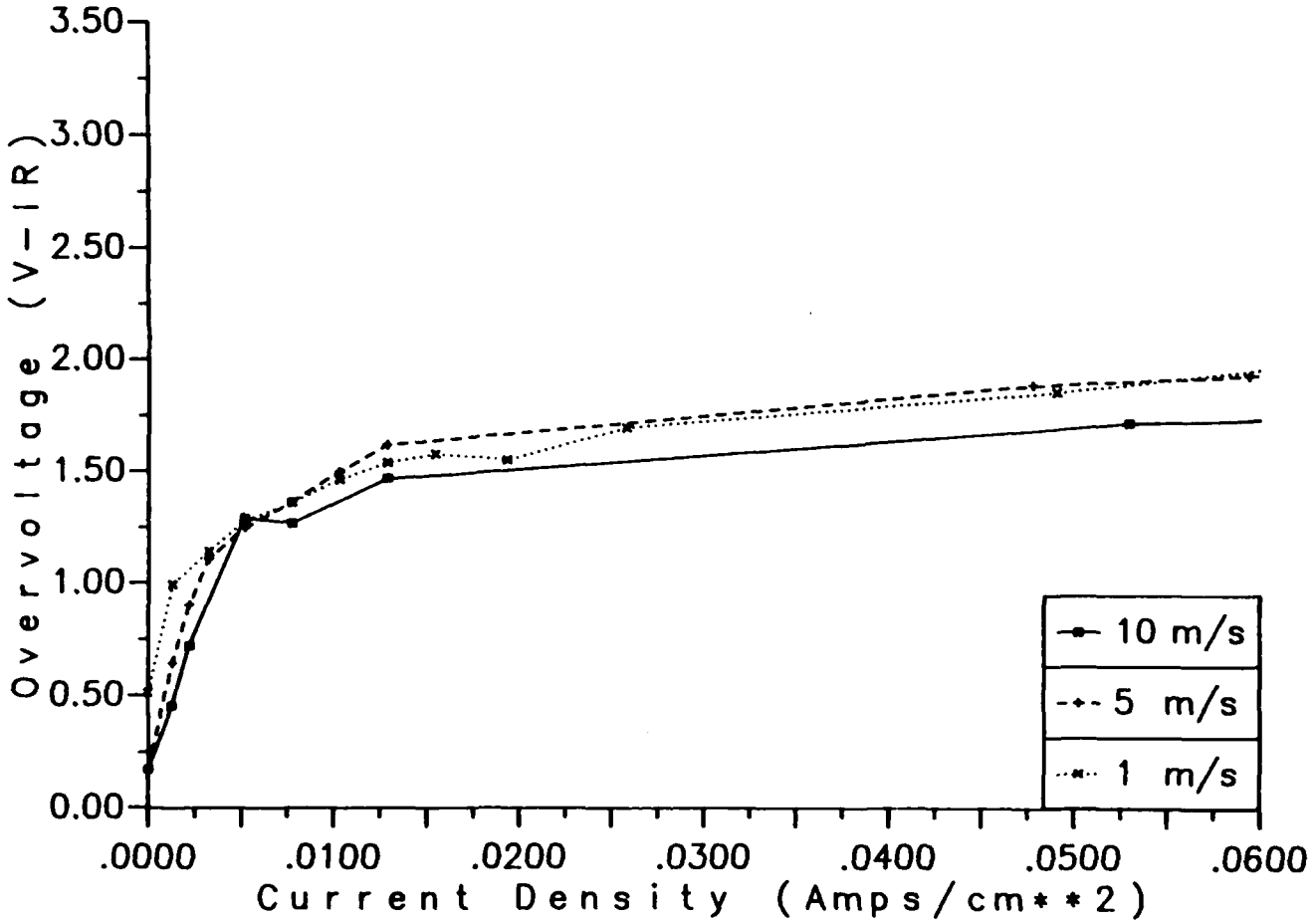

Figure 6.11 Overvoltage versus Current Density for 1"×1" Duct with Platinum-Plated-Copper Electrodes:
Anode on Top.
Temperature = 27.9-30.9 °*C*. pH = 8.29-8.34.

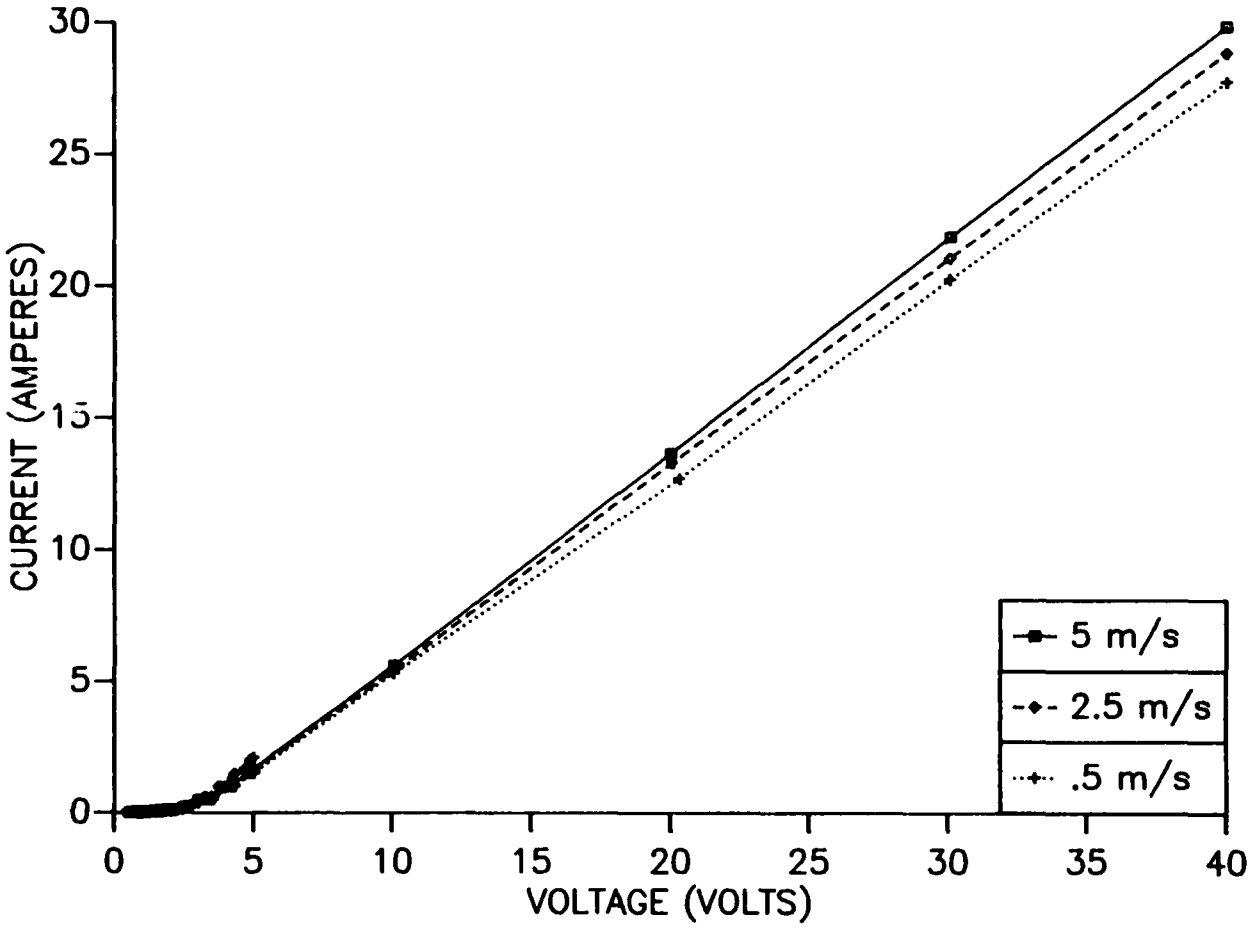

Figure 6.12 Current versus Voltage for 2"×1" Duct with Hastelloy-C Cathode and Graphite Anode: Anode on Top.
Temperature Not Recorded. pH = 8.33-8.41.

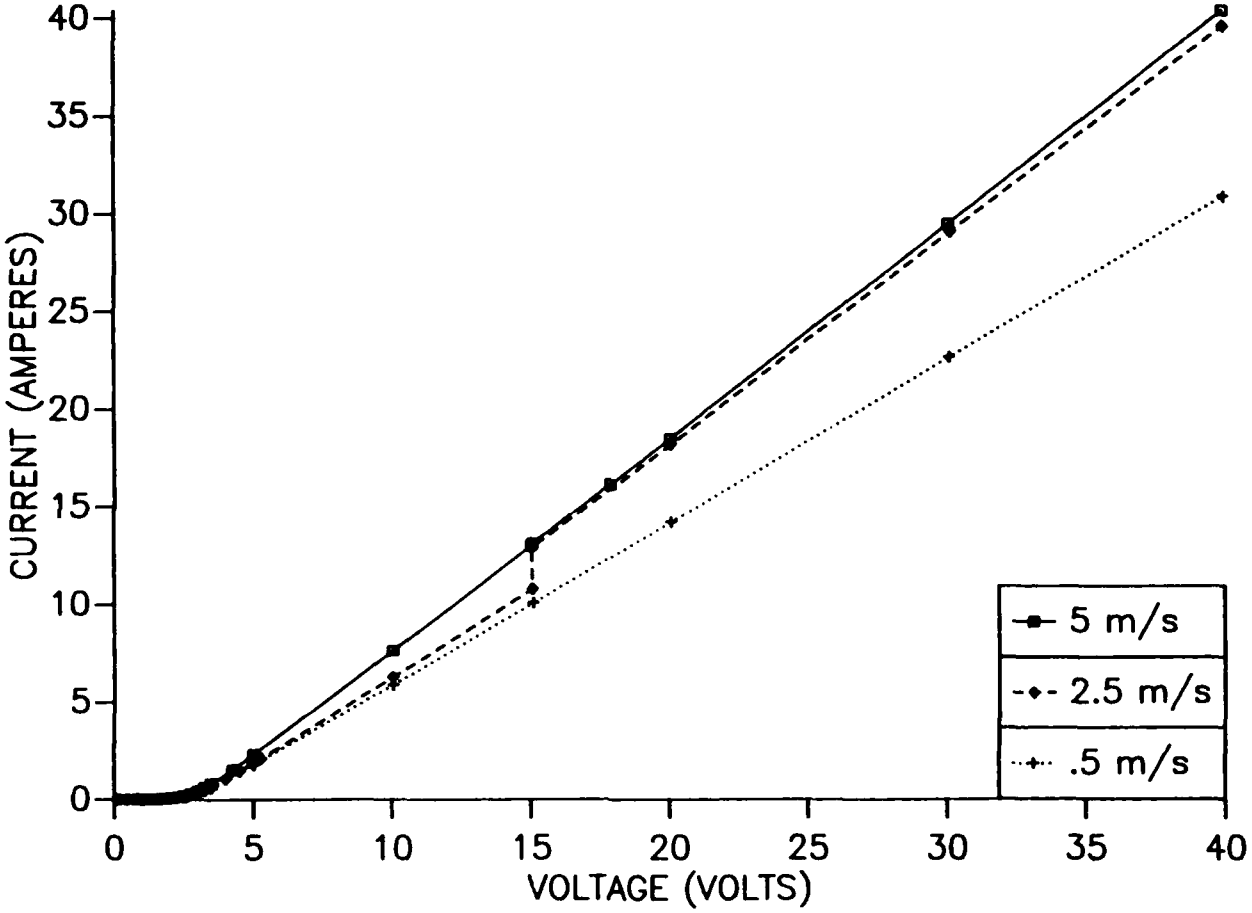

Figure 6.13 Current versus Voltage for 2"×1" Duct with Hastelloy-C Cathode and Graphite Anode: Cathode on Top.
Temperature = 21.7 to 37.5 °*C*. pH = 8.32-8.42.

in Fig. 6.13 at 15 volts is due to the change of experimental condition—the electrolyte temperature changed by approximately $10.1°C$ for the 2.5 m/s case.

Figure 6.14 (anode on top) and 6.15 (cathode on top) shows overvoltage versus current density below .03 $A \cdot cm^2$. In contrast to the platinum case, variance in overvoltage with increasing flow rates was minimal. This suggests that the dominating overpotential is that of activation and not diffusion. An overpotential of ~2.7 volts was required before passage of significant amounts of current was enabled.

Figure 6.16 presents the current versus voltage performance with Hastelloy-C as anode and graphite as cathode. Again the discontinuities at 20 volts are due to the change of experimental condition incurred because of fluctuations in electrolyte temperature ($10.2°C$ increase for .5 m/s case and $7.1°C$ increase for 2.5 m/s case). Figure 6.17 displays the overvoltage versus low current density relationship. As with the opposite configuration, the overvoltage required before passage of current does not appear to fluctuate significantly with variations in flow rate. However, this overvoltage (~2.4 volts) is significantly lower then that incurred when Hastelloy-C functions as a cathode.

6.7 Platinum-Plated Electrode Durability Performance

The platinum-plated-copper electrode did not function well as an anode. Although the platinum seemed unaffected by electrolysis, extensive separation of the platinum-copper interface was observed. The copper thus exposed was severely attacked; pits up to 30 mils in depth were observed on the 1"×1" test section anode surface. Fig. 6.18 illustrates degradation of platinum-plated-copper anode (bottom) and cathode (top). Since the main biproduct found in the electrolyte was copper-oxide and copper-hydroxide (based on x-ray diffraction), oxygen ions

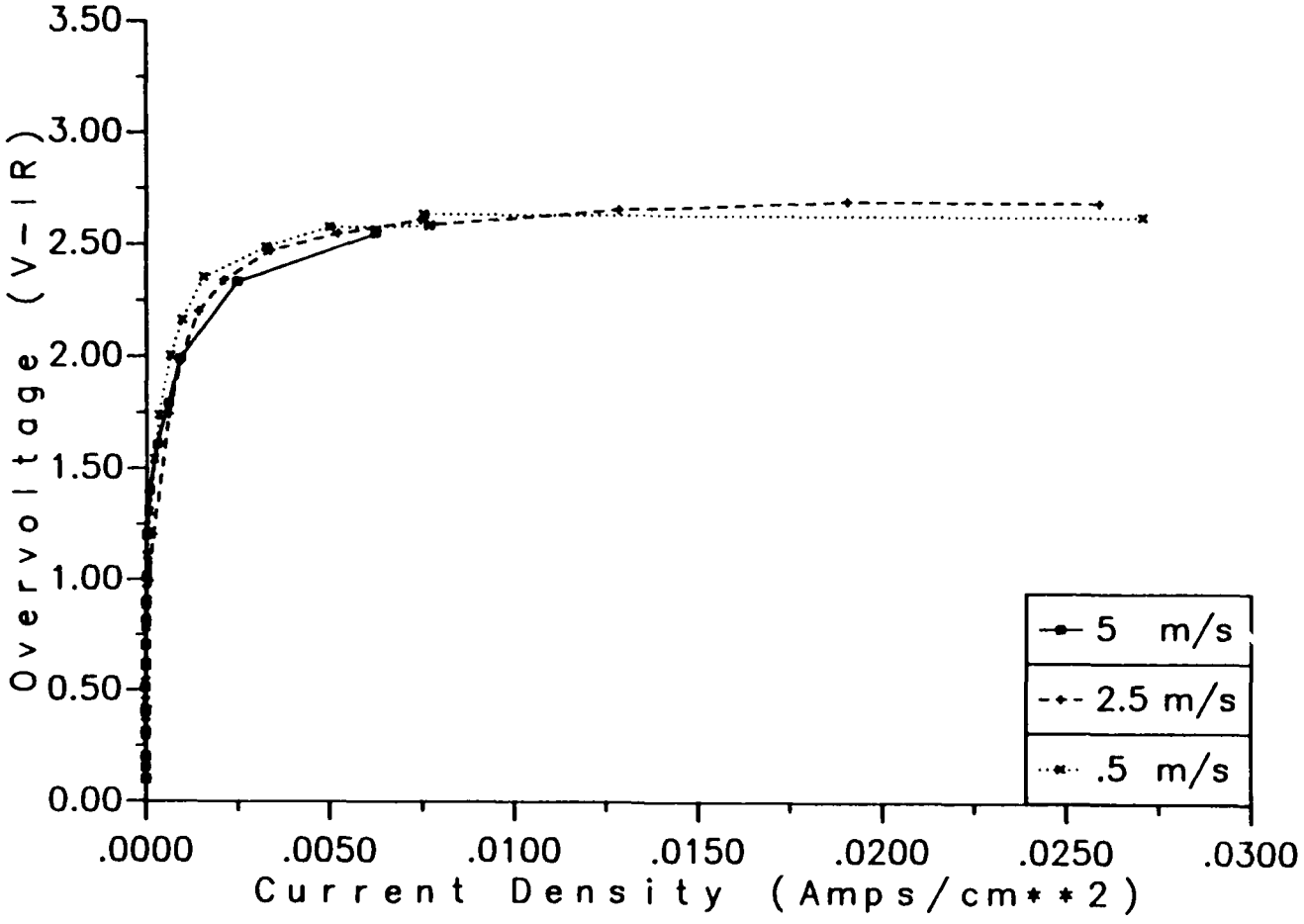

Figure 6.14 Overvoltage versus Current Density for 2"×1" Duct with Hastelloy-C Cathode and Graphite Anode: Anode on Top.
Temperature = 29.8 to 38.1 °*C*. pH = 8.32-8.42.

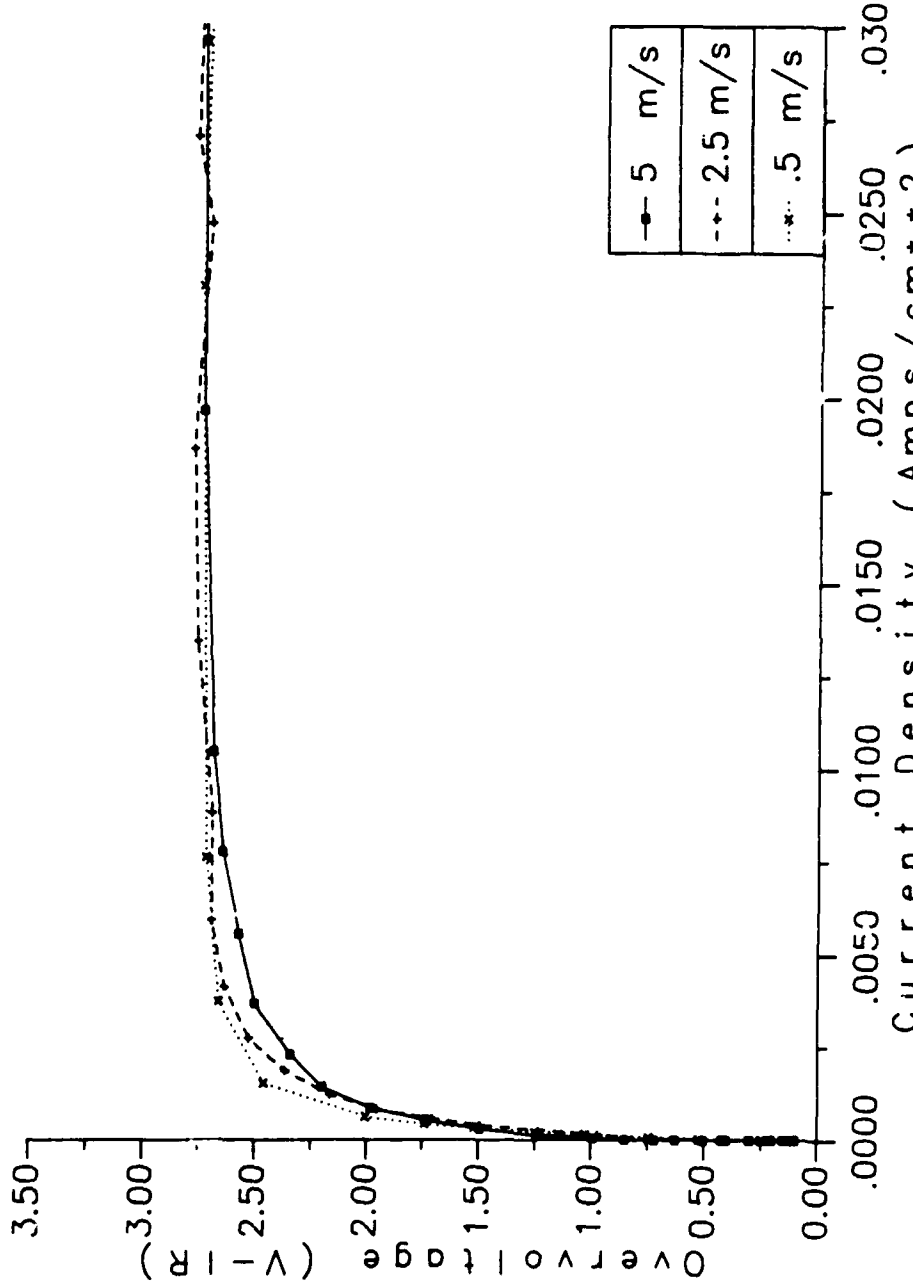

Figure 6.15 Overvoltage versus Current Density for 2"×1" Duct with Hastelloy-C Cathode and Graphite Anode: Cathode on Top.

Temperature = 21.7 to 37.5 °C. pH = 8.32-8.42.

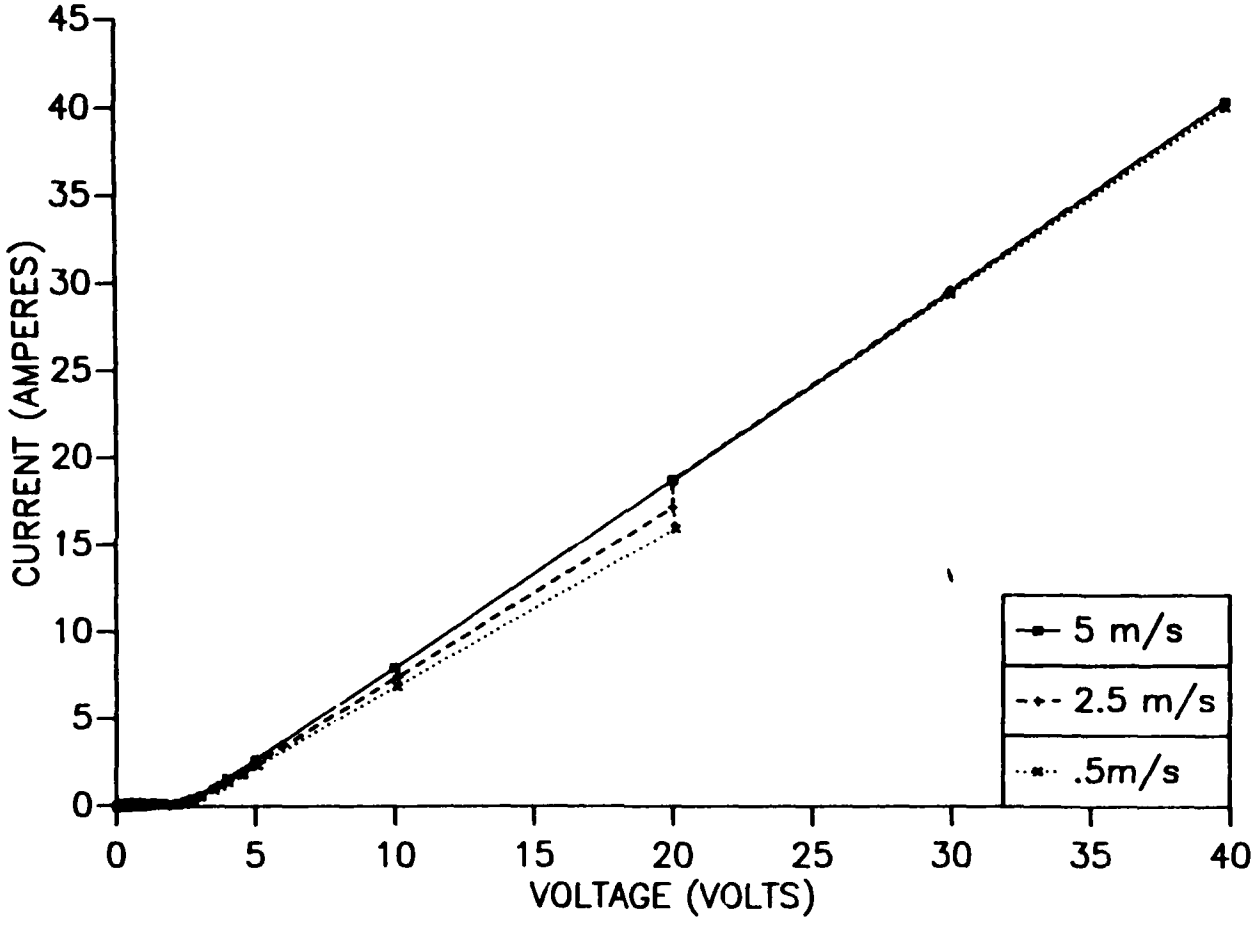

Figure 6.16 Current versus Voltage for 2"×1" Duct with Hastelloy-C Anode and Graphite Cathode: Anode on Top.
Temperature = 23.4 to 38.0 °C. pH = 8.30-8.40.

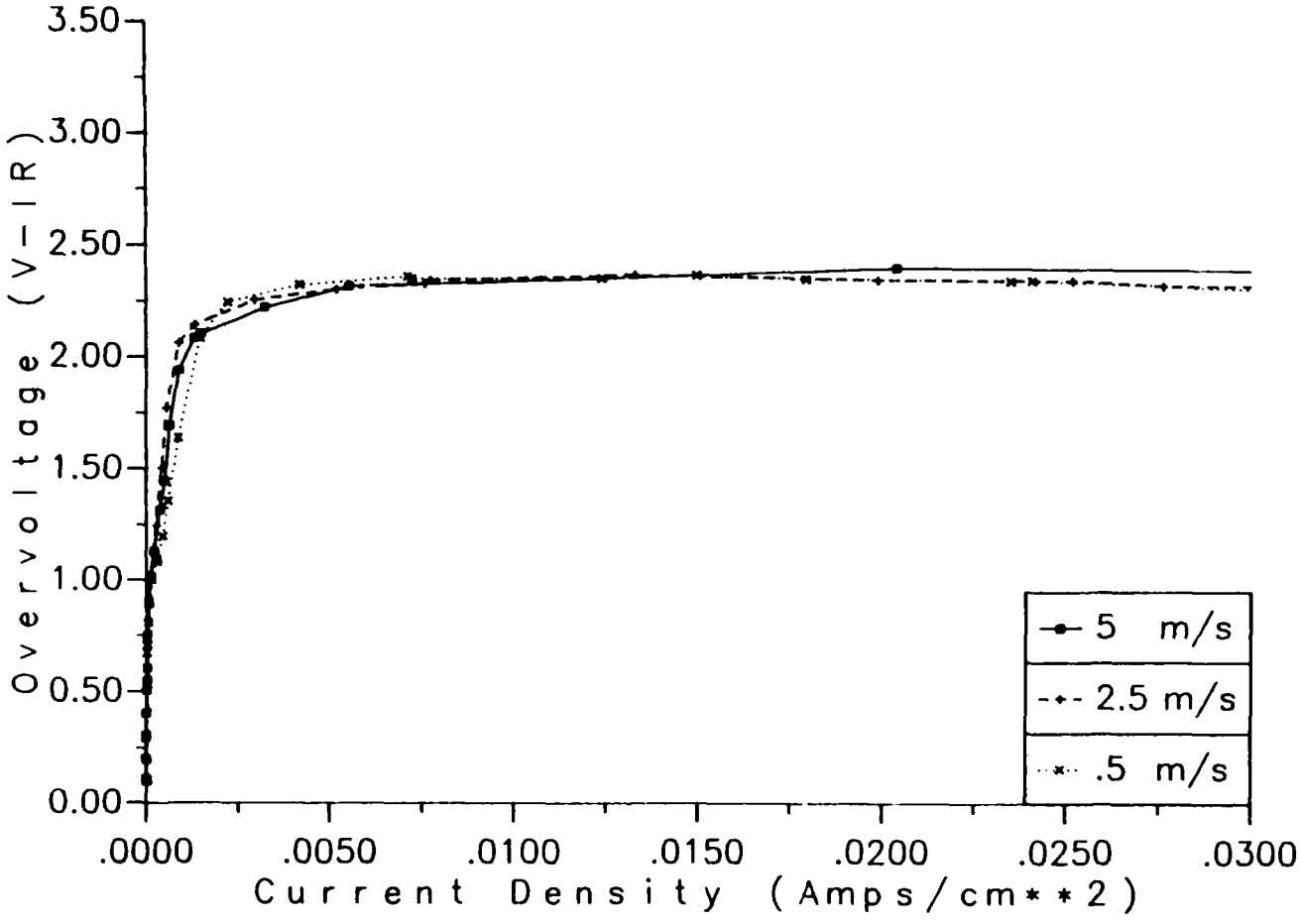

Figure 6.17 Overvoltage versus Current Density for 2"×1" Duct with Hastelloy-C Anode and Graphite Cathode: Anode on Top.
Temperature = 23.4 to 38.0 °*C*. pH = 8.30-8.40.

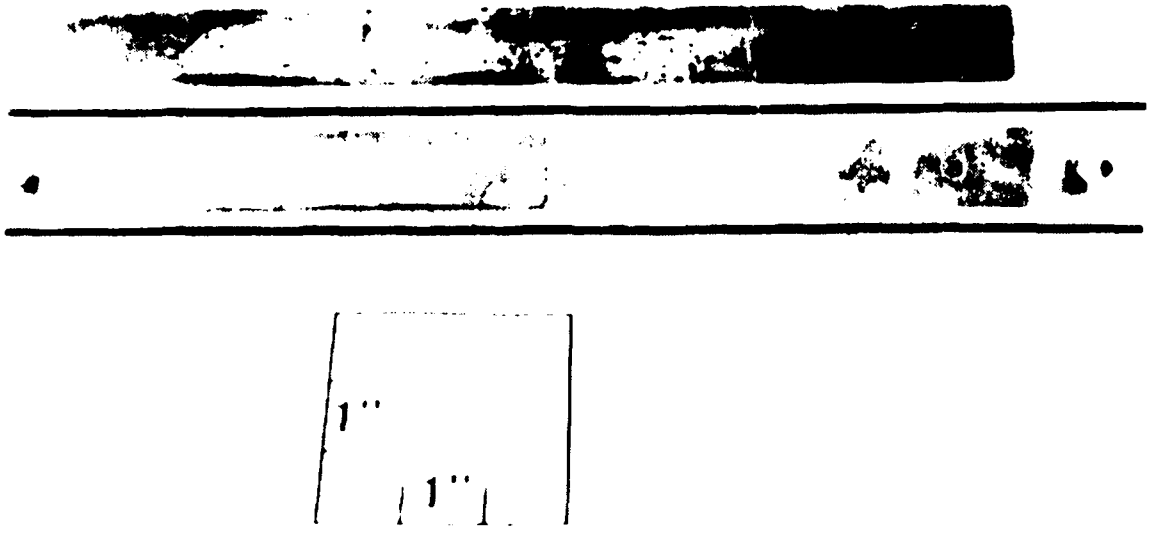

Figure 6.18 Degradation of Platinum-Plated-Copper Anode (Top) and Cathode (Bottom).

evolving at the boundary probably reacted with copper thus erroding the electrode. Underlying copper was unaffected by electrolysis where platinum did not peel.

Platinum peeling was especially noticable at the edges of the electrode, the electrode center and mounting bolts. Degradation at electrode leading and trailing edges can be attributed to significantly higher current densities due to the high electric field at the sharp corners. Since the electrode was plated in two dips, an overlap of platings occurred in the center of the electrode; the first half of the electrode length was plated and then the remainder was plated. The plating did not hold up well where overlapping occurred: The second platinum layer did not stay attached to the first platinum layer. Finally, areas surrounding the mounting bolts peeled extensively. However, the silver solder used to connect the copper bolts to the plate appeared to withstand corrosion.

In the absense of flow, evolution of chlorine gas was visible at the anode. Oxygen gas evolution was not observed. The electrodes used with a 2" gap distance were not corroded as badly as those with only a 1" gap. This may be attributed to a thicker platinum plating on and a lower current density through the former.

The platinum-plated-copper electrode functioned much better as a cathode. Numerous pin head size holes were noted where platinum had worn through. However, exposed copper surfaces were not significantly eroded. As discussed in section 6.3, extensive hydrogen gas formation was observed. Again, some corrosion was noted at the cathode center where the platinum platings overlapped. At the cathode surface during stagnant case experiments, a white precipitate was formed at the boundary of the hydrogen gas bubbles. This product would then dissolve back into the solution. Following the experiment, the solution at the electrodes was filtered and the resulting residue was analyzed by x-ray diffraction. Relatively high

concentrations of $SrCO_3$ were detected by phase identification. Since $SrCO_3$ is a white substance of crystalline form, it may have been the substance observed being evolved.

6.8 Hastelloy-C and Graphite Electrode Durability Performance

The Hastelloy-C electrode performed better than the platinum-plated copper. Instead of pitting, Hastelloy-C electrode was uniformally eroded along the grain of the metal. The plate thickness was decreased by a nominal 7.5± 1.5 mils. Slightly more noticable wear occurred at the leading and trailing edges of the electrode. As with platinum-plated-copper, this can be attributed to higher current density at the edges due to fringing electric field effects. Electrode surfaces scorched from welding withstood corrosive effects much better than the normal surface. This suggests that metallurgical processes such as annealing may improve the resistance of Hastelloy-C to corrosion.

The electrolyte became contaminated by yellow colored flakes following Hastelloy-C anode errosion. These flakes would then dissolve into solution giving the electrolyte a distinct yellow appearance. Since iron was one of the contaminates found following x-ray diffraction analysis of filtered seawater, the yellow product may be some form of iron, such as iron-oxide.

The graphite electrode functioned extremely well as both cathode and anode. The machined graphite surface was polished before experimentation. This decreased the electrode thickness by 1 mil. Even after extensive operation, no further decrease was observed. Corrosion in the form of pitting or eroding was not observed even after several hours of continuous operation. However, the brittle nature of graphite may be a serious drawback when used as an electrode for seawater MHD propulsion.

Qualitative analysis of the seawater following experiments with graphite and Hastelloy-C yielded some fairly interesting results. When graphite was used as an anode and Hastelloy-C as cathode under flowing conditions, a $SrCO_3$ residue was detected from the sample taken from the recirculation tank. However, when a sample from the test section following stagnant experiments was analysed, $CaCO_3$ was discovered. When graphite was used as the cathode and Hastelloy-C as the anode, $SrCO_3$ was again detected in the tank. However, following stagnant case runs, a sample taken at the electrodes yielded no detectable phases other than an amorphous residue.

6.9 Conclusions

From initial experiments, the MHD thruster performance can be optimized to within 98% of theoretical conductance. This can be accomplished by designing the device to operate in the constraints that significantly high current and flow rate are maintained to minimize influences of overvoltage and gas production. However, current must not be so high that degradation of electrodes due to corrosion/erosion occurs.

Of the materials tested, graphite seems to offer the best performance. However, this is offset by its poor performance under shear stress. Hastelloy-C would be the next contender if it could be made more durable. A dimensionally stable electrode such as manganese-oxide plated titanium is probably the most promising. If a gas permeable electrode can be developed that withstands the extreme corrosive effects of seawater, the MHD thruster may attain even better conductance related performance at various flow rates due to the absence of gas evolution on the electrolyte-electrode surface.

As discussed in section 4.7, the most promising electrode material based on past research is of dimensionally stable design. It prefers an oxygen reaction at the anode while being resistant to corrosive effects of seawater. Experimentation is currently in progress using the DSA. Results of these studies will be presented in future reports.

Chapter 7

CONDUCTIVITY ENHANCEMENT

7.1 Introduction

An area of prime interest is improvement of MHD thruster performances by enhancing the conductivity of seawater by techniques such as super-sonic wave electrodes and seeding [43]. Of these techniques, the most promising is seeding. Seeding is accomplished by adding a concentrated strong acid or base solution, such as HCl, H_2SO_4 or $NaOH$, to the seawater. Since molar conductance is additive based on the concentration and strength of individual charge carrying ions in solution, the addition of a strong electrolyte will increase the conductivity of seawater significantly.

Conductivity enhancement of synthetic seawater by HCl, H_2SO_4 and $NaOH$ has been conducted in beaker experiments. Results of these experiments are presented in Figure 7.1 [48]. As can be seen, the experimentally determined enhancement of conductivity parallels the analytical results [49] fairly well. Of the three, the best enhancement was obtained by the 95-98 % H_2SO_4 solute. It should be noted that hydrochloric acid can only exist under atmospheric pressure at concentrations of approximately 37 %. However, if stored under higher pressure, a correspondingly higher concentration can be obtained.

When thus stored, the hydrochloric acid is anticipated to be the optimum medium for seeding. The reasons are two fold. First, since the HCl performs fairly well at 37 %, it is expected to enhance conductivity better than even the H_2SO_4 solution at higher concentration. An increase in concentration typically corresponds to an increase in conductivity. Second, by being stored under pressure, the HCl

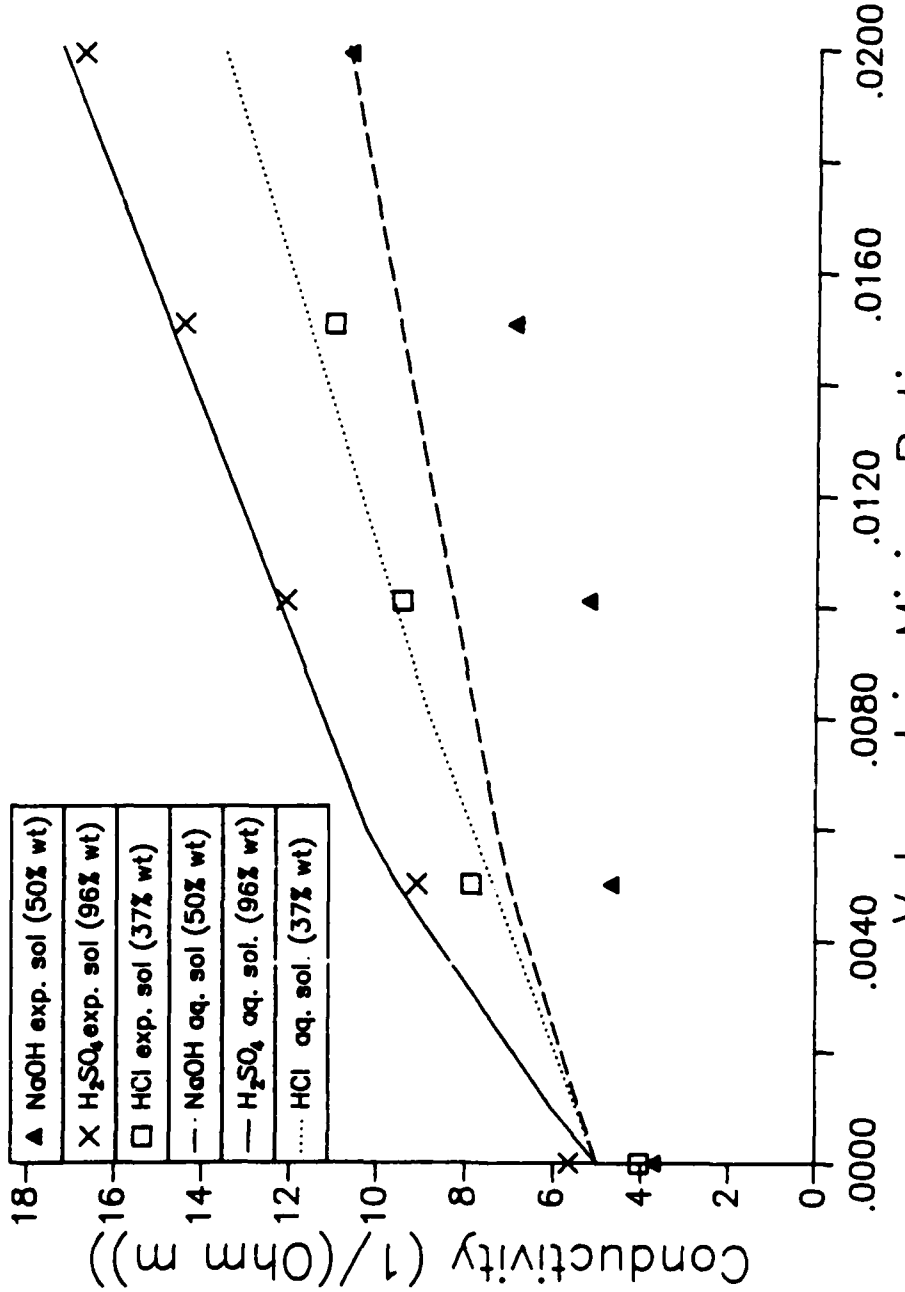

Figure 7.1 Theoretical versus Experimental Seeding.

solution will alleviate the need for an injection pump when incorporated in the MHD thruster design.

Since the MHD thruster must operate under flowing conditions, a synthetic seawater circulation loop is used to experimentally determine performance of H_2SO_4 seeding. Two cases are addressed. The first is conductivity enhancement of the synthetic seawater medium by uniform mixing of sulfuric acid at varying concentrations. This is accomplished by adding sufficient sulfuric acid to bring the synthetic seawater solution to the desired concentration, and conducting the electrolysis at steady state. The mixture is agitated to insure sufficient mixing. The second case is pulse injection of sulfuric acid just upstream of the test section. This case more accurately simulates the performance attainable in an MHD thruster since the strong electrolyte must be injected into the main seawater flow in the MHD channel.

Also of interest in seeding enhancement is the effect of the enriched solution on the performance of the electrode materials. Since only one set of electrodes were evaluated during the seeding experiment, the pair was chosen to consist of a both stable and an unstable electrode. One would expect that by enriching the solution, the destruction of the unstable electrode would be dramatically increased whereas the stable electrode should not be affected assuming no preferred reaction with the seeding ions exists. Graphite was chosen as the stable cathode, and Hastelloy-C anode was chosen as anode to observe its degradation.

7.2 Enhancement by Uniform Mixing

For conductivity enhancement by uniform mixing, voltage-versus-current plots are used to evaluate the performance of the H_2SO_4 at .5% and 1% enrichments by volume in seawater. These results are illustrated in Figures 7.2 and 7.3 respectively.

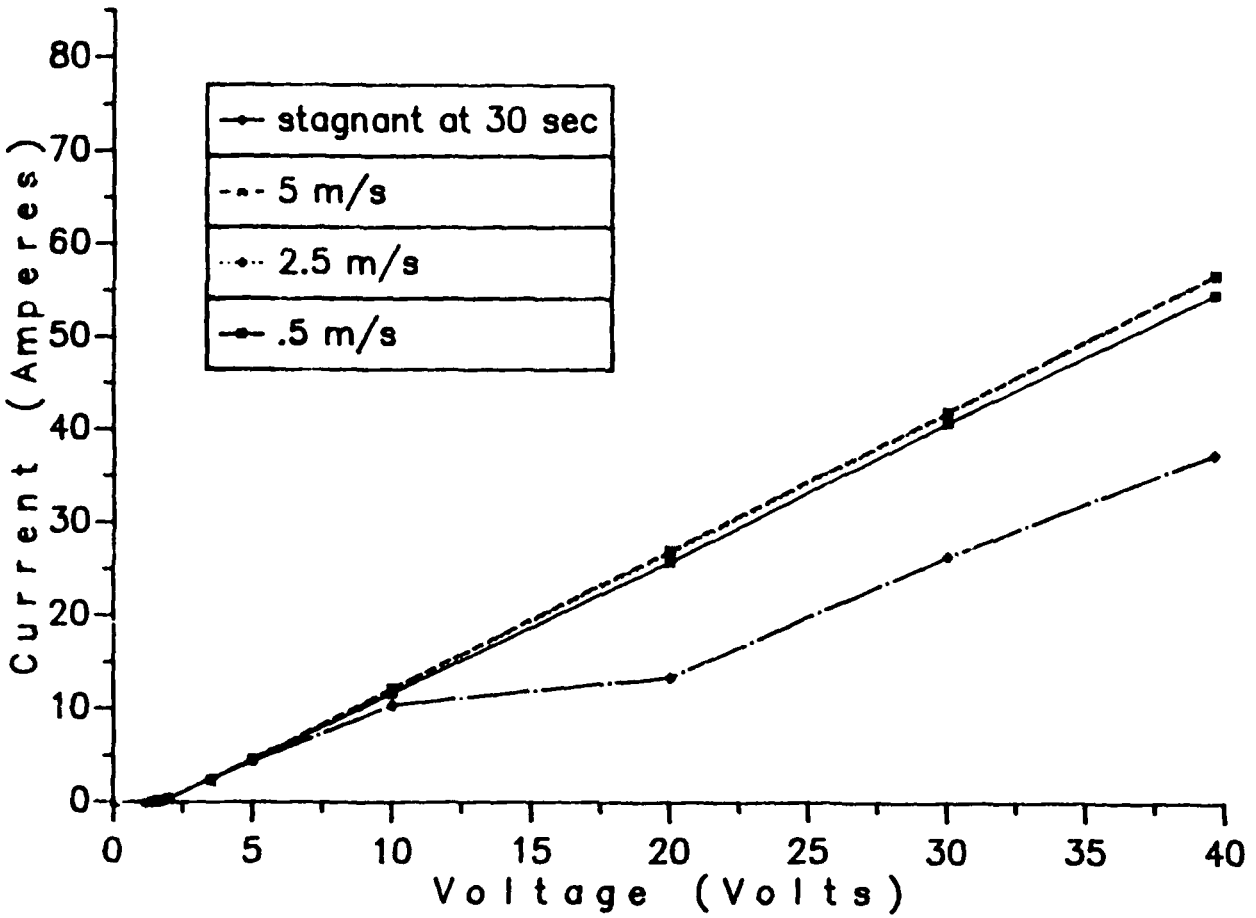

Figure 7.2 Current versus Voltage Enhanced by .5% H_2SO_4 by Volume for 2"×1" Duct with Hastelloy-C Anode and Graphite Cathode Anode on Top

Temperature = 25.1-27.9 °C. pH = 1.2-1.08.

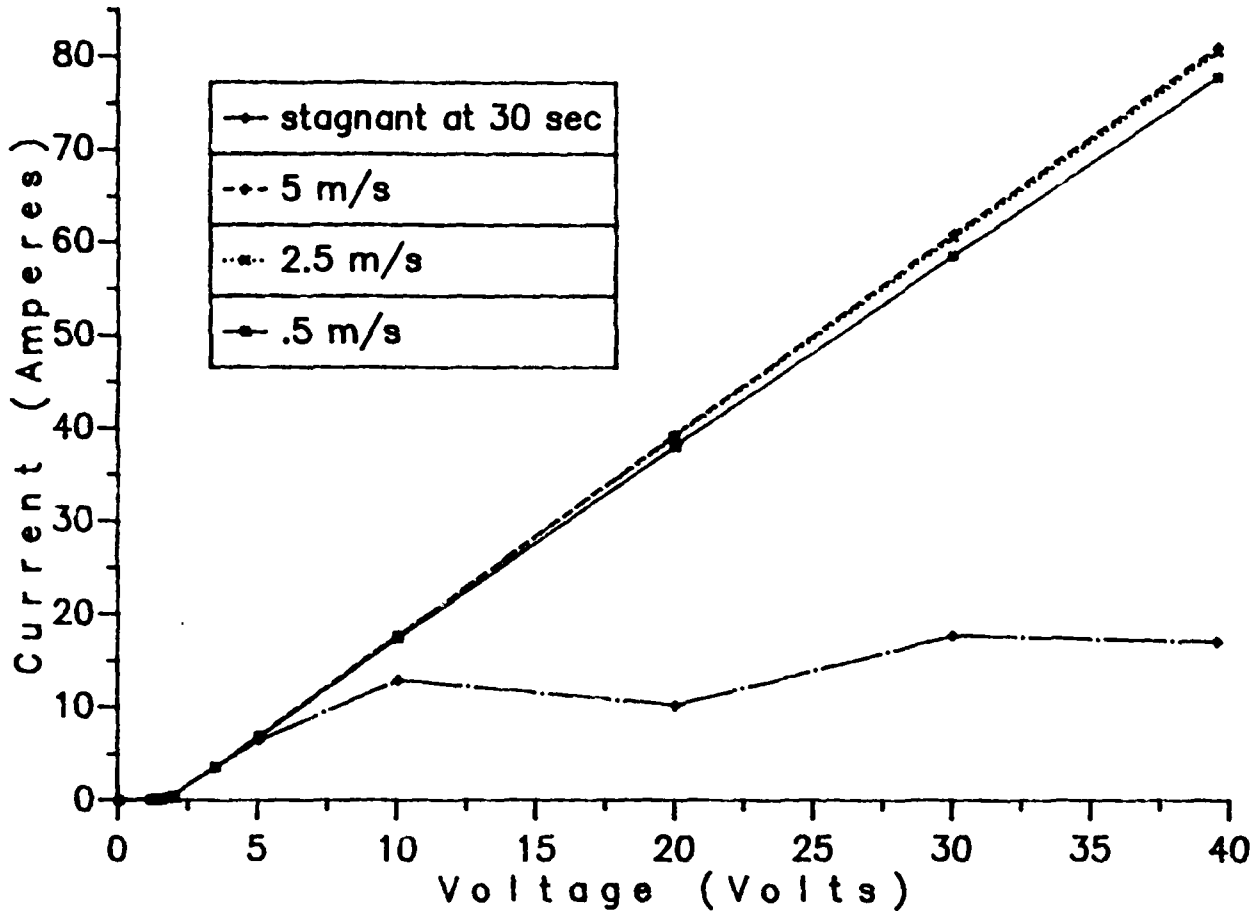

Figure 7.3 Current versus Voltage Enhanced by 1% H_2SO_4 by Volume for 2"×1" Duct with Hastelloy-C Anode and Graphite Cathode Anode on Top

Temperature = 29.5-32.4 °C. pH = .74-.69.

For both enrichments the general trends mirror those seen in the seawater studies discussed in chapter 6 (see Figs. 6.13 and 6.16). The 2.5 and 5 m/s cases performed better than the 1 m/s case and all flowing conditions performed better than the stagnant case. The coinsiding curves for 2.5 m/s and 5 m/s cases suggest that there exists a flow rate (somewhere between 1 m/s and 2.5 m/s) above which the voltage-versus-current performances are essentially the same for all flows.

The dramatic fluctuations in conductance of the stagnant cases are due to formation and movement of microbubbles coating the anode (top electrode). These H_2, O_2, and Cl_2 gases are nonconductive and therefore act as an insulating barrier. As bubbles disperse upstream and downstream from the electrode surface, a noticeable increase in conductance is observed.

As predicted by beaker experiments, the conductivity enhancement due to the sulfuric acid is fairly linear. By the addition of .5% H_2SO_4, the conductance increased by 98.8%. The addition of 1.0% H_2SO_4 resulted in a 187.6% increase in conductance. As would be expected, the pH of the solution changed dramatically with the addition of acid.

7.3 Enhancement by Pulse Injection

For the pulse injection studies, the effective conductivity of the seawater-H_2SO_4 mixture is the basis of evaluation. Utilizing test section geometry and experimentally determined values for voltage and current, the conductivity of seawater with seeding by H_2SO_4 under flowing conditions is determined. Figures 7.4, 7.5 and 7.6 present the results for pulse injections at 1, 2.5 and 5 m/s respectively with Hastelloy anode on top and graphite cathode on bottom.

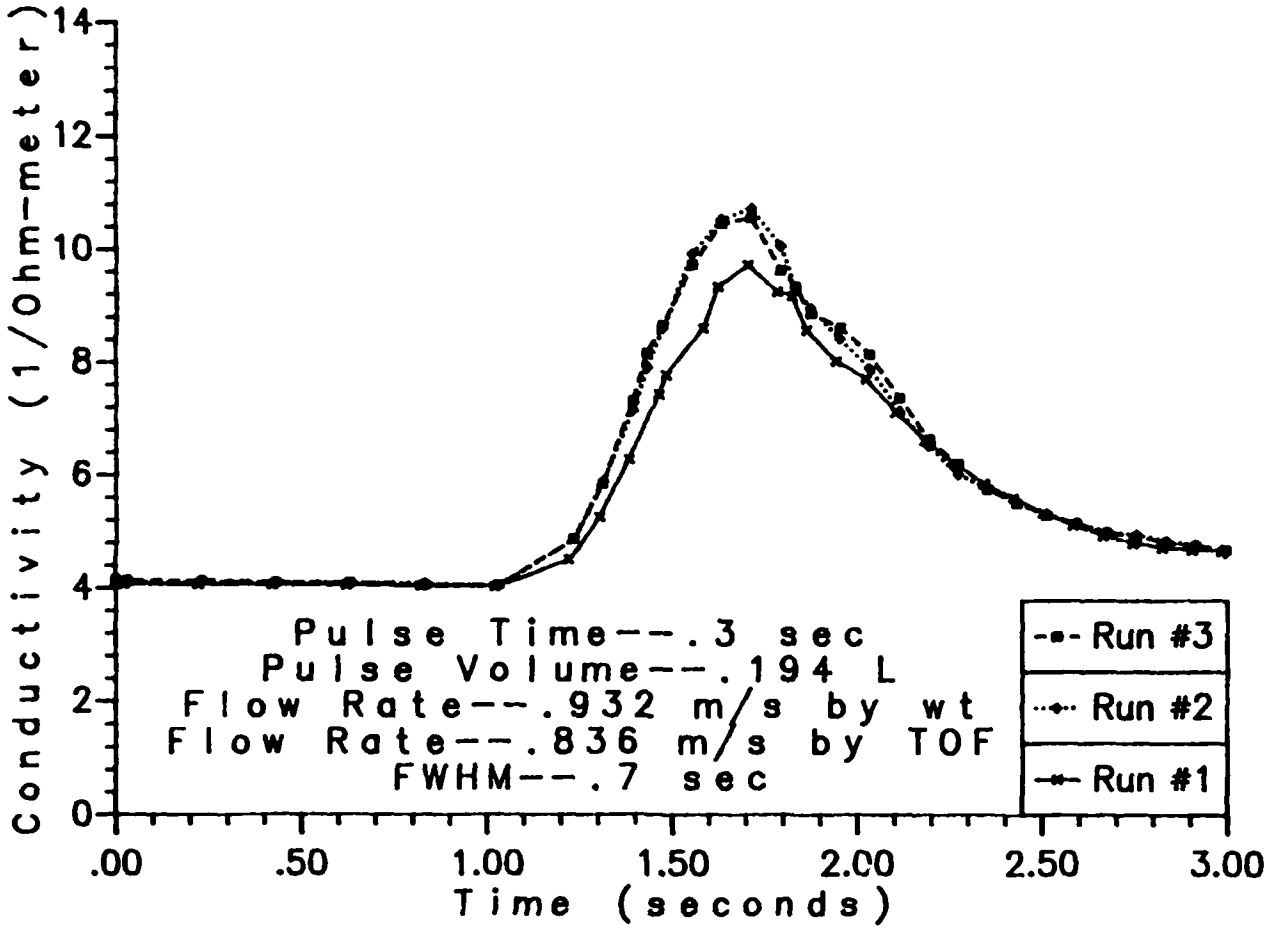

Figure 7.4 Conductivity versus Time for 1 m/s Flowing Condition with Pulse Injection of 10.33% H_2SO_4 by Volume Using Hastelloy-C Anode and Graphite Cathode Anode on Top

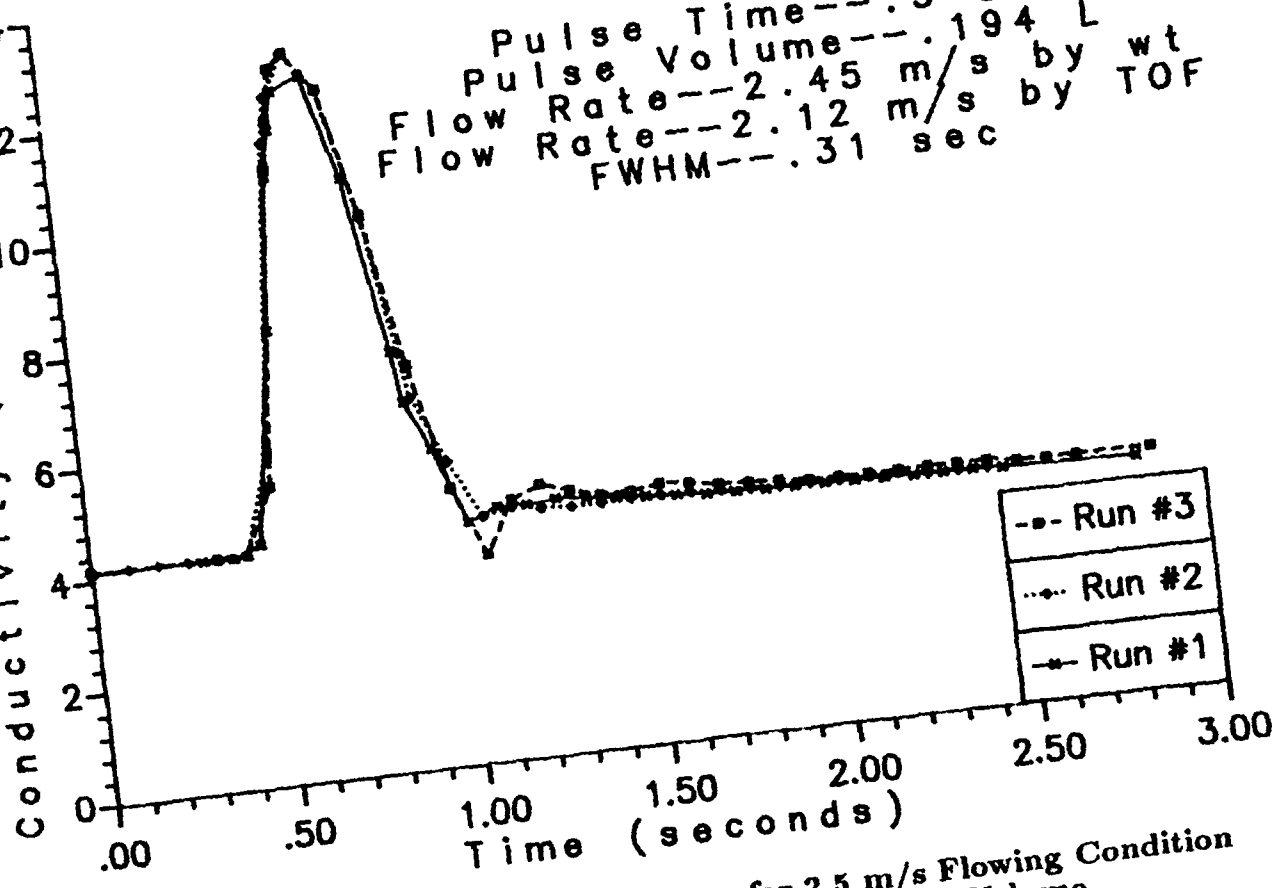

Figure 7.5 Conductivity versus Time for 2.5 m/s Flowing Condition with Pulse Injection of 10.33% H_2SO_4 by Volume Using Hastelloy-C Anode and Graphite Cathode Anode on Top

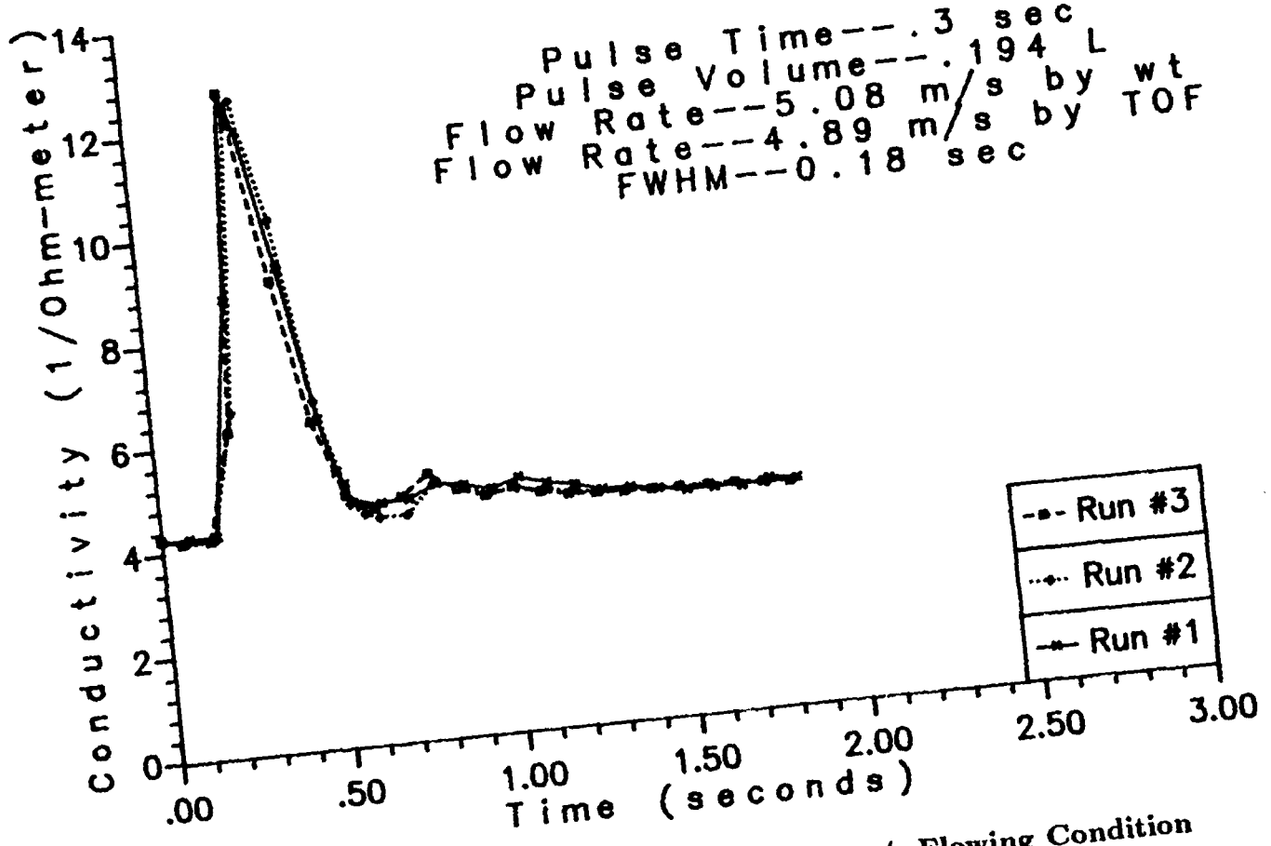

Figure 7.6 Conductivity versus Time for 5 m/s Flowing Condition with Pulse Injection of 10.33% H_2SO_4 by Volume Using Hastelloy-C Anode and Graphite Cathode Anode on Top

A second orientation with Hastelloy cathode and graphite anode on sides was investigated and results are illustrated in Figure 7.7. Figure 7.8 displays raw data from the 2.5 m/s case. A factor of 1.12 was used to correct for fringe field effects in determination of seawater conductivity. Time equal to zero has been set as time at which pressure pulse peak due to injection is detected across the electrodes. Time of flight (TOF) is the time required for the pulse of sulfuric acid enriched seawater to reach the electrodes upon being injected 1.428 m upstream. This has been determined by the difference between time zero and the time at which the conductivity as shown in Figs.7.4 through 7.7 has reached a maximum value.

For the 1, 2.5 and 5 m/s cases, the velocity of the slugs based on the time of flights were .836, 2.12, and 4.89 m/s. Based on weight of seawater accumulated in bypass tank following the run, the velocities for the same runs were deduced to be .932 ,2.45 and 5.08 m/s—a difference of 10.3, 13.5 and 3.7% respectively. One would expect the disruption of flow due to the pulse injection to decrease the channel velocity and this was observed.

By using the full width half maximum (FWHM) correlation on the transient of conductivity surge, the effective pulse widths have been determined. For the 1, 2.5 and 5 m/s runs, these are .7, .31 and .18 respectively. The difference in values with respect to variance in flowrates is fairly linear and is caused by time-dependent dispersion which is due to the turbulence of the flow—Re greater than 29,000 for all cases.

As presented in Fig. 7.7, the 1 m/s case oriented sideways with Hastelloy-C cathode and graphite anode obtained a larger increase in conductivity with sulfuric acid injection than the arrangement with Hastelloy-C anode at top (Fig. 7.4). This is attributed to slightly higher H_2SO_4 concentration and reduced effect of

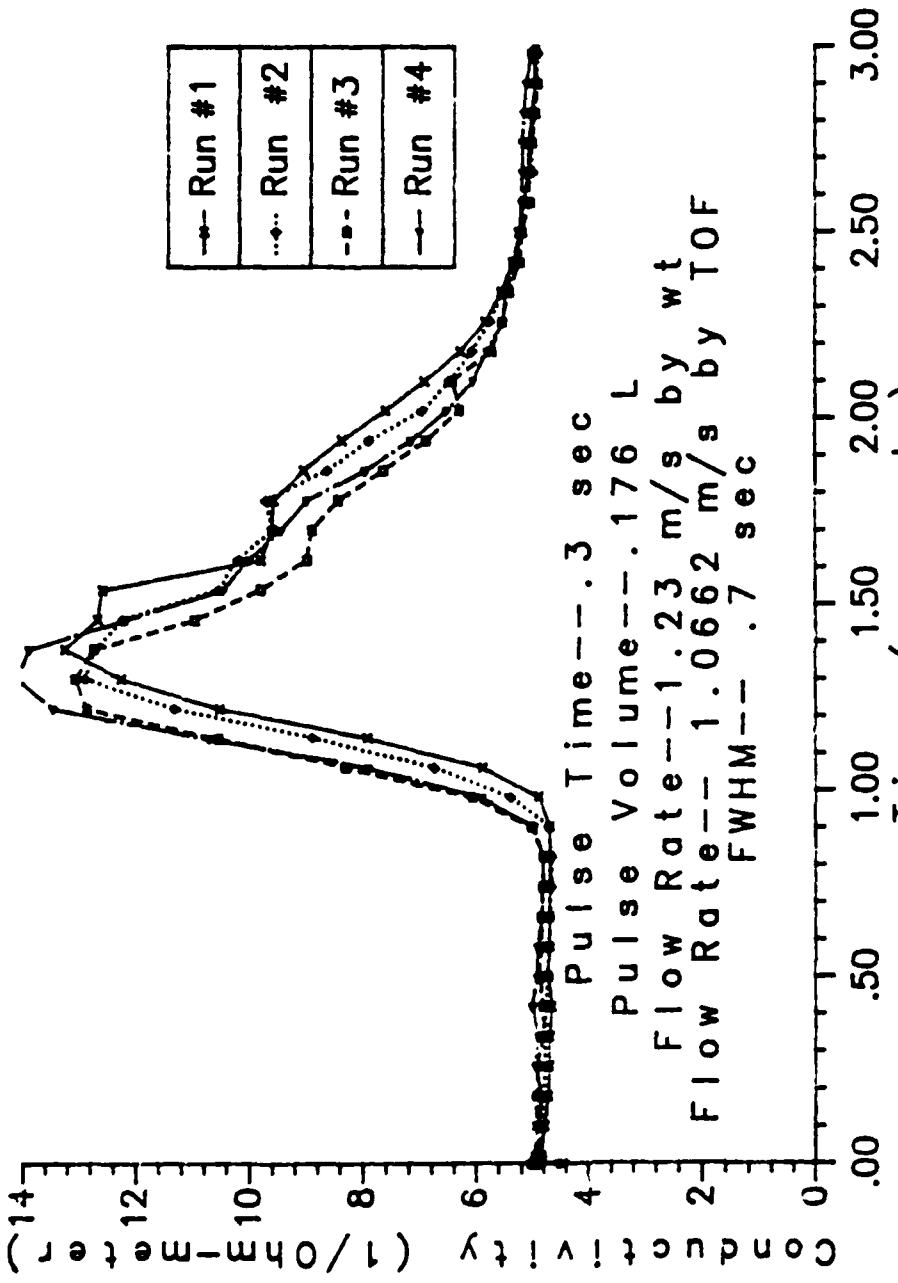

Figure 7.7 Conductivity versus Time for 1 m/s Flowing Condition with Pulse Injection of 11.11% H_2SO_4 by Volume Using Hastelloy-C Cathode and Graphite Anode Side by Side Orientation

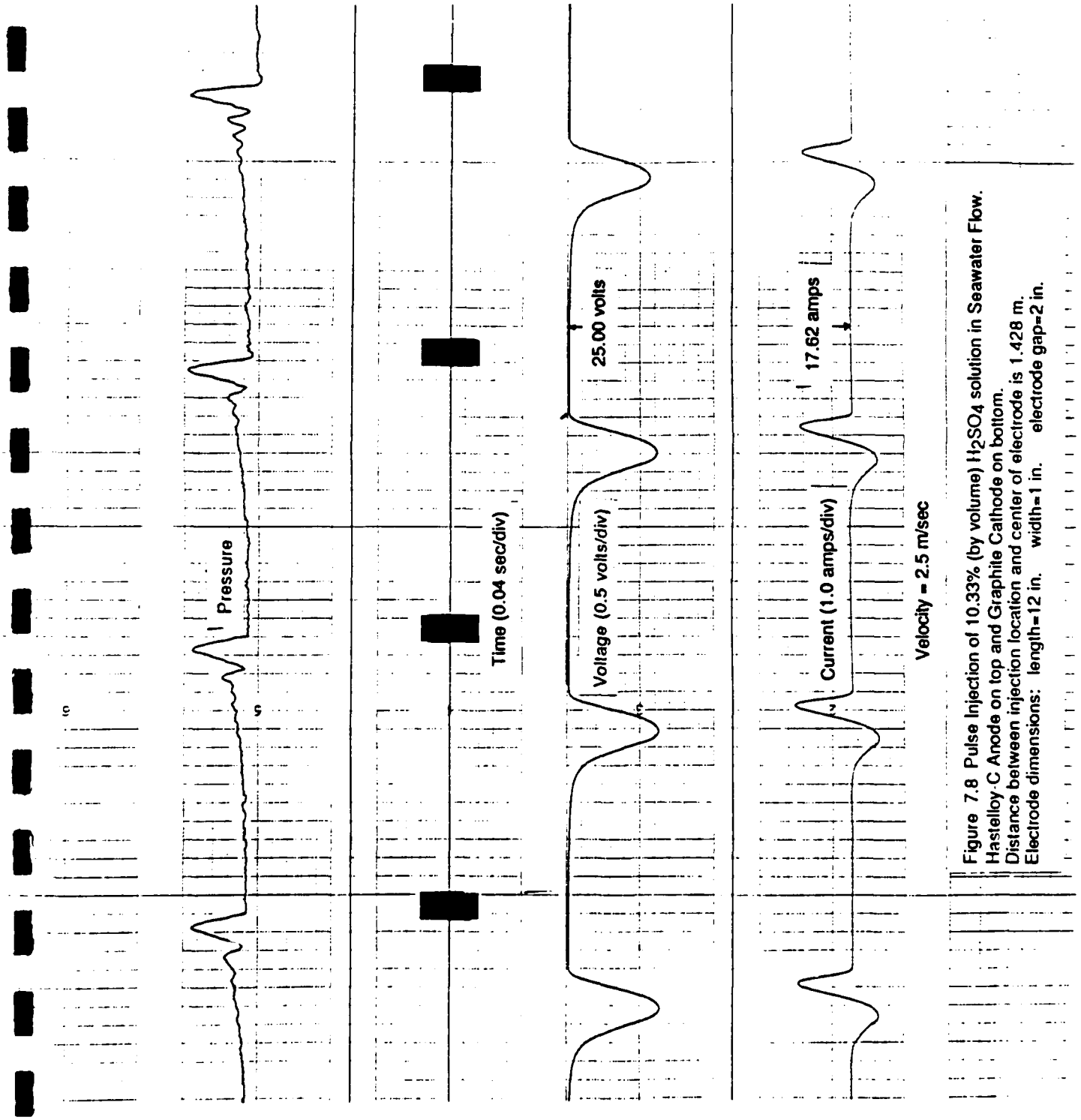

Figure 7.8 Pulse Injection of 10.33% (by volume) H_2SO_4 solution in Seawater Flow.
Hastelloy-C Anode on top and Graphite Cathode on bottom.
Distance between injection location and center of electrode is 1.428 m.
Electrode dimensions: length=12 in. width=1 in. electrode gap=2 in.

nonconductive gas products. At 1 m/s flow rate, the arrangement with anode at top will have lower conductance due to reduced flushing of product gases accumulating at top electrode. This contrasts sideways oriented electrodes where gases collecting at top of duct do not cover an electrode surface.

In 1 m/s cases as presented in Figs. 7.4 and 7.7, there are long trailing edges on the pulse profiles indicating the effect of wall boundary layer flow. This is not observed in higher flows as their profiles are symmetric.

Finally, the maximum conductance obtained by the 2.5 and 5 m/s cases are approximately the same. The peak for the 1 m/s case is significantly less but is offset by a much more substantial pulse width. This implies that at low flowrates (approximately 1 m/s) the thruster performance will be most efficiently augmented by seeding—minimal expenditure of H_2SO_4 because active time in channel is longer. However, at higher flowrates, an increase in conductance can be obtained at the expense of larger acid consumption. Since the conductivity peak at 5 m/s flowrate was approximately the same as that of the 2.5 m/s flow, the later velocity is a more optimal operating condition based on conductivity enhancement versus seed consumption.

7.4 Performance of Graphite and Hastelloy-C Electrodes

As expected, the stable graphite electrode was not noticeably affected by the sulfuric acid enhanced solution. In contrast, the Hastelloy-C electrode, which was slightly eroded as anode for seawater electrolysis, was severely attacked by the sulfuric acid enhanced solution. Figure 7.9 illustrates the severe distruction of the Hastelloy-C material. At beginning of experiment, the electrode thickness was 60 mils. After the runs, the thickness was 19 mils—a decrease of 68.3%.

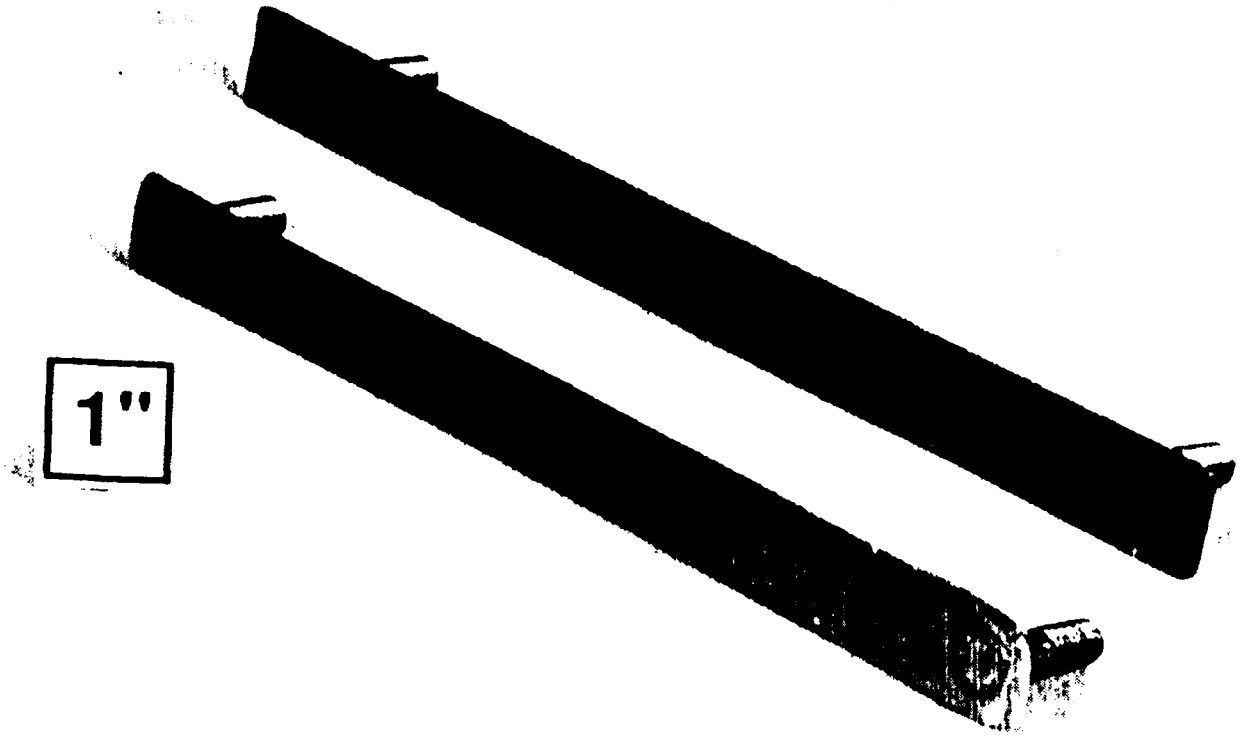

Figure 7.9 Degradation of Hastelloy-C Anode due to Sulfuric Acid Enriched Seawater Electrolysis; Top Electrode before Electrolysis; Bottom Electrode after Electrolysis

7.5 Conclusions

Based on this study, conductivity enhancement by seeding is a viable option to improve MHD thruster performance. Seeding is deemed necessary because it will allow the MHD thruster to operate in areas of lower conductivity, such as freshwater rivers and ports. It can also provide a means of sustaining higher vehicle speeds for short time durations. This attribute may be required for escape and evasion in military applications.

Because of the nature of strong acids and bases, a corrosive resistant material must be used for the electrodes. Based on this study, graphite is a good candidate. The DSA anode is also a possibility but further studies must be conducted to investigate its stability in the presence of a strong acid or base. Also, all vehicle surfaces exposed to the MHD thruster exhaust would need to be resistant to strong acid or base if conductivity enhancement is to be used.

Chapter 8

DISCUSSION

8.1 Feasibility of the MHD Thruster

The main query throughout this work is the feasibility of the MHD thruster in marine vehicle applications. As mentioned in chapter 1, interest in the MHD concept has been reenergized by advances in cryogenics and superconducting magnet technology. These advances have enabled achievement of much stronger magnetic fields than previously attained. For a feasible thruster design, magnetic fields on the order of 5+ T are required. Based on analytical results presented in chapters 2 and 3, the MHD concept for seawater applications now appears to be practical for large vehicles such as submarines, and small vehicles such as ROV and UAV. Minor upgrade of the existing nuclear power supplies should provide sufficient electric energy for large thruster vehicle applications. For smaller vehicles, the MHD thruster is practical when high speeds are not of paramount importance.

The ionic conductance of seawater, as discussed and experimentally investigated in chapters 4 and 6, is of sufficient magnitude to support the electric field required for operation of an MHD thruster. As anticipated, hydrogen gas formation was found to adversely affect the conductance process. Correspondingly, a dramatic increase in conductance was observed when the seawater was flowing past the electrodes versus the stagnant case. This is due to "flushing" of the hydrogen gas under flowing condition. A further increase in conductance with increasing flow rates can be attributed to increasing temperature of the electrolyte due to Ohmic heating and increased "flushing."

Of the electrode materials evaluated, graphite performed the best with no noticeable degradation. Experiments are currently in progress to evaluate the performance of DSA electrodes. DSA and gas diffusion materials will be a subject of future investigation. In addition, several other aspects concerning the MHD concept need to be more fully analyzed. Some of these are discussed in the following sections.

8.2 The A.C. Internal Duct Thruster

One very promising MHD thruster concept is the a.c. internal duct propulsion mechanism. In this arrangement, the electric field and the magnetic field alternate direction in phase so that the Lorentz force is always directed towards the rear of the vehicle. The benefits of this approach are substantial. If the frequency is in the order of 1 to 4 kHz, the polarization effects of the solution can be avoided [30].

However, if the frequency can be increased to over 5kHz, the molar conductivity of an electrolytic solution, Λ, will increase towards Λ_o (molar conductivity of the solution at infinite dilution) due to the disappearance of the time-of-relaxation effect [31]. A mathematically rigorous explanation of the time-of-relaxation effect is presented by Pierre M. V. Resibois [35]. The alternating current should also prevent buildup of reactant products on the electrode surfaces.

There are several potential problems with this design. One is synchronization of the alternating electric and magnetic fields. Secondly, choice of electrode materials may be limited due to oxidation and reduction reactions occurring on both electrode surfaces. Accumulation and recombination of H_2 and O_2 to attain additional thrust is probably not feasible. Likewise, use of oxygen preferred electrode may not be possible because of additional requirement for material to withstand

reduction reaction.

8.3 Performance of MHD Thruster at Different Pressures and Temperatures

The performance of the MHD thruster at various depth and oceanic temperature regions is of prime importance. Since the conductivity of seawater is both temperature and pressure dependent, these two influences must be considered in MHD feasibility studies. The dependence of conductivity on increasing pressure (increasing depth) is a linearly increasing function for the pressure ranges of interest (assuming constant temperature and salinity) [34].

If one assumes that the maximum diving depth for next generation submarines will be over twice that of present vessels, pressure and temperature gradients corresponding to 2000 m in depth must be taken into account. Since the pressure gradient of seawater is approximately 1 bar ($10^5\ N \cdot m^{-2}$) for every 10 m in depth [50], the maximum pressure for depths of interest is probably on the order of 200 bars. An increase of pressure of 200 bars correlates to an increase in conductivity of 1.35 % to 3.19 % for temperature ranges of -1.85°C to 30°C, respectively [51]. This slight improvement in conductivity will not significantly enhance the MHD thruster performance. However, the change incurred in conductivity due to variations in temperature is significant.

The temperature of the oceans' surfaces ranges from as high as 30°C in the tropics to as low as -2°C under arctic ice [50]. This corresponds to conductivity values ranging from 5.84 to 2.67 $\Omega^{-1}m^{-1}$; a 54.3 % variation in conductivity. The mean surface temperature is on the order of 20°C. Up to a depth of 100 meters or more, the seawater is well mixed and has a fairly consistent temperature. However, below this region is the zone of rapid temperature decrease with increasing depth

known as the thermocline. At a depth proportional to 200 bars, the mean oceanic temperature has dropped to $3.8°C$ [50]. From Table 4.1, the conductivity of seawater at $20°C$ is 4.71 $\Omega^{-1} \cdot m^{-1}$. At $3.8°C$, the conductivity is 3.19 $\Omega^{-1} \cdot m^{-1}$. This represents a corresponding decrease in conductivity of 32.3 %. Since the MHD thruster is linearly dependent on conductivity, its performance will be severely reduced in regions of cold water.

8.4 Cooling of the Superconducting Magnet's Filaments

One major drawback with current commercial superconducting magnet designs is the requirement to maintain the $NbTi$, Nb_3Sn, or $(Nb,Ta)_3Sn$ filaments at temperatures in the order of $4.2°K$ [24]. This requires cooling by liquid helium which is very expensive.

Research in the area of superconductive ceramics has lead to the development of certain oxides that become superconducting above $90°K$. This is significant because coolant boiloff would be reduced and temperatures above $77°K$ can be reached by cooling with liquid nitrogen which is much less expensive. Unfortunately, the ceramic materials are characteristically brittle and fragile [52], which make them impractical in current MHD thruster designs. Further research in superconductive ceramics may solve this problem.

In present superconducting magnet design, the He boiloff can be reduced by inclosing the magnetic windings in a cylinder cooled with He. This cylinder is then enclosed by an outer cylinder cooled by liquid nitrogen. This technique keeps the He cylinder's outer walls at approximately $80°K$ and thereby reduces helium coolant losses [53]. Obviously, the boiloff of helium and nitrogen during the cooling process must be taken into account in future MHD thruster designs, since sizeable quantities

of liqiud helium and nitrogen will be required to sustain the MHD thruster during operation.

8.5 Gas Production

Hydrogen and oxygen gas formation may present a severe problem for military applications of the MHD thruster. Due to the fairly insoluble nature of H_2 and O_2, a visible trail of these gas products may exist in the wake of a magnetohydrodynamically propelled submersible. Such distinguishable optical and acoustic signatures would make the MHD thruster impractical for submarine use unless some method of filtering the gasses from the exhaust seawater can be devised. The most promising solution would be the use of gas diffusion electrodes since this would also allow recombustion of hydrogen and oxygen.

More investigation in the area of Cl_2 production is also necessitated by environmental concerns. If chlorine gas is produced on the anode to any significant degree, it may negatively impact the ocean's ecosystem. A logical solution is the use of the oxygen preferred anode. However, studies are needed to insure that the electrode's oxygen production performance will not deteriorate over time.

8.6 Closing

Based on this investigation, the MHD thruster concept is a very promising form of next generation marine vehicle propulsion. It potentially offers reduced maintenance, less noise, and higher vehicle speeds then screw-type propulsion. To validate the concept, a prototype thruster needs to be constructed. Concurrently, further research in electrode metallurgy, product gas formation, and superconducting ceramics needs to be conducted to improve the potential success of the MHD thruster.

REFERENCES

1. W. A. Rice, U. S. patent 2997013, August 12, 1961.
2. J. B. Friauf, "Electromagnetic Ship Propulsion," *J. of Amer. Soc. of Naval Engrs.*, Feb., 1961, pp. 139-142.
3. O. M. Phillips, "The Prospects for Magnetohydrodynamic Ship Propulsion," *J. of Ship Res.*, March, 1962, pp. 43-51.
4. R. A. Doragh, "Magnetohydrodynamic Ship Propulsion using Superconducting Magnets," Soc. of Nav. Architects and Mar. Eng., Annual Meeting, New York, Nov. 14, 15, 1963.
5. S. Way, "Propulsion of Submarines by Lorentz Forces in the Surrounding Sea," Amer. Soc. of Mechanical Engrs, Paper 64 WA/ENER7, Nov., 1964.
6. S. Way and C. Devlin, "Prospects for the Electromagnetic Submarine," Collection of Technical Papers, AIAA 3rd Propulsion Joint Specialist Conference, Washington D. C., July 17-21, 1967, Paper # 67-432.
7. A. Iwata, Y. Saji and S. Sato, "Construction of Model Ship ST-500 with Superconducting Electromagnetic Thrust System," Proc. ICEC 8, 1980, pp. 775-784.
8. E. Tada, Y. Saji, K. Kuroshi and T. Fujinaga, "Fundamental Design of a Superconducting EMT Icebreaker," *Trans. IMarE(C)*, vol. 97, Conf. 3, Paper 6, 1984, pp. 49-57.
9. A. Iwata and Y. Saji, "Superconducting Electro-Magnetic Ship Propulsion," unpublished paper, 1988.
10. Y. Sasakawa, K. Imaichi, E. Tada and S. Takezawa, "Japanese Experimental Ship with the Superconducting Electromagnetic Thruster," Paper presented in the Applied Superconducting Conference in Osaka University, Japan, Oct. 17, 1988.
11. Pasha Publications, Arlington, VA, "MHD Sub Propulsion System to be Tested at Argonne," *Navy News and Undersea Technology*, vol. 6, no. 46, Nov. 27, 1989, pp. 1-2.
12. Pasha Publications, Arlington, VA, "Evidence Grows the 'Pod' is a Superconductive Drive," *Navy News and Undersea Technology*, vol. 7, no. 11, March 19, 1990, pp. 1-2.
13. T. Stefanick, "The Nonacoustic Detection of Submarines," *Sci. Amer.*, vol. 258, no. 3, March, 1988, pp. 41-47.
14. J. E. Moore and R. C. Hall, **Submarine Warfare: Today and Tomorrow**, Adler and Adler Publishing Inc., 1986, pp. 28-73.
15. J. E. Moore, **Warships of the Soviet Navy**, Janes Publishing Inc., 1981, pp. 15-39.
16. N. Polmar and B. Allen, **Rickover**, Simon and Schuster, 1982, pp. 353-687.

17. Navy League of the United States, **The Almanac of Seapower**, 1983, pp. 142-149.

18. J. M. Moore, **Janes Naval Review**, Janes Publishing Inc., 1987, pp. 80-92.

19. W. F. Hughes and F. J. Young, **The Electromagnetohydrodynamics of Fluids**, John Wiley and Sons, Inc., 1966, pp. 144-148.

20. A. P. Baranov, "Future of Magnetohydrodynamic Ship Propulsion," *Sudostroyeniye*, no. 12, Dec. 1966, pp. 3-6.

21. G. T. Hummert, "An Evaluation of Direct Current Electromagnetic Propulsion in Sea Water," Office of Naval Research Project Report, no. 79-9B2-EMSUB-R1, 1979.

22. R.D. Blevins, **Applied Fluid Dynamics Handbook**, Van Nostrand Reinhold Company Inc., 1984, pp. 44-54.

23. G. L. Tuve and L. C. Domholdt, **Engineering Experimentation**, McGraw Hill, 1966, pp. 369-381.

24. T. F. Lin, J. B. Gilbert and R. Kossowsky, "Sea Water Magnetohydrodynamic Propulsion for Next-Generation Undersea Vehicles," ONR annual report, NTIS: ADA218318, Feb., 1990, pp 5, 32-36.

25. G. P. Sutton, **Rocket Propulsion Elements**, John Wiley and Sons, Inc., 1956, pp. 13-23.

26. T. C. Gillmer and B. Johnson, **Introduction to Naval Architecture**, United States Naval Institute, 1982, page 220.

27. SV. AA. Harvald, **Resistance and Propulsion of Ships**, John Wiley and Sons, Inc., 1983, pp. 98-100.

28. T. C. Gillmer, **Modern Ship Design**, United States Naval Institute, 1975, page 134.

29. A. A. Bednarczyk, **Nuclear Electric Magnetohydrodynamic Propulsion for Submarine**, M.I.T. Thesis, 1989, pp. 101-103.

30. W. J. Moore, **Physical Chemistry**, Fourth Edition, Prentice-Hall, Inc., 1972, pp. 420-565.

31. J. Koryta and J. Dvořák, **Principles of Electrochemistry**, John Wiley and Sons, Ltd., 1987, pp. 105-385.

32. J. E. Bennett, "Electrodes for Generation of Hydrogen and Oxygen from Seawater," *Int. J. of Hydrogen Energy*, vol. 5, Pergamon Press Ltd., 1980, pp. 401-408.

33. J. O'M. Bockris and S. U. M. Khan, **Quantum Electrochemistry**, Plenum Press, 1979, pp. 1-5.

34. S. I. Smedley, **The Interpretation of Ionic Conductivity in Liquids**, Plenum Press, 1980, pp. 152-156.

35. P. M. V. Résibois, **Electrolyte Theory: An Elementary Introduction to a Microscopic Approach**, Harper and Row, Publishers, Inc., 1968. pp. 88-107.

36. T. Erdey-Grúz, **Kinetics of Electrode Processes**, John Wiley and Sons, Inc., 1972, pp. 28-31.

37. D. W. Cott, V. W. Daniel, R. A. Carrington and J. S. Herring, "MHD Propulsion for Submarines," Component Development Integration Facility External Report, No. 2DOE-MHD-D140, Oct. 10, 1988, pp. 56-64.

38. S. Motoo and N. Furuya, "Gas Diffusion Electrode for Hydrogen Evolution," *J. of Elec. Chem.*, vol. 161, 1984, pp. 189-191.

39. M. Hiroi, M. Muroya, E. Tada and S. Ogawa, "Anodes for Superconducting Electromagnetic Propulsion Ships," *Denki Kagaku*, vol. 57, no. 8, Aug. 1989, pp. 837-840.

40. Robert C. Weast, **CRC Handbook of Chemistry and Physics**, 58^{th} Edition, CRC Press, Inc., 1978, pp. D141-146, D249, F3, F203.

41. T. M. Dauphinee, J. Anesin, H. P. Klein and M. J. Phillips, "The Effect of Concentration and Temperature on the Conductivity Ratio of Potassium Chloride Solution to Standard Seawater 35% (Cl 19.3740%)," *IEEE J. of Ocean. Eng.*, vol. OE-5, no. 1, Jan. 1980, pp. 17-21.

42. F. Culkin and N. D. Smith, "Determination of the Concentration of Potassium Chloride Solution Having the Same Electrical Conductivity, at 15°C and Infinite Frequency as the Standard Seawater of Salinity 35.0000% (Chlorinity 19.37394%)," *IEEE J. of Ocean. Eng.*, vol. OE-5, no. 1, Jan. 1980, pp. 22-23.

43. T. M. Dauphinee and H. P. Klein, "Proposal to Calibrate Standard Seawater Conductivity Relative to a KCL Solution, Preliminary Results," UNESCO Technical Papers of Marine Science, vol. 28, annex 3, 1978, page 35.

44. A. Poisson, "Conductivity/Salinity/Temperature Relationship of Diluted and Concentrated Standard Seawater," *IEEE J. of Ocean. Eng.*, vol. OE-5, no. 1, Jan. 1980, pp. 41-49.

45. B. D. Thomas, T. G. Thompson, and T. G. Thompson and C. L. Utterback, " The Electrical Conductivity of Seawater," *J. of Cons. Int. Explor. Mer.*, vol. 9, 1934, pp. 28-35.

46. W. S. Reeburgh, "Measurements of Electrical Conductivity of Seawater," *J. of Marine Res.*, vol. 23, 1965, pp. 187-199.

47. Personal correspondence with Akira Iwata, Senior of Cryogenic Research Laboratory, Technical Institute, Kawasaki Heavy Industries, Ltd., Nov. 29, 1988.

48. J. A. Naggar, T. M. Imblum, J. B. Gilbert, and T. F. Lin, "Observation of Flow Electrolysis with Simulated Sea Salt Solutions," to be presented at ONR's review meeting, Newport, Rhode Island, Oct. 15-17, 1990.

49. T. F. Lin, "Considerations of Sea Water Conductivity Enhancement for Electromagnetic Thrusters," paper presented in the 25th Intersociety Energy Conversion Engineering Conference (IECEC), #900147, Reno, Nevada, Aug. 12-17, 1990.

50. M. Whitfield and D. Jagner, **"Marine Electrochemistry: A Practical Introduction"**, John Wiley and Sons, Ltd., Belfast, Nothern Ireland, 1981, pp. 13-17.

51. A. L. Bradshaw and Karl E. Schleicher, "Electrical Conductivity of Seawater," *IEEE J. of Ocean. Eng.*, vol. OE-5, no. 1, Jan. 1980, pp. 50-61.

52. E. T. Smith and J. E. Davis, " 'Our Life Has Changed': The Lightbulb, The Transistor - Now The Superconductor," ***Bus. W.***, April 6, 1987, pp 94-97.

53. Discussion with Kwang-Fu Hwang, 25 June 1990.